Exploring the Biological Activity of Rhodium Metalloinsertors

Thesis by

Kelsey Melinda Boyle

In Partial Fulfillment of the Requirements for the degree of

Doctor of Philosophy in Chemistry

CALIFORNIA INSTITUTE OF TECHNOLOGY

Pasadena, California

2019

Defended December 19, 2018

Kelsey Melinda Boyle
ORCID: 0000-0002-6728-8403

ACKNOWLEDGEMENTS

First and foremost, I must thank my advisor, Professor Jacqueline Barton. Over these last five years, you have been a mentor and a role model. You have always given me autonomy in my projects and guidance, support, and encouragement when needed, and I am no doubt the scientist I am today because of your mentorship. I feel very fortunate to have worked with such a powerful woman in science, and I hope to exude the same strength and enthusiasm to my own future students. My thesis and graduate experience wouldn't have been the same with any other advisor, and for that I thank you.

I must also thank my thesis committee, as they have provided unparalleled academic and personal guidance throughout my journey at Caltech. To Harry Gray, thank you for being a pillar of support and for providing much needed words of encouragement at the times I most greatly felt the pressures of graduate school. To Dave Tirrell, thank you for your ever-present encouragement, support, and confidence in my ability to excel at my goals. To Doug Rees, thank you for your openness, guidance, and encouragement. I feel so fortunate to have had the dream-team of mentors on my committee, and I am deeply grateful for everything all of you have done.

There are the many members of the Caltech community and beyond that have helped me over the past few years. In particular, I would like to thank the people that have worked closely with me on my scientific and personal endeavors. To the Barton group's current administrative coordinator, Elizabeth Garcia, thank you for always being there to calm me down and build me up when I've needed it. You are a great friend, and I hope to continue to exchange cat videos and weird snacks with you for years to come. To Scott Virgil, purifying the diastereomers and enantiomers of my complexes would have been hell without your help. Thank you so much for your guidance and for always explaining how you think about scientific challenges—it has made me a better scientist. To Nathan Dalleska, thank you for helping me run my samples, guiding me on how to improve my methods, and making me feel better whenever I think accidentally ruined the ICP-MS. To Jens

Kaiser, you have taught me pretty much everything I know about the world of crystallography. Thank you for being helpful and patient through the many frustrations of my crystallographic endeavors. And to Julie Bailis at Amgen, thank you for providing a biological perspective on my research that challenges me to understand more and work harder.

To the many other essential CCE community members—Mo Renta, Elisha Okawa, Joe Drew, Agnes Tong, Amy Woodall-Ojeda, Silva Virgil, Haick Issaian, Lauriane Quenee, Alison Ross, Anne Penney, Steve Gould, Elisa Brink, Mona Shahgholi, Dave VanderVelde, Nate Siladke, the stockroom staff, and the custodial staff—thank you for keeping this huge CCE machine running day-to-day and for making sure that the chemistry is the hardest part of research.

I am also extremely grateful to the many members of the Barton group, both past and present, for making our lab an easy and fun place to work. First I must thank my colleagues and friends on the south side of lab. Alexis Komor and Alyson Weidmann, thank you for serving as my mentors when I was just beginning my journey. Adam Boynton, you were a fantastic labmate and such a positive, optimistic force in the lab—thank you for all the help and discussions over the years. Natalie Muren, your encouraging and inviting attitude is truly wonderful, thank you for always providing open and honest advice and perspective on life at and after Caltech. Lionel Marcélis, you are a great friend and mentor, and I thank you for always sticking around lab late at night to help me safely open bottles of triflic acid. Stephanie Threatt, I have some of my best science and life discussions with you, though they are often interrupted by my need to show you pictures of my cat—it's been a pleasure becoming friends these past few years. To the many current and recent postdocs in our lab, Yingxin Deng, Levi Ekanger, Adela Nano, Edmund Tse, Katie Schaefer, and Sandra König, you have all been so supportive and willing to give great advice on maneuvering grad school and achieving my career goals. You are all great mentors. To the rest of the group—Ariel Furst, Anna Arnold, Michael Grodick, Ted Zwang, Liz O'Brien, Phil Bartels, Siobhán MacArdle, Viktoria Urland, Aoshu Zhong, and Nirit Kantor—thank you for all the fun

conversations and the enlightening science discussions. And to my undergraduate mentees, Paige Gannon and Catherine Day, working with you was a true highlight of my graduate career. Your eagerness to learn, your excitement for science, and your overall wonderfulness made the summers at Caltech my favorite time of the year. I know you will keep being amazing in your own graduate programs, and I cannot wait to see what great things you both do.

I think it is no secret to anyone that I am greatly passionate about chemistry education, and there are many at Caltech and beyond whom I must thank for helping me develop this passion into a career. First I must thank my colleagues at Caltech's Center for Teaching, Learning, and Outreach (CTLO). To Cassandra Horii, thank you for all of your support throughout my time at Caltech and for allowing my to explore the world of education as a CPET co-director. To Jenn Weaver, between the coffee breaks and me inheriting your old clothes, you are like a big sister away from home. Thank you so much for always being there to listen to my problems and help me see things from a different perspective. To the rest of the CTLO—Leslie Rico, Mitch Aiken, Kitty Cahalan, Ellie Race-Moore, Julius Su, James Maloney, Tina Zelaya, Holly Ferguson, Daniel Thomas, and Olivia Wilkins—thank you for your help, guidance, and support. Thank you also to Veronica Jaramillo for helping me learn about the community college system and letting me sit in on your class from time to time. It has been an invaluable experience and has made me confident in my decision to become an educator.

Next, I want to thank the many people who helped me with the development of Ch101. To the faculty mentors who helped Rebekah Silva and me start the program—Harry Gray, Dave Tirrell, Mitchio Okumura, and Brian Stoltz—thank you for everything. Teaching our own course was a dream come true that was only possible because you believed in us and supported us. To everyone else involved in getting Ch101 started—Agnes Tong, Amy Woodall-Ojeda, and Silva Virgil who helped us on the administrative end, the CCE faculty mentors who have rotated through the program, the passionate postdocs and graduate students who volunteered to spend their free time

teaching classes, and of course the amazing undergraduate students at Caltech who took a chance on new elective courses taught by novice instructors—thank you so much. Thank you especially to my co-instructors Rebekah Silva and Levi Ekanger for making Ch101 an amazing collaborative experience, to my faculty mentors Dave Tirrell and John Bercaw for their teaching advice, and to the students who took my classes and made Ch101 the highlight of my week. Thank you all for helping me to become a better teacher.

I feel fortunate to have also made many great friends during my time here at Caltech who help keep me sane when I'm not in lab. Emily Blythe, you were the first friend I made at Caltech, and I can't possibly imagine the last five years without the many crafternoons, game nights, and Veggie Grill outings. You are such a genuinely wonderful human being and a caring friend. Rebekah Silva, you were my first friend in the Barton group. While we've never collaborated in our research, I can't think of anyone else who I've worked with more—from CPET to creating Ch101 to teaching Ch101—we've been through a lot! You are such an incredible and kind friend who has always been there for me with a shoulder to cry on and a couch to sleep on when I don't want to drive home. Andy Zhou, since we became friends the amount of time I spent bursting with laughter has skyrocketed. We've had so many great conversations and walks to the C-store over the past few years, and you are one of the most open and genuine friends I have. Tonia Ahmed, we've had some great all-nighters, listening to Beyoncé, eating crappy pizza, and furiously trying to finish our Ch212 problem sets before the sun rises. That class was fun, but the best part of it was becoming friends with someone as flawless as you. To all the other friends who've kept grad school fun over the years—Joe Redford, Griffin Chure, Ferdi Huber, Catie Blunt, Bill Ireland, Sam Ho, Belinda Wenke, Carissa Eisler—thank you.

There have been so many people before Caltech who have supported me, invested their time in me, and believed in me, and they are all part of the reason I am here today. To my many scientific mentors throughout the years, in particular Reed Eisenhart, Mr. Bohacek, Nathan Schultz,

Connie Lu, and John Ellis, thank you for your guidance and for believing in me. To all of my incredible friends and specifically to Caitlin, Ceal, Rebecca, and Sam, thank you for your support and for forcing me to get out of my lab and do something fun when you visited on your California vacations. To my incredible family, there are so many grandparents, aunts, uncles, and cousins who have always been proud of me and supported my decisions, and I thank all of them.

To my aunts Carrie, Lori, and Mona who were always around when I was growing up—thank you for teaching me how to be a funny, sassy, independent woman. To Elliot, you are an incredible brother-in-law and add a great dynamic to our family. To my sister Shannon, I really couldn't ask for a more incredible seester. You constantly inspire me with how hard you fight for your dreams, how much you care for others, and how you are so genuinely and unapologetically yourself. I am so proud of you and will always look up to you. To my parents, I wouldn't be the person or scientist I am today without the two of you. You always joke that you don't know where Shannon and I got our academic drive, bur I assure you that you taught us all of the qualities that have made us good scientists. You taught us to work hard, to be honest, to be creative, to be patient, to be curious, to never give up, and so importantly that our worth isn't tied to our academic success. I don't think any amount of words could ever express how much I appreciate you both. You have given me all the help, love, and support I could ever need. I love you both and this thesis is dedicated to you. Thank you for everything.

And finally, to my family in California, Deano and Pangur Bán. To Deano—we've been together through the entire journey of graduate school—from first applying to Caltech and UCI, to moving cross-country from MN to CA, to adopting the most purrfect and quirky fur-baby/writing buddy/mouse-toy fetcher, to defending our theses, and now to moving back home to start our new careers. Thank you for always being by my side, I don't know if I could have done all of this without you. I love you so much and I cant wait to start the next phase of our lives together.

ABSTRACT

Rhodium metalloinsertors are a unique family of potential anticancer agents that have been show to bind selectively to thermodynamically destabilized DNA base pair mismatches, abasic sites, and insertions/deletions (indels) *in vitro*. These metalloinsertors are also able to target mismatches in cells: metalloinsertors preferentially kill mismatch repair (MMR)-deficient cancer cells, which have a relative abundance of uncorrected DNA mismatches and indels, over MMR-proficient cells, which can repair these lesions. As such, these complexes have shown great promise as a potential treatment strategy for MMR-deficient cancers, which are often resistant to classic chemotherapies.

Recently, a new class of metalloinsertors that bear a rhodium-oxygen bond was synthesized and shown to have remarkable potency and selectivity towards MMR-deficient cells. We have discovered many key differences between first generation metalloinsertors and these new Rh-O metalloinsertors: (1) the MMR-selectivity of first generation metalloinsertors is heavily influenced by ancillary ligand bulk and lipophilicity, whereas the MMR-selectivity of Rh-O metalloinsertors is strong *regardless* of ancillary ligand properties, (2) first generation metalloinsertors have toxicities in the micromolar range while Rh-O metalloinsertors have toxicities in the *nano*molar range, and (3) first generation metalloinsertors can only bind DNA via the Δ-enantiomer while Rh-O metalloinsertors can bind DNA via both the Δ- *and* Λ-enantiomers. Excitingly, the improved potency and selectivity of these "Rh-O" metalloinsertors brings them into a realm of clinical relevance.

Here we examine the basis for the improved potency and selectivity of these new Rh-O metalloinsertors. A family of six Rh-O metalloinsertors that vary in the steric bulk and lipophilicity of an ancillary ligand was synthesized and characterized. Regardless of

ancillary ligand identity, these Rh-O metalloinsertors exhibit nanomolar or low-micromolar toxicities and all preferentially target MMR-deficient cancer cells over MMR-proficient cells. Notably, the off-target accumulation of these metalloinsertors in mitochondria is very low. This cellular distribution is in stark contrast with first generation metalloinsertors in which increased ligand lipophilicity led to increased mitochondrial uptake and ultimately non-selective mitochondrial-mediated cell death. We believe robust selectivity of these complexes is retained in part due to their low off-target accumulation in the mitochondria, which is further complemented by the low dosing requirements of these potent therapeutic agents.

Our studies also suggest the high potency of these complexes may be due to a difference in DNA-binding abilities, which is supported by observed differences in which enantiomers can bind to DNA mismatches, differences in ligand buckling at physiological pH, and lipophilicity of the therapeutics, with Rh-O metalloinsertors being dramatically more lipophilic than their first generation counterparts. To better understand the structural basis for this increased potency, crystallographic experiments are underway. A first generation metalloinsertor was previously crystallized with mismatched DNA, and the structure was pivotal in identifying the DNA binding mode of metalloinsertion. Using similar methods, we are working to produce a high-resolution crystal structure of an Rh-O metalloinsertor with mismatched DNA in order to gain structural insights into the increased potency of these new complexes. A significant difference in DNA binding could result in different biological activation of proteins and overall higher potency of these Rh-O metalloinsertors.

Finally, as metalloinsertors are moved towards pre-clinical study, understanding their biological activity in diverse cell culture experiments is essential. We examined a metalloinsertor and the FDA approved chemotherapeutic agent cisplatin in 27 diverse colorectal cancer cell lines. The comparison of these drugs revealed the metalloinsertor to be on average five times more potent than cisplatin in this panel. The potency of the metalloinsertor in different cell lines spanned nearly three orders of magnitude and correlated with whole-cell uptake of rhodium. Additionally, a fluorescent metalloinsertor conjugate was used to quantify the number of lesions in DNA that could be targeted by metalloinsertion, a result that correlated well with the potency of a metalloinsertor across several cell lines, consistent with DNA mismatches as the effective biological target of the metalloinsertor.

The experiments described within this thesis have allowed us to gain a better understanding of the biological activity of rhodium metalloinsertors. We have established that Rh-O metalloinsertors are distinct from first generation metalloinsertors, and that these new metalloinsertors can serve as highly tunable, potent, and mismatch-selective anticancer agents. Furthermore, this potency is observed across diverse cell lines and has been shown to correlate with the number of genomic DNA lesions that can be bound by metalloinsertion. The unique biological activity of these complexes makes them ideal candidates for the treatment of MMR-deficient cancers, and the potency and tunability of Rh-O metalloinsertors will allow for the development of previously unattainable diagnostic and therapeutic tools for MMR-deficiencies.

PUBLISHED CONTENT AND CONTRIBUTIONS

Boyle, K. M.; Barton, J. K. Targeting DNA mismatches with rhodium metalloinsertors. *Inorganica Chimica Acta*. **2016**, 452, 3-11. DOI: 10.1016/j.ica.2016.01.021

K. M. B. participated in the writing of the review article.

Barton, J. K.; Boynton, A. N.; Boyle, K. M. Targeting DNA Mismatches with Coordination Complexes in *DNA-targeting Molecules as Therapeutic Agents*; Waring, M. J., Ed.; Royal Society of Chemistry, **2018**, p 367-390. DOI: 10.1039/9781788012928

K. M. B. participated in the writing of the book chapter.

Boyle, K. M.; Barton, J. K. A Family of Rhodium Complexes with Selective Toxicity towards Mismatch Repair-Deficient Cancers. *J. Am. Chem. Soc.* **2018**, 140, 5612-5624. DOI: 10.1021/jacs.8b02271

K. M. B. participated in the design of the project, performed and analyzed the synthesis and characterization of the small molecules, performed and analyzed the biological assays, and participated in the writing of the manuscript.

Boyle, K. M.; Nano, A.; Day, C.; Barton, J. K. Cellular Target of a Rhodium Metalloinsertor is the DNA Base Pair Mismatch. **2018**, *Submitted*.

K. M. B. participated in the design of the project, performed and analyzed the biological assays, and participated in the writing of the manuscript.

TABLE OF CONTENTS

LIST OF FIGURES, TABLES, AND SCHEMES

Chapter 1

INTRODUCTION*†

1.1 Overview of DNA as a Therapeutic Target

1.1.1 DNA-targeted Small Molecules

DNA has proven to be a rich target for a large range of small-molecule therapeutic drugs. The first DNA-targeting compounds with therapeutic properties were discovered in the 1940s.[1,2] Nitrogen mustards and antifolate drugs were found to cause tumor regression in patients with non-Hodgkin's lymphoma and remission in children with lymphoblastic leukemia, respectively.[2,3] It was found that the anticancer properties of these drugs arise from their interactions with DNA; nitrogen mustards irreversibly alkylate DNA through an aziridinium intermediate to form inter-strand crosslinks and antifolates block DNA synthesis by inhibiting dihydrofolate reductase (DHFR), an enzyme necessary for the synthesis of purine bases.[1,4] Since the discoveries of these therapeutics, the versatility of DNA as a target has been significantly expanded. Therapeutics have been seen to bind covalently to DNA (alkylating agents, platinum drugs), non-covalently interact with DNA (actinomycin D, mitomycins, polyamides), to interfere with protein-DNA complexes (doxorubicin, etoposide), and even target DNA secondary structures such as G-quadruplexes (itarnafloxin, in phase II clinical trials).[5–8]

∗ Adapted from Boyle, K. M.; Barton, J. K. Targeting DNA mismatches with rhodium metalloinsertors. *Inorganica Chimica Acta*. **2016**, 452, 3-11. DOI: 10.1016/j.ica.2016.01.021 and

† Adapted from Barton, J. K.; Boynton, A. N.; Boyle, †K. M. Targeting DNA Mismatches with Coordination Complexes in *DNA-targeting Molecules as Therapeutic Agents*; Waring, M. J., Ed.; Royal Society of Chemistry, **2018**, p 367-390. DOI: 10.1039/9781788012928

These complexes and more DNA-targeting chemotherapeutics have been reviewed recently.[5,9]

In the development of novel metallodrugs, DNA is consistently one of the most exploited targets. As seen in **Figure 1.1**, metal complexes can bind DNA through several different routes, involving both covalent and non-covalent interactions.[10,11] In the covalent binding mode, a small molecule binds directly to DNA to form a covalent lesion to one or more bases, thus impeding DNA replication. In contrast, non-covalent interactions rely on thermodynamic stabilization through electrostatics, hydrogen bonding, hydrophobic interactions, and π-stacking interactions.[12] The majority of complexes that bind DNA non-covalently are either intercalators or groove binders. In intercalation, an aromatic, heterocyclic ligand slips indiscriminately between two adjacent base pairs. This process leads to a partial unwinding of the DNA, increasing the rise of the helix. Groove binding is another common non-covalent binding motif of small molecule therapeutics. In this binding mode, a small molecule that is generally crescent-shaped will tightly bind the minor groove of DNA. Unlike intercalators, which generally lack sequence specificity, groove binders often target AT-rich regions. Moreover, sequence-specific intercalators and groove binders have been prepared.[7,13] Once bound to DNA, these non-covalent complexes primarily cause inhibition of proteins involved in DNA transcription and synthesis, which can lead to cytotoxicity.[14–16] Somewhat recently, a new non-covalent DNA binding mode, termed metalloinsertion, has been observed. In this mode, a large aromatic, heterocyclic ligand inserts into DNA at a destabilized site and ejects the destabilized bases from the helix, without causing an increase in base rise as is seen with intercalators.[17] In contrast

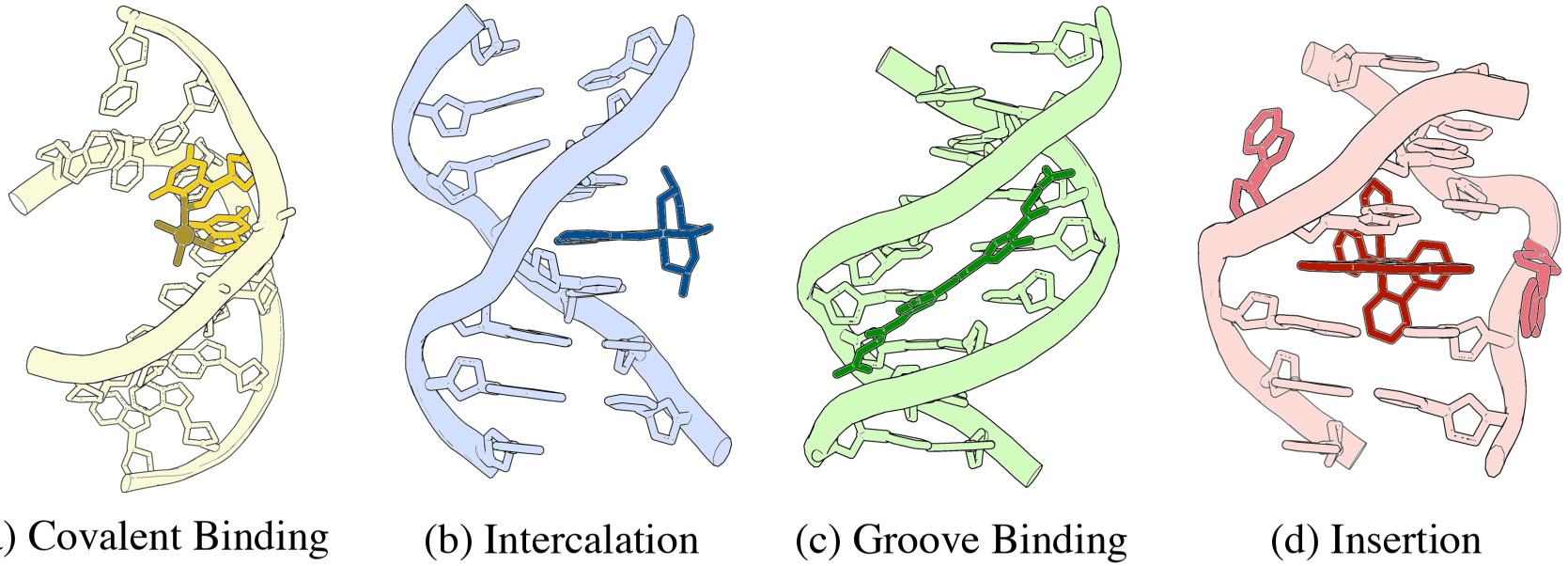

Figure 1.1 Four common binding modes of small molecules to DNA: (a) covalent binding, (b) intercalation, (c) groove binding, and (d) insertion. Structural data from PDB files 1AIO, 454D, 2LWH, and 3GSK, respectively.

to intercalators, metalloinsertors are highly specific for destabilized DNA mismatches, abasic sites, and single base bulges.

1.1.2 Metal-based Anticancer Agents: Successes and Drawbacks

Though DNA-targeting metallodrugs are a significant field of study for many researchers, few have had clinical success due to the general toxicity of heavy metals in the body.[18–20] The most noteworthy and well characterized metallodrug found to bind DNA is *cis*-diamminedichloroplatinum(II) (cisplatin). Cisplatin, the first inorganic chemotherapeutic, was discovered serendipitously by Barnett Rosenberg in 1965 while studying the effects of electric fields on *E. coli* using a platinum electrode.[21] Today, cisplatin and its derivatives, carboplatin and oxaliplatin, remain some of the most frequently used chemotherapeutics with over 50% of all cancer regimens containing one of these platinum drugs.[22] Once within a cell, the chloride ligands of cisplatin are displaced by water.[23] This reactive intermediate binds the N7 position of purine bases to form inter- and intra-strand DNA crosslinks, with the biologically significant adduct believed to be 1,2-intrastrand crosslinks between two adjacent guanine bases.[24] This adduct was structurally characterized using X-ray crystallography in 1995.[25] The 2.6 Å resolution structure shows the bending of the DNA duplex by 40˚ towards the major groove, accompanied by the widening of the minor groove. This lesion is recognized intracellularly by DNA-binding proteins, eventually leading to the apoptotic death of affected cells.[23]

Despite its success in the clinic, cisplatin is not without its drawbacks. Patients treated with cisplatin often experience severe, dose-limiting side-effects such as nausea, vomiting, nephrotoxicity, and ototoxicity.[26] These side-effects occur because cisplatin,

like many chemotherapeutics, is not selective towards cancer cells—it binds DNA inside healthy and cancerous tissues alike. Instead, cisplatin appears primarily to rely on increased uptake by rapidly dividing cancer cells for selectivitiy.[5] Targeted therapy, in which a specific biological signature of cancer drives preferential drug action on cancerous cells over healthy cells, is a clear alternative to these non-specific chemotherapeutics. For example, proteins that are upregulated or expressed exclusively in cancer cells may be exploited as cancer-selective targets.[27] For such protein targets, kinase inhibitors and monoclonal antibodies have found clinical use in the treatment of a variety of cancers.[28,29] For example, cetuximab, a monoclonal antibody, targets and inhibits the epidermal growth factor receptor (EGFR), which is upregulated in several cancers in order to maintain rapid proliferation.[30] In addition to targeting specific proteins, it is also possible to target specific DNA lesions associated with cancer, such as single base-pair mismatches, as described in the next section

1.2 Mismatch Repair Machinery

1.2.1 DNA Damage and Errors in Replication

The DNA within cells is constantly subject to damage by exogenous agents, such as UV light and ionizing radiation, and endogenous modifications, such as depurination, methylation, and errors in replication.[31] Some estimates suggest cells experience up to 10^5 such lesions each day.[32] This damage can lead to interruptions in cellular processes, cell death, and mutations if uncorrected. High fidelity of DNA is essential, and therefore cells have evolved complicated systems to repair many types of DNA damage, known collectively as the DNA damage response. The DNA damage response consists of several processes that identify or correct a broad range of damage, including base excision repair,

nucleotide excision repair, mismatch repair (MMR), and double strand break repair. These processes have all been reviewed recently.[33–36]

MMR machinery is primarily responsible for identifying and correcting replication errors in the form of DNA base-pair mismatches and small insertions and deletions (indels). These lesions result from failed proofreading of replication polymerases and polymerase slippage during replication, respectively. The high fidelity of polymerases and their proofreading exonuclease activities result in a low error rate of ~10^{-7} mismatches per base pair per replication, and this is improved upon by the MMR machinery, which increases fidelity an additional 50-1000-fold.[37] Indels are generated more frequently, especially in repetitive sequences, and are also corrected by the MMR machinery with high fidelity.[33,38]

1.2.2 Mechanisms of the MMR Machinery

The MMR machinery is responsible for identifying and correcting mismatches and indels in newly synthesized DNA, as depicted in **Figure 1.2**. This process involves several major steps. In the first step MutSα (heterodimer of MSH2 and MSH6) or MutSβ (heterodimer of MSH2 and MSH3) recognize and bind the mismatched region. MutSα, which contains 85% of cellular MSH2, is responsible for recognizing and binding all base pair mismatches and small (1-2 base pair) indels while Mutsβ can only efficiently repair indels.[33,39] Next, though the mechanism is not well understood, MutSα undergoes a mismatch and ATP-dependent conformational change that allows for the binding of MutLα, a heterodimer containing MLH1 and PMS2. It is believed that MutLα, which has endonuclease activity when activated by proliferating cell nuclear antigen (PCNA), identifies and nicks the nascent strand of DNA, initiating excision of the DNA strand

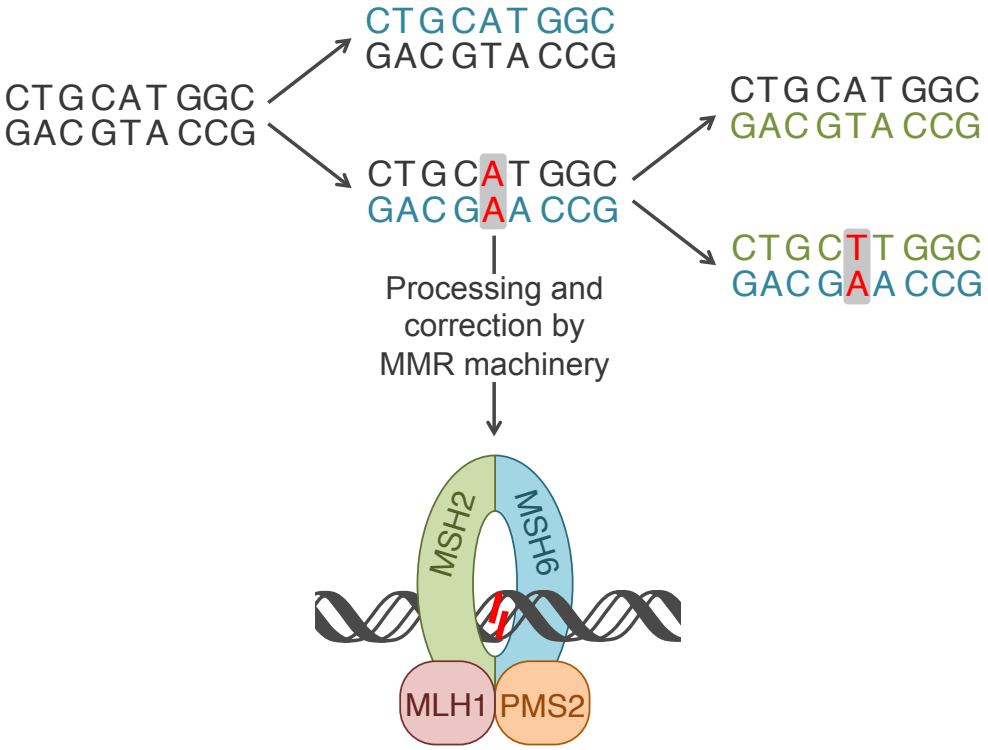

Figure 1.2 Eukaryotic mismatch repair corrects DNA mismatches. Propagation of an AA mismatch through replication, resulting in a TA mutation. The first iteration of replication results in an AA mismatch, shown in red. The mismatch can be processed and repaired by the MMR machinery shown at the bottom. If unprocessed, upon a second iteration of replication the mismatch will result in a mutation, shown in red. Newly synthesized DNA from the first iteration and second iteration is shown in blue and green, respectively.

containing the replication error.[40] Several models exist that explain the removal of the mismatch in both the 5'-to-3' and 3'-to-5' directions. Excision is followed by resynthesis of DNA and ligation. A detailed review on current models in MMR has recently been published.[33]

Deficiencies in either MutSα or MutLα have been associated with a loss of MMR proficiency. MMR deficiencies result in a 50-1000 fold increase in mismatches within the cell. When these mismatches are left unrepaired, they can propagate to form potentially catastrophic mutations in future generations of cells. As such, deficiencies in MMR machinery are associated with many forms of cancer, including nearly 80% of hereditary non-polyposis colon cancers and 15-20% of all solid tumors.[41,42] Additionally, these cancers often show resistance to traditional chemotherapeutics, such as cisplatin and alkylating agents, making them excellent candidates for targeted therapy.[43]

1.2.3 FDA Approved Therapeutics for MMR-deficient Cancers

There are two potential strategies in targeting cancers with deficiencies in MMR: targeting the high mutational load of these cells or targeting the uncorrected DNA lesions themselves. The former is accomplished by the FDA approved therapeutic pembrolizumab. Pembrolizumab is a monoclonal antibody that targets the program cell death 1 (PD-1) receptor on T-cells.[44] In all cells, the major histocompatibility complex (MHC) binds to antigens (foreign or mutated biomolecules) and presents them on the cell surface. T-cells recognize the loaded MHC and attack these compromised cells unless an inhibitory ligand, such as PD-L1 or PD-L2, binds to the PD-1 receptor on T-cells. Mutated proteins, which are particularly abundant in MMR-deficient cancers due to their high mutational frequency, serve as excellent antigens and should signal T-cells to kill

these MMR-deficient cells; however, these cancers adapt to produce large amounts of the inhibitor ligands PD-L1 and PD-L2 in order to shield themselves from T-cells. As such, T-cell essentially deactivate and become suppressed, and therefore they are no longer able to kill the cancerous tissue. Excitingly, pembrolizumab can bind to PD-1 and block the inhibitory interaction between PD-1 and PD-L1, allowing T-cells to stay active in the presence of antigen producing MMR-deficient cells.

Pembrolizumab was first FDA approved in 2014 for the treatment of unresectable or metastatic melanoma, and in 2017 it made history when it was approved for the treatment of solid tumors containing high mutational loads and MMR deficiencies, making it the first anticancer agent to be approved for a specific cancer-associated biomarker.[45,46] Pembrolizumab has allowed doctors to make great strides in the treatment of MMR-deficient cancers, though this treatment strategy is still far from perfect—treatable tumors must express high levels of PD-L1, patients are susceptible to immunogenic side effects, and the treatments themselves are expensive.[47–49] As such, the need for additional therapeutic strategies for MMR-deficient cancers remains crucial. While targeting the high mutational load of MMR-deficient tumors has led to the success of pembrolizumab, there are currently no FDA approved chemotherapeutics that target uncorrected DNA mismatches and idels directly. Such a drug would certainly have a different therapeutic profile than pembrolizumab, which may offer better or synergistic benefits to patients with MMR-deficient tumors.

1.3 Rhodium Metalloinsertors: Probes for DNA Mismatches

1.3.1 Designing a Mismatch-targeting Molecule

The Barton group has historically explored complexes that can non-covalently target specific DNA sequences (such as 5'-TGCA-3' and 5'-py-py-pu-3' sites) as well as the non-conventional A- and Z- forms of DNA, but these targets are not implicated in disease and thus lack therapeutic potential.[13,50–52] DNA mismatches, however, are generic DNA targets that are involved in many types of cancer, as described above. Due to imperfect hydrogen bonding and π-stacking, DNA base pair mismatches are thermodynamically destabilized compared to well-matched DNA.[53] This slight destabilization has been successfully targeted through the use of rhodium metalloinsertors, which contain the sterically expansive 5,6-chrysenequinone diimine (chrysi) ligand.

The chrysi ligand was designed to be larger than traditional intercalating ligands and more akin in size to a well-matched base pair, making it too bulky to simply intercalate into DNA (**Figure 1.3**, left).[16] Instead, chrysi interacts with through insertion at a destabilized site. Insertion, which was originally proposed by L. S. Lerman in 1961, is a DNA binding mode in which a DNA base pair is separated and ejected from the π-stack by the inserting molecule.[54] Rhodium(III) was chosen to be a substitutionally inert metal anchor for the chrysi ligand due to its photophysical properties; rhodium complexes promote DNA strand scission in structurally similar metallointercalators upon photoexcitation.[55] The rhodium center also anchors two ancillary ligands, which add bulk to the complexes and limit how the chrysi ligand can interact with DNA, largely

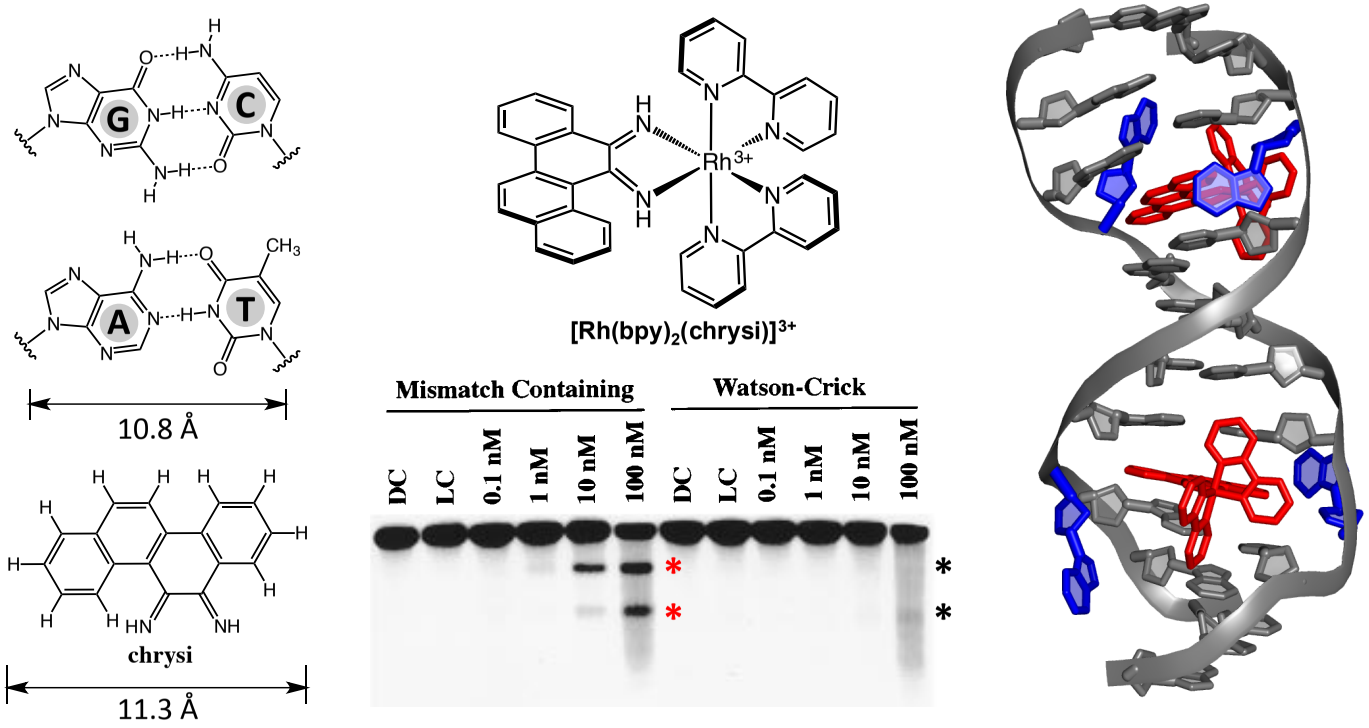

Figure 1.3 Structure and activity of a rhodium metalloinsertor. (Left) The chrysi ligand is 0.5 Å wider than a well matched base pair, making intercalation unfavorable. (Upper middle) The structure of $[Rh(bpy)_2(chrysi)]^{3+}$, which is capable of site-selective photocleavage at a single CC mismatch in a 2725-base pair linearized plasmid (lower middle), resulting in two photocleavage products (red *). The equivalent well-matched plasmid is not cleaved by the metal complex (black *). (Right) Mismatch selectivity is cause by selective metalloinsertor (red) binding to mismatched base pairs (blue) in DNA, which has been observed crystallographically. Structural data from PDB 3GSK.

preventing indiscriminant intercalation.[56] These ancillary ligands can also be selected to tune DNA binding and cellular uptake properties, as discussed below.

1.3.2 Targeting DNA Mismatches with Rhodium Metalloinsertors

The first generation metalloinsertor, $[Rh(bpy)_2(chrysi)]^{3+}$ (bpy = 2,2'-bipyridine), is easily synthesized via a base-catalyzed condensation reaction between $[Rh(bpy)_2(NH_3)_2]^{3+}$ and 5,6-chrysene quinone.[57] As predicted, $[Rh(bpy)_2(chrysi)]^{3+}$ can selectively bind DNA base pair mismatches with nanomolar affinities and photocleave the DNA backbone adjacent to the mismatch when irradiated with UV-light.[17] This process is enantioselective, meaning only the right-handed Δ-enantiomer can bind right-handed, B-form DNA. A series of binding affinity assays were employed to determine the specificity of $[Rh(bpy)_2(chrysi)]^{3+}$. For instance, when incubated with a 2725 base pair linearized plasmid containing a single CC mismatch, $[Rh(bpy)_2(chrysi)]^{3+}$ selectively binds and photocleaves the DNA solely at the mismatched site (**Figure 1.3**, middle).[58] No photocleavage is observed with the analogous well-matched plasmid. $[Rh(bpy)_2(chrysi)]^{3+}$ was also incubated with DNA segments containing all possible DNA mismatches and multiple different sequence contexts in which the base pairs flanking the mismatch were varied.[59] Through these experiments, it was determined that $[Rh(bpy)_2(chrysi)]^{3+}$ has >1000-fold preference for targeting mismatched sites over well-matched sites. Additionally, the complex binds and cleaves 80% of all DNA mismatches upon irradiation, irrespective of sequence context. Not surprisingly, the binding affinity of $[Rh(bpy)_2(chrysi)]^{3+}$ towards a mismatch correlates strongly with the thermodynamic destabilization of the mismatch; highly destabilized mismatches (such as CC, CA, and CT mismatches) are easily recognized by $[Rh(bpy)_2(chrysi)]^{3+}$, whereas more stabilized

mismatches, specifically mismatches containing guanine, are not preferentially cleaved by the complex. These complexes have also been seen to bind abasic sites and single-base bulges in DNA.[60,61]

A crystal structure at 1.1 Å resolution of $[Rh(bpy)_2(chrysi)]^{3+}$ with a 12-mer oligonucleotide containing two AC mismatches further elucidated the binding mode of the complex to be metalloinsertion.[62] Unlike classical metallointercalators, the metalloinsertor binds DNA via the minor groove and results in little distortion to the DNA backbone. Instead, the DNA accommodates the inserting ligand through the ejection of the mismatched bases out of the π-stack and into the major and minor grooves. This binding mode was verified with an additional crystal structure of the complex bound to an AA mismatch (**Figure 1.3**, right), as well as a solution NMR structure of the complex with DNA containing a CC mismatch.[63,64] This structure provides additional insight into why G-containing mismatches are not detected by metalloinsertors; these highly stable mismatches are not easily ejected from the base-stack, so chrysi cannot displace mismatches at these sites.

1.4 Rhodium Metalloinsertors Inside the Cell

1.4.1 Targeting MMR-deficiencies with Rhodium Metalloinsertors

The therapeutic potential of rhodium metalloinsertors was explored after experiments showed their ability to bind DNA base pair mismatches selectively. It was hypothesized that metalloinsertors would have increased toxicity towards cells that contain an increased number of DNA mismatches, as is present in MMR-deficient cells. To test this hypothesis, an enzyme-linked immunosorbent assay (ELISA) for cellular proliferation was performed with two colorectal cancer cell lines, the HCT116O cell line,

which is MMR-deficient, and the MMR-proficient HCT116N cell line. These cell lines, which originate from the MLH1 deficient HCT116 parent cell line, are isogenically matched; the HCT116N cell line is transfected with human chromosome 3, which encodes for a functioning MLH1 gene, and the HCT116O cell line is transfected with human chromosome 2, leaving it MMR-deficient.[65] $[Rh(bpy)_2(chrysi)]^{3+}$ was found to have increased potency in the MMR-deficient cell line.[66]

As with the DNA binding studies, only the Δ enantiomer was biologically active, suggesting the compounds do not decompose or racemize within the cell.[66] This unique activity, the ability to selectively kill MMR-deficient cells over their MMR-proficient counterparts, has been found to be common to many rhodium metalloinsertor.[67–69] Importantly, while general to metalloinsertors, these are the only complexes known to exhibit this type of selectivity, with common chemotherapeutics such as cisplatin and the DNA-alkylating agent N-methyl-N'-nitro-N-nitrosoguanidine (MNNG) showing the opposite trend (**Figure 1.4**).[43] These results have been additionally verified in MSH2-deficient mouse embryonic fibroblasts and an inducible MSH1-deficient cell line, showing that the characteristic activity of these complexes towards MMR-deficient cell lines is dependent on the MMR-deficient phenotype rather than a unique feature of the HCT116 cell lines.[66,70]

The cell-selective inhibitory activity of metalloinsertors is somewhat surprising considering that these complexes interact only non-covalently with DNA and even MMR-deficient cells contain relatively few mismatches. Like other non-covalent DNA intercalators and groove binders, it is possible that rhodium metalloinsertors bind DNA mismatches and disrupt transcription or replication processes, leading to selective

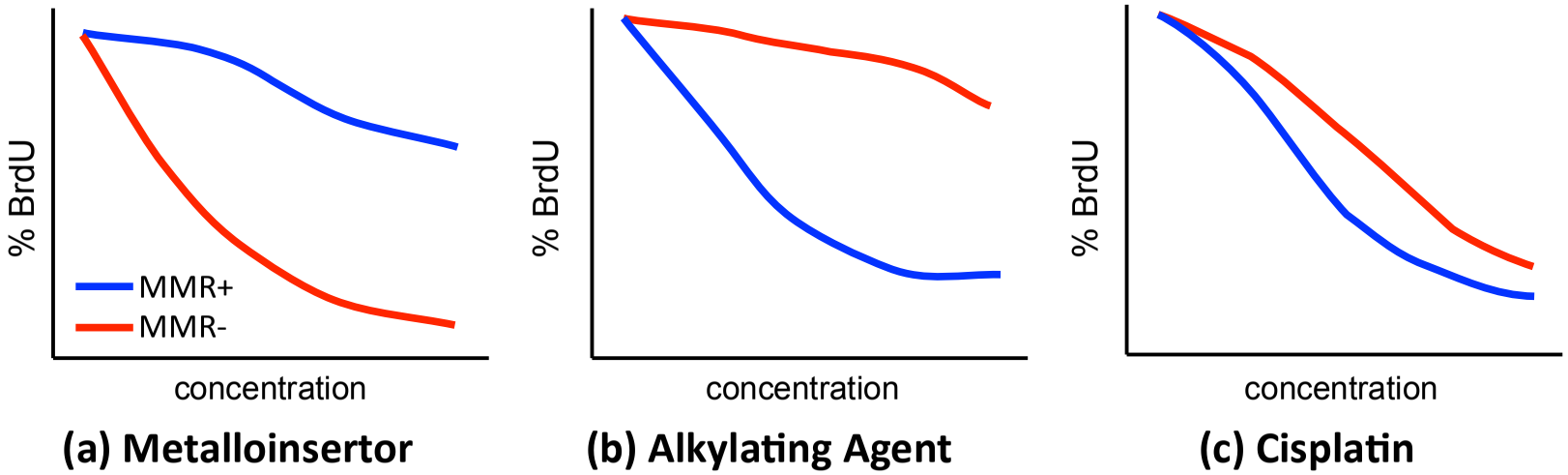

Figure 1.4 Anti-proliferative activity of anticancer agents. The anti-proliferative behavior of (a) a generic rhodium metalloinsertor, (b) the alkylating agent, MNNG, and (c) the ubiquitous therapeutic, cisplatin, as measured via BrdU-incorporation ELISA in MMR-deficient (MMR-, red) and MMR-proficient (MMR+, blue) cells. It is of interest to note that both the alkylating agent and cisplatin preferentially kill the MMR proficient cell line. This result is reflective of the resistance many MMR-deficient cancers exhibit towards these classes of therapeutics.

cytotoxicity in MMR-deficient cells. Ongoing research in our lab aims to better understand the activity of rhodium metalloinsertors and the mechanisms that lead to this selective cell death.

1.4.2 DNA-binding affinity and subcellular localization of metalloinsertors

As discussed previously, the design of the inserting chrysi ligand was central to obtaining mismatch specificity. It is important to note, however, that the design of the ancillary ligands has also proven to be important. The metalloinsertion binding mode places the ancillary ligands of the rhodium complexes in close proximity to the DNA bases and backbone. For this reason, several structure-function studies have been performed to determine the effect of the ancillary ligands on biological activity. In one study, the ancillary ligands were varied in size from small ammine groups to bulky 4,7-diphenyl-phenanthroline (DIP) groups.[71] The binding affinities to mismatched DNA spanned over 3 orders of magnitude and correlated well to biological activity, with higher affinity mismatch-binding complexes being more selective than their low-affinity counterparts. Again, none of the complexes showed selective inhibition of the MMR-proficient cells.

Differences in binding affinity, however, are not the sole predictor of biological activity. The activities of two structurally similar metalloinsertors, $[Rh(DPAE)_2(chrysi)]^{3+}$ and $[Rh(PrDPA)_2(chrysi)]^{3+}$ (DPAE = 2-(di(pyridin-2-yl)amino)ethanol, PrDPA =N-propyl-N-(pyridin-2-yl)pyridin-2-amine), were examined to explore in more detail the importance of uptake and subcellular localization (**Figure 1.5**).[72] These two complexes have similar mismatch binding affinities and differ only in the presence of either ethanol or propyl modified HDPA (2,2'-dipyridylamine) ligands.

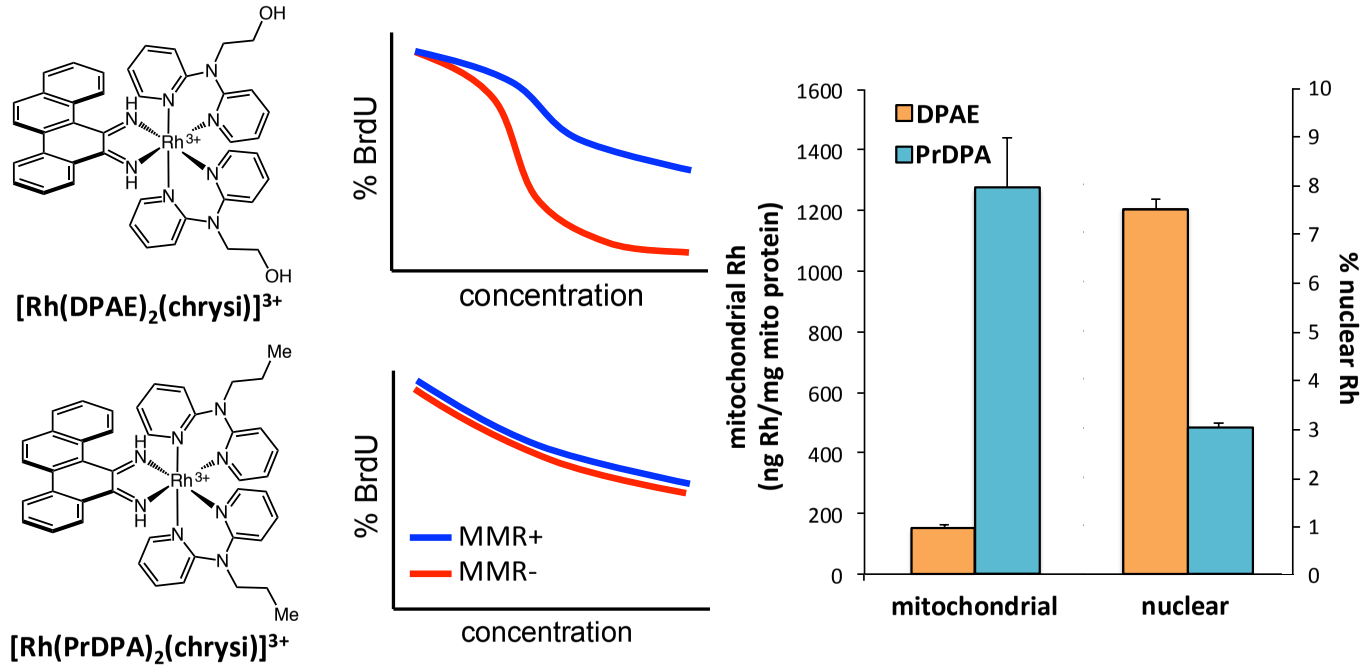

Figure 1.5 Biological activity of two structurally similar metalloinsertors. (Left) Structure of two similar metalloinsertors, $[Rh(DPAE)_2(chrysi)]^{3+}$ and $[Rh(PrDPA)_2(chrysi)]^{3+}$. (Middle) Cell proliferation observations (as measured via BrdU-incorporation ELISA) for each metalloinsertors, which contain hydrophilic (top) or lipophilic (bottom) ligands. Despite having similar DNA binding affinities and similar whole-cell uptake, $[Rh(DPAE)_2(chrysi)]^{3+}$ shows selective behavior toward MMR- cells, whereas $[Rh(PrDPA)_2(chrysi)]^{3+}$ exhibits no selectivity. (Right) This is explained by the subcellular localization profiles of each complex. While both complexes enter the nucleus at high enough concentrations for DNA binding, $[Rh(PrDPA)_2(chrysi)]^{3+}$ has significant localization into the mitochondria, leading to off target and non-selective cytotoxicity.

The addition of these ligands does, however, lead to a difference in lipophilicity as measured by the partition constant. As expected, the more lipophilic complex,$[Rh(PrDPA)_2(chrysi)]^{3+}$, showed significantly higher cellular uptake than $[Rh(DPAE)_2(chrysi)]^{3+}$, making its non-selective biological activity initially surprising. However, upon subcellular fractioning and analysis using inductively coupled plasma spectrometry (ICP-MS), it became clear that the subcellular localization of these two complexes provided an explanation for their activities. $[Rh(PrDPA)_2(chrysi)]^{3+}$ showed a 10-fold increase in mitochondrial uptake over $[Rh(DPAE)_2(chrysi)]^{3+}$. Although more $[Rh(PrDPA)_2(chrysi)]^{3+}$ was also found in the nucleus of the cells, the percentage of total Rh found within the nucleus is higher for $[Rh(DPAE)_2(chrysi)]^{3+}$. These results suggest that localization of complexes to the mitochondria eradicates their biological selectivity for MMR-deficient cells and leads to MMR-independent death of both cell lines. Importantly, these findings support the hypothesis that metalloinsertors achieve their cell selectivity through binding *nuclear* DNA mismatches, not mitochondrial DNA.

The effects of subcellular localization were further examined with a larger family of complexes that differed primarily in lipophilicity.[68] With the exception of $[Rh(DIP)_2(chrysi)]^{3+}$, all complexes display similar binding affinities to mismatched DNA in the 10^6 to 10^7 M^{-1} range. Once again, it was found that biological selectivity correlated not with overall cellular uptake or nuclear localization, but instead with mitochondrial localization. As expected, the more lipophilic, greasy cations showed the highest mitochondrial localization, which correlated with elimination of biological selectivity.[73] The more hydrophilic complexes had significantly lower localization to the mitochondria, which correlated with higher cell selectivity. These studies highlighted the

importance not only of cellular uptake but also considerations of subcellular localization. These studies furthermore suggested that off-target effects, such as mitochondrial targeting, are detrimental to the biological function of metalloinsertors.

1.4.3 Current Design of Rhodium Metalloinsertors

Recently, a new family of potent rhodium metalloinsertors based on $[Rh(DPE)(chrysi)(phen)]^{2+}$ (DPE=1,1- di(pyridine-2-yl)ethan-1-ol, phen=1,10-phenanthroline) has been examined (**Figure 1.6**).[69] Unlike previous generations of metalloinsertors, these complexes contain an unusual Rh-O bond through the coordination of their pyridyl-ethanol ligands. These Rh-O containing metalloinsertors are more potent than cisplatin and display optimal differential cellular activity in the nanomolar range, as much as two orders of magnitude more potent than earlier generations of complexes. Surprisingly, this scaffold is robust to many substitutions of the oxygen-containing ligand: replacing the dangling pyridyl group of DPE with a small methyl group, a phenyl group, or a greasy hexyl group all lead to improved, nanomolar cytotoxicity in MTT assays. Furthermore, and surprisingly, both the Δ and Λ enantiomers of these new complexes bind DNA with similar affinity *in vitro* and both show differential cell-selective activity in MTT assays.

Remarkably, the increased potency and selectivity of $[Rh(DPE)(chrysi)(phen)]^{2+}$ and its derivatives is not a result of increased DNA binding or localization. For example, in comparison to the complex $[Rh(phzi)(NH_3)_4]^{3+}$, a selective metalloinsertor that utilizes the expansive benzo[a]phenazine quinone diimine (phzi) ligand, $[Rh(DPE)(chrysi)(phen)]^{2+}$ possesses an order of magnitude *lower* mismatch binding affinity, similar cellular uptake and mitochondrial concentrations, and slightly lower

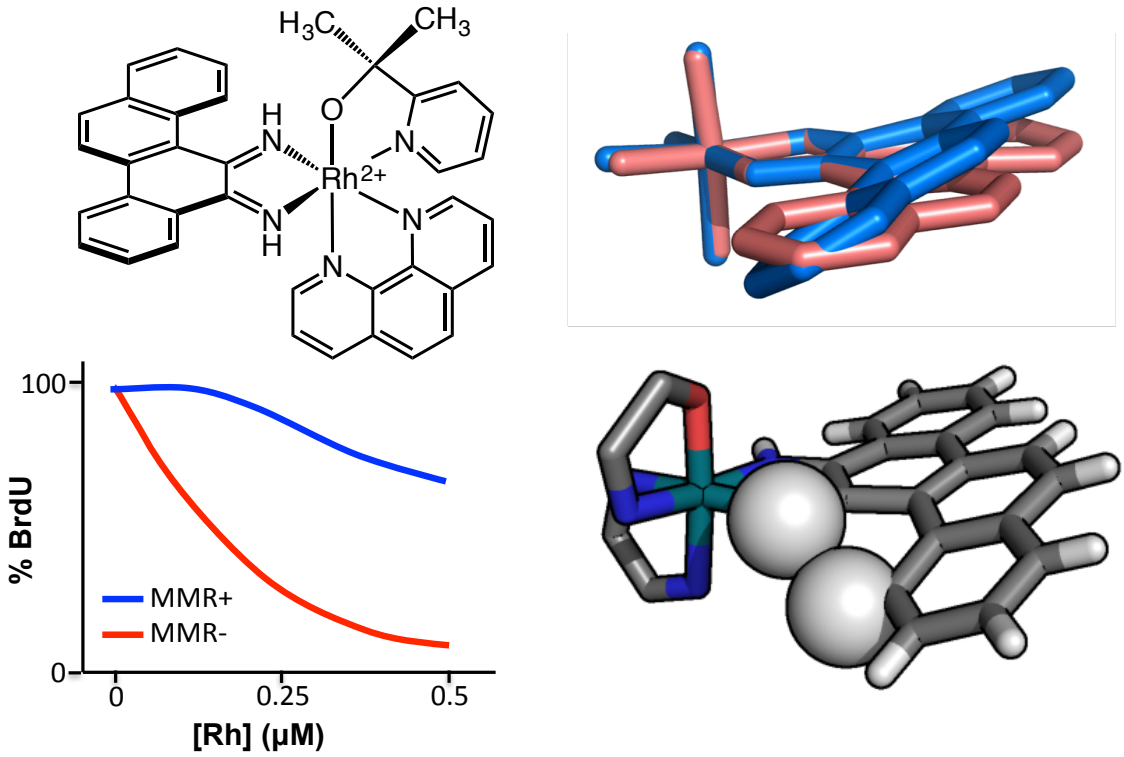

Figure 1.6 A new family of rhodium metalloinsertors with unique activity. (Top left) The structure of $[Rh(phen)(chrysi)(PPO)]^{2+}$ and its anti-proliferative activity (bottom left) as measured via BrdU-incorporation ELISA. $[Rh(phen)(chrysi)(PPO)]^{2+}$ is currently the most selective and potent metalloinsertor. (Top right) When the inserting chrysi ligand of $[Rh(phen)(chrysi)(DPE)]^{2+}$ (pale blue) is overlain with the chrysi ligand of of $[Rh(bpy)_2(chrysi)]^{3+}$, (pink) there are is a noticeable buckling of the $[Rh(phen)(chrysi)(DPE)]^{2+}$ chrysi ligand due to steric clashing with an imine proton with high pKa value (bottom right).

nuclear concentration. Despite these differences, $[Rh(DPE)(chrysi)(phen)]^{2+}$ shows comparable selectivity towards MMR-deficient cells as the tetrammine complex but is nearly 4-fold more potent than $[Rh(phzi)(NH_3)_4]^{3+}$. Initially, it seemed possible that the increased potency and racemic binding could be due to a labile Rh-O bond, leading to covalent DNA binding and racemization within the cell. However, these possibilities were eliminated using several *in vitro* tests of stability. It appears that the enantiomeric activity of these complexes is authentic, with both Δ and Λ enantiomers being able to kill MMR-deficient cells selectively without racemization.

One apparent difference between the Rh-O containing metalloinsertors and previous generations are dramatic changes in the pKa of the chrysi imine protons. The pKa of the first generation complex, $[Rh(bpy)_2(chrysi)]^{3+}$, is 5.6 ± 0.2; thus the complex is deprotonated at cellular pH. The deprotonation of the chrysi ligand relieves steric clashes between its imine proton and aromatic ring system protons, allowing the chrysi ligand to lay planar (**Figure 1.6**, right). This planarity can be seen in the crystal structure of $[Rh(bpy)_2(chrysi)]^{3+}$ bound to a DNA mismatch. The Rh-O containing metalloinsertors have significantly higher pKa values of 8.3-8.9, meaning the chrysi ligand cannot deprotonate at cellular pH. To relieve steric clashing, the chrysi ligand must instead buckle relative to $[Rh(bpy)_2(chrysi)]^{3+}$. This buckling can be seen in the crystal structure of $[Rh(DPE)(chrysi)(phen)]^{2+}$. While we still believe the binding mode of these complexes to be metalloinsertion, it appears that this significant structural change in the inserting ligand of these complexes must create a slightly different DNA lesion than $[Rh(bpy)_2(chrysi)]^{3+}$. The new lesion or lesions must accommodate both the Δ and Λ enantiomers. Within the cell, this lesion may be more easily recognized by proteins

activating necrotic cell death than lesions caused by previous metalloinsertors, leading to the increased potency and selectivity of these complexes. Clearly much needs to be done to elucidate the basis of the high potency and cell selectivity of these new complexes, both from a structural standpoint and with regard to understanding the biological fate of the complexes.

1.5 Conclusion

Rhodium metalloinsertors constitute a unique family of transition metal complexes that selectively bind DNA base pair mismatches and preferentially inhibit proliferation and survival of MMR-deficient cells. Over the years, the design of these complexes has improved significantly, traversing from micromolar toxicities now into the nanomolar range. Thus a unique family of rhodium metalloinsertors with nanomolar potencies and high selectivity for MMR-deficient cell lines has now been characterized, bringing these complexes into the realm of therapeutic interest.[69]

Based on the metalloinsertive binding mode of $[Rh(bpy)_2(chrysi)]^{3+}$, elucidated through solid and solution state structures, as well as *in vitro* and *in cellulo* work performed on the extensive family of metalloinsertors, we hypothesize that these complexes bind DNA mismatches within MMR-deficient cells, and that this Rh-DNA lesion is recognized by proteins and cellular machinery that eventually lead the cell to necrosis. Unlike cisplatin, these complexes do not appear to form covalent adducts with DNA. Instead, it is possible that the non-covalent binding of metalloinsertors inhibits proteins involved in DNA processes such as transcription or replication, similar to other non-covalent DNA groove binders and intercalators. In such a case, their activity may only be evident in MMR-deficient cells containing increased concentrations of

mismatches, leading to their observed selectivity. It is possible that the lesion formed by the more potent and selective complexes of the current generation, that can accommodate the Δ and Λ enantiomer, may also be more recognizable in the cell, or processed more efficiently to produce necrosis. Recent work on metalloinsertors has emphasized examining the versatility of Rh-O metalloinsertors, characterizing the structures of metalloinsertors bound to their target mismatches, and understanding the biological activity of these metalloinsertors in diverse cellular environments. Future work will use what is established in this thesis to explore new challenges, such as identifying proteins and pathways involved in metalloinsertor processing and developing future generations of metalloinsertors with improved potency or selectivity for use as a foundation for a new family of chemotherapeutics.

Indeed what has been clear from these studies at the outset is that transition metal chemistry offers a rich variety of means to target DNA sites along with novel methods to characterize their fates inside cells. Cisplatin, despite its simplicity in structure and relative lack of specificity in cellular targeting, has proven to be a powerfully important therapeutic. We expect that greater specificity in cellular targeting along with greater specificity in DNA targeting can only aid us in the development of new strategies upon which to build and potentially new potent and *selective* metal compounds as cancer therapeutics.

1.6 References

(1) Gilman, A.; Philips, F. S. *Science (80-.).* **1946**, *103*, 409–436.

(2) Farber, S.; Diamond, L. K.; Mercer, R. D.; Sylvester Jr, R. F.; Wolff, J. A. *N. Engl. J. Med.* **1948**, *238*, 787–793.

(3) Goodman, L. S.; Wintrobe, M. M.; Dameshek, W.; Goodman, M. J.; Gilman, A.; McLennan, M. T. *J. Am. Med. Assoc.* **1946**, *132*, 126–132.

(4) Li, M. C.; Hertz, R.; Bergenstal, D. M. *N. Engl. J. Med.* **1958**, *259*, 66–74.

(5) Hurley, L. H. *Nat. Rev. Cancer* **2002**, *2*, 188–200.

(6) Palchaudhuri, R.; Hergenrother, P. J. *Curr. Opin. Biotechnol.* **2007**, *18*, 497–503.

(7) White, S.; Szewczyk, J. W.; Turner, J. M.; Baird, E. E.; Dervan, P. B. *Nature* **1998**, *391*, 468–471.

(8) Shalaby, T.; Fiaschetti, G.; Nagasawa, K.; Shin-ya, K.; Baumgartner, M.; Grotzer, M. *Molecules* **2013**, *18*, 12500–12537.

(9) Cheung-Ong, K.; Giaever, G.; Nislow, C. *Chem. Biol.* **2013**, *20*, 648–659.

(10) Komor, A. C.; Barton, J. K. *Chem. Commun.* **2013**, *49*, 3617–3630.

(11) Zeglis, B. M.; Pierre, V. C.; Barton, J. K. *Chem Commun* **2007**, *44*, 4565–4579.

(12) Paul, A.; Bhattacharya, S. *Curr. Sci.* **2012**, *102*, 212–231.

(13) Krotz, A. H.; Hudson, B. P.; Barton, J. K. *J. Am. Chem. Soc.* **1993**, *115*, 12577–12578.

(14) Baraldi, P. G.; Bovero, A.; Fruttarolo, F.; Preti, D.; Tabrizi, M. A.; Pavani, M. G.; Romagnoli, R. *Med. Res. Rev.* **2004**, *24*, 475–528.

(15) Wheate, N. J.; Brodie, C. R.; Collins, J. G.; Kemp, S.; Aldrich-Wright, J. R. *Mini Rev. Med. Chem.* **2007**, *7*, 627–648.

(16) Zeglis, B. M.; Pierre, V. C.; Barton, J. K. *Chem. Commun.* **2007**, *44*, 4565–4579.

(17) Jackson, B. A.; Barton, J. K. *J. Am. Chem. Soc.* **1997**, *119*, 12986–12987.

(18) Barbier, O.; Jacquillet, G.; Tauc, M.; Cougnon, M.; Poujeol, P. *Nephron - Physiol.* **2005**, *99*, 105–110.

(19) Shi, H.; Hudson, L. G.; Liu, K. J. *Free Radic. Biol. Med.* **2004**, *37*, 582–593.

(20) Domingo, J. L. *J. Toxicol. Environ. Health* **1994**, *42*, 123–141.

(21) Rosenberg, B.; Van Camp, L.; Krigas, T. *Nature* **1965**, *205*, 698–699.

(22) Wheate, N. J.; Walker, S.; Craig, G. E.; Oun, R. *Dalt. Trans.* **2010**, *39*, 8113–8127.

(23) Jamieson, E. R.; Lippard, S. J. *Chem. Rev.* **1999**, *99*, 2467–2498.

(24) Eastman, A. *Biochemistry* **1986**, *25*, 3912–3915.

(25) Takahara, P. M.; Rosenzweig, A. C.; Frederick, C. A.; Lippard, S. J. **1995**, *377*, 649–652.

(26) Kelland, L. *Nat. Rev. Cancer* **2007**, *7*, 573–584.

(27) Weidmann, A. G.; Komor, A. C.; Barton, J. K. *Comments Inorg. Chem.* **2014**, *34*, 1–10.

(28) Scaltriti, M.; Baselga, J. *Clin. Cancer Res.* **2006**, *12*, 5268–5272.

(29) Zhang, J.; Yang, P. L.; Gray, N. S. *Nat. Rev. Cancer* **2009**, *9*, 28–39.

(30) Van Cutsem, E.; Köhne, C.-H.; Hitre, E.; Zaluski, J.; Chang Chien, C.-R.; Makhson, A.; D'Haens, G.; Pintér, T.; Lim, R.; Bodoky, G.; others. *N. Engl. J. Med.* **2009**, *360*, 1408–1417.

(31) Dexheimer, T. S. In *DNA Repair of Cancer Stem Cells*; Springer: Dordrecht, 2013; pp 19–32.

(32) Hoeijmakers, J. H. J. *N. Engl. J. Med.* **2009**, *361*, 1475–1485.

(33) Kunkel, T. A.; Erie, D. A. *Annu. Rev. Genet.* **2015**, *49*, 291–313.

(34) Schärer, O. D. *Cold Spring Harb. Perspect. Biol.* **2013**, *5*, a012609.

(35) Dianov, G. L.; Hübscher, U. *Nucleic Acids Res.* **2013**, *41*, 3483–3490.

(36) Panier, S.; Boulton, S. J. *Nat. Rev. Mol. Cell Biol.* **2014**, *15*, 7–18.

(37) Kunkel, T. A. *J. Biol. Chem.* **2004**, *279*, 16895–16898.

(38) Tran, H. T.; Keen, J. D.; Kricker, M.; Resnick, M. A.; Gordenin, D. A. *Mol. Cell. Biol.* **1997**, *17*, 2859–2865.

(39) Modrich, P. *J. Biol. Chem.* **2006**, *281*, 30305–30309.

(40) Kadyrov, F. A.; Dzantiev, L.; Constantin, N.; Modrich, P. *Cell* **2006**, *126*, 297–308.

(41) Kolodner, R. D. *Trends Biochem. Sci.* **1995**, *20*, 397–401.

(42) Arzimanoglou, I. I.; Gilbert, F.; Barber, H. R. K. *Cancer* **1998**, *82*, 1808–1820.

(43) Fink, D.; Aebi, S.; Howell, S. B. *Clin. Cancer Res.* **1998**, *4*, 1–6.

(44) Peters, S.; Kerr, K. M.; Stahel, R. *Cancer Treat. Rev.* **2018**, *62*, 39–49.

(45) Sul, J.; Blumenthal, G. M.; Jiang, X.; He, K.; Keegan, P.; Pazdur, R. *Oncologist* **2016**, *21*, 643–650.

(46) FDA. FDA approves first cancer treatment for any solid tumor with a specific genetic feature.

(47) Pollack, M. H.; Betof, A.; Dearden, H.; Rapazzo, K.; Valentine, I.; Brohl, A. S.; Ancell, K. K.; Long, G. V.; Menzies, A. M.; Eroglu, Z.; Johnson, D. B.; Shoushtari, A. N. *Ann. Oncol.* **2018**, *29*, 250–255.

(48) Cagle, P. T.; Bernicker, E. H. *Arch. Pathol. Lab Method* **2015**, *139*, 1477.

(49) Tartari, F.; Santoni, M.; Burattini, L.; Mazzanti, P.; Onofri, A.; Berardi, R. *Cancer Treat. Rev.* **2016**, *48*, 20–24.

(50) Sitlani, A.; Long, E. C.; Pyle, A. M.; Barton, J. K. *J. Am. Chem. Soc.* **1992**, *114*, 2303–2312.

(51) Mei, H.-Y.; Barton, J. K. *Proc. Natl. Acad. Sci.* **1988**, *85*, 1339–1343.

(52) Barton, J. K.; Raphael, A. L. *Proc. Natl. Acad. Sci.* **1985**, *82*, 6460–6464.

(53) Pan, S.; Sun, X.; Lee, J. K. *Int. J. Mass Spectrom.* **2006**, *253*, 238–248.

(54) Lerman, L. S. *J. Mol. Biol.* **1961**, *3*, 18--IN14.

(55) Uchida, K.; Pyle, A. M.; Morii, T.; Barton, J. K. *Nucleic Acids Res.* **1989**, *17*, 10259–10279.

(56) Suri, Asif, K.; Mao, B.; Amin, S.; Geacintov, N. E.; Patel, D. J. *J. Mol. Biol.* **1999**, *292*, 289–307.

(57) Zeglis, B. M.; Barton, J. K. *Nat. Protoc.* **2007**, *2*, 357–371.

(58) Jackson, B. A.; Alekseyev, V. Y.; Barton, J. K. *Biochemistry* **1999**, *38*, 4655–4662.

(59) Jackson, B. A.; Barton, J. K. *Biochemistry* **2000**, *39*, 6176–6182.

(60) Ernst, R. J.; Komor, A. C.; Barton, J. K. *Biochemistry* **2011**, *50*, 10919–10928.

(61) Zeglis, B. M.; Boland, J. A.; Barton, J. K. *J. Am. Chem. Soc.* **2008**, *130*, 7530–7531.

(62) Pierre, V. C.; Kaiser, J. T.; Barton, J. K. *Proc. Natl. Acad. Sci.* **2007**, *104*, 429–434.

(63) Zeglis, B. M.; Pierre, V. C.; Kaiser, J. T.; Barton, J. K. *Biochemistry* **2009**, *48*, 4247–4253.

(64) Cordier, C.; Pierre, V. C.; Barton, J. K. *J. Am. Chem. Soc.* **2007**, *129*, 12287–12295.

(65) Maida, M.; Aebi, S.; Fink, D.; Howell, S. B.; Los, G. *J. Natl. Cancer Inst.* **1997**, *89*, 1537–1541.

(66) Hart, J. R.; Glebov, O.; Ernst, R. J.; Kirsch, I. R.; Barton, J. K. *Proc. Natl. Acad. Sci.* **2006**, *103*, 15359–15363.

(67) Ernst, R. J.; Song, H.; Barton, J. K. *J. Am. Chem. Soc.* **2009**, *131*, 2359–2366.

(68) Komor, A. C.; Schneider, C. J.; Weidmann, A. G.; Barton, J. K. *J. Am. Chem. Soc.* **2012**, *134*, 19223–19233.

(69) Komor, A. C.; Barton, J. K. *J. Am. Chem. Soc.* **2014**, *136*, 14160–14172.

(70) Bailis, J. M.; Gordon, M. L.; Gurgel, J. L.; Komor, A. C.; Barton, J. K.; Kirsch, I. R. *PLoS One* **2013**, *8*, e78726.

(71) Ernst, R. J.; Song, H.; Barton, J. K. *J. Am. Chem. Soc.* **2009**, *131*, 2359–2366.

(72) Weidmann, A. G.; Komor, A. C.; Barton, J. K. *Philisophocal Trans. R. Soc.* **2013**, *371*, 20120117.

(73) Modica-Napolitano, J. S.; Aprille, J. R. *Adv. Drug Deliv. Rev.* **2001**, *49*, 63–70.

Chapter 2

A FAMILY OF RHODIUM COMPLEXES WITH SELECTIVE TOXICITY TOWARD MISMATCH REPAIR-DEFICIENT CANCERS*

2.1 Introduction

Over the past 70 years, DNA and its associated metabolic processes have proven to be fruitful targets for the design of new therapeutic agents.[1] Many of the most common FDA-approved chemotherapeutics work by binding DNA, such as the DNA-crosslinking agent cisplatin and the DNA-intercalating agent doxorubicin.[2–5] Despite the prevalence of these drugs in the clinic, there are many drawbacks to their design and mechanisms of action. In many cases, the drugs target a generic DNA structure that is common to both healthy and cancerous cells. The incidental targeting of healthy tissue can result in dramatic and often dose-limiting side effects, such as emesis and nephrotoxicity.[6] To circumvent these off-target effects, it is essential to identify new therapeutic targets that are almost exclusively found within cancerous tissues and cells.

In our research, we focus on one such target: DNA base pair mismatches. Mismatches occur regularly in cells due to polymerase errors or interaction with exogenous compounds.[7] In healthy cells, these errors are corrected by the mismatch repair (MMR) machinery of the cell. However, in many solid tumors or tumors of Lynch syndrome patients, mutations in MMR proteins severely down-regulate or completely inactivate repair.[8,9] As a result, these cancers contain a relative abundance of DNA base

---

∗ Adapted from Boyle, K. M.; Barton, J. K. A Family of Rhodium Complexes with Selective Toxicity towards Mismatch Repair-Deficient Cancers. *J. Am. Chem. Soc.* **2018**, 140, 5612-5624. DOI: 10.1021/jacs.8b02271

pair mismatches compared to healthy cells, making mismatches a potential biomarker for selective cancer therapy.

Mismatched base pairs have been targeted through the design of metal complexes, called rhodium metalloinsertors, which selectively and non-covalently bind these lesions.[10] Rhodium metalloinsertors contain a sterically expansive aromatic chrysi (5,6-chrysenequinone diimine) ligand that is capable of π-stacking with DNA bases. Due to steric bulk, however, the chrysi ligand is unable to easily intercalate into well-matched DNA, and instead primarily interacts with DNA at thermodynamically destabilized sites, such as mismatches or abasic sites.[11] The ability of a prototypical metalloinsertor, $[Rh(bpy)_2(chrysi)]^{3+}$ (bpy = 2,2'-bipyridine), to selectively bind DNA mismatches has been verified using both *in vitro* binding assays and crystallographic studies.[12–15] Crystallographic and NMR studies show that this complex binds DNA mismatches *via* metalloinsertion, a non-covalent binding mode in which the complex inserts into DNA at the mismatched site from the minor groove, ejects the mismatched DNA bases, and π-stacks with the flanking well-matched base pairs.[14] This mismatch-targeting ability has also been suggested by human cell culture experiments, with metalloinsertors exhibiting enhanced cytotoxicity in MMR-deficient cell lines relative to their MMR-proficient counterparts.[15,16] This result is in stark contrast to most DNA-targeting therapeutics, such as the aforementioned cisplatin and doxorubicin, which are selective towards MMR-*proficient* cell lines over MMR-deficient cell lines, leading to the development of resistance in MMR-deficient tumors following treatment.[17,18]

Several generations of metalloinsertors have been synthesized since $[Rh(bpy)_2(chrysi)]^{3+}$, which has led to the recent discovery of a potent and selective

family of rhodium metalloinsertors containing a pyridyl-alcohol ligand and unique Rh−O ligand coordination (**Figure 2.1**).[19] This Rh−O ligand coordination is structurally distinct from earlier generations of parent metalloinsertors, which contained solely Rh−N coordination.[20] Furthermore, these **Rh−O** metalloinsertors were found to have improved potency and selectivity towards MMR-deficient cancer cells over MMR-proficient cancer cells. Surprisingly, this high potency and cell selectivity was seen across a variety of metalloinsertors containing O-coordinated ligands that differed significantly in size and structure (spanning methyl, pyridyl, phenyl, and hexyl functionalization), suggesting the biological activities of **Rh−O** metalloinsertors are not perturbed by ligand substitution off of the O-containing site.

Here, a family of rhodium metalloinsertors was designed and synthesized as variations of the **Rh−O** metalloinsertor $[Rh(phen)(chrysi)(PPO)]^{2+}$ (phen = 1,10-phenanthroline). These complexes, of the form $[Rh(L)(chrysi)(PPO)]^{2+}$, all include the O-containing PPO ligand but differ in the identity of their ancillary ligand, L, where L= bpy, HDPA (2,2'-dipyridylamine), 4,7-DMP (4,7-dimethyl-1,10-phenanthroline), 5,6-DMP (5,6-dimethyl-1,10-phenanthroline), and DIP (4,7-diphenyl-1,10-phenanthroline) (**Figure 2.2**). The ancillary ligand substitution alters the steric bulk and lipophilicity of these complexes, which can ultimately affect DNA-binding properties and biological activity.[20,21] Each complex described, even the most lipophilic and sterically bulky, shows biological selectivity towards MMR-deficient cell lines, further demonstrating that the Rh−O ligand framework is amenable to a wide array of functionalization. To better understand the trends in biological activity of these complexes, each metalloinsertor was examined for binding affinity to mismatched DNA, pK_a, lipophilicity, whole cell uptake,

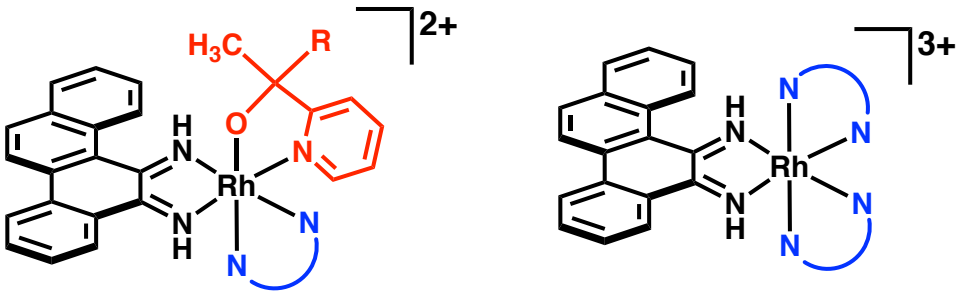

Rh-O
Metalloinsertor

Parent
Metalloinsertor

Figure 2.1 General structure of metalloinsertors. (Left) **Rh−O** metalloinsertors show improved potency and selectivity over parent metalloinsertors that have exclusively Rh-N coordination (right). R has been varied between methyl, phenyl, pyridyl, and hexyl groups and N—N has been varied between several bpy, phen, and HDPA derivatives.

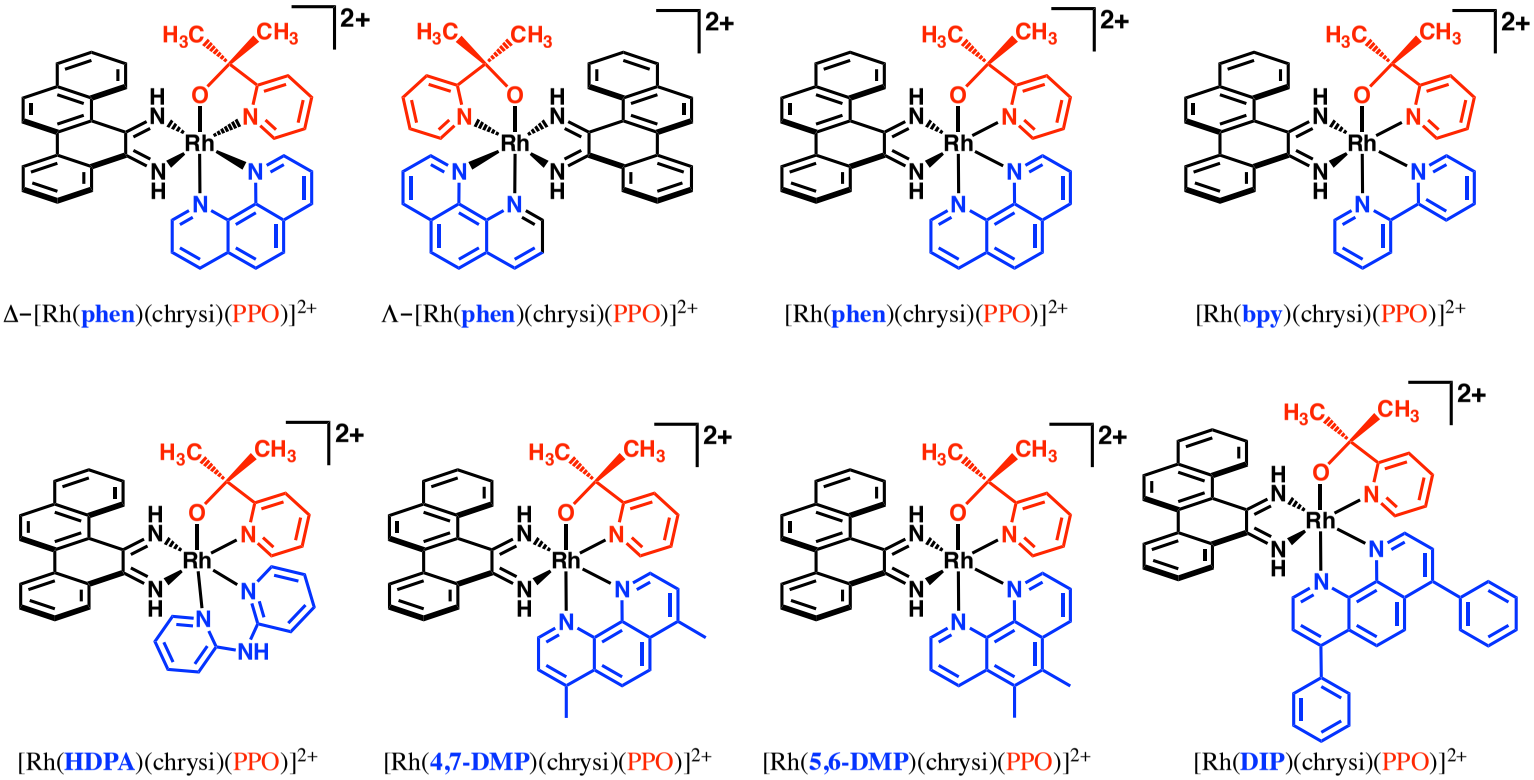

Figure 2.2 Chemical structures of $[Rh(L)(chrysi)(PPO)]^{2+}$ family of rhodium metalloinsertors The PPO ligand is shown in red and the changing ancillary ligand shown in blue.

and subcellular localization into the nucleus and mitochondria. The results indicate that minimizing uptake of the complexes into the mitochondria may be a key factor in ensuring high biological selectivity and support that these **Rh−O** complexes exhibit distinct differences in metalloinsertor-DNA binding and cell activation compared to parent metalloinsertors.

2.2 Experimental Methods

2.2.1 Materials

Commercially available chemicals were used as received. All reagents and Sephadex ion-exchange resin were obtained from Sigma-Aldrich with the following exceptions. $RhCl_3$ was purchased from Pressure Chemical, Inc. Dowex ion-exchange beads were purchased from Acros Organics. Analytical standards for Rb and transition metals were purchased from Analytical West and Ultra Scientific, respectively. MTT and ELISA assay kits were obtained from Roche. Pierce BCA assay kit and NP40 were purchased from Thermo Scientific. Sep-pak C18 solid-phase extraction (SPE) cartridges were purchased from Waters Chemical Co. Cell culture media and supplements were purchased from Invitrogen. Tissue culture flasks and plates were obtained from Corning. ^{32}P labeled ATP was purchased from Perkin Elmer. UreaGel supplies were purchased from National Diagnostics. Microbiospin columns were purchased from BioRad.

2.2.2 Synthesis and Characterization of Metal Complexes

$[Rh(phen)(chrysi)(PPO)]Cl_2$ and $[Rh(bpy)_2(chrysi)]Cl_3$ were synthesized following the published protocols.[19,22] New metal complexes were synthesized in a similar manner to published procedures.[19,20,23] Complete synthetic details for each complex, including specific amounts (masses, volumes, and ratios), are given below.

2.2.2.1 Synthesis and Characterization of $[Rh(bpy)(chrysi)(PPO)]^{2+}$

$RhCl_3 \bullet 3H_2O$ (270 mg, 1.0 mmol, 1 equiv.) and KCl (78 mg, 1.0 mmol, 1 equiv.) were refluxed in methanol (8 mL) for 2 hours at 98 °C. 2,2'-bipyridine (bpy, 160 mg, 1.0 mmol, 1 equiv) was added in a minimum volume of methanol and refluxed for 4 h, during which the deep red solution turned to golden precipitate. The solution was filtered over a medium fritted filter and rinsed with methanol and dried under vacuum (380 mg, 84% crude yield).

$[Rh(bpy)Cl_4]K$ (380 mg, 0.86 mmol, 1 equiv.) was added to an oven-dried 25 mL Schlenk flask with stir bar and degassed by cycling argon and vacuum into the flask. Neat triflic acid (10 g, excess) was added to the flask under positive Ar pressure and immediately capped with a rubber septum and vent needle. The solution turned deep red upon triflic acid addition. After two hours, the argon flow was turned off, the vent needle was removed, and the flask was stirred for 12 h. The solution was then added dropwise to 300 mL cold, stirring ether at -78 °C to produce a yellow-brown precipitate. The precipitate was filtered over a medium frit. To prevent the fine precipitate from flowing through the frit, vacuum was applied slowly during the filtration. One all filtrate was collected, it was washed with cold ether, and dried under vacuum. $[Rh(bpy)(OTf)_4]K$ was combined with NH_4OH (28% w/v, 40 mL, excess) and stirred at 40 °C for 1 h, during which the solution became a foggy light yellow. The solvent was removed under vacuum (280 mg, 42% crude yield).

$[Rh(bpy)(NH_3)_4](OTf)_3$ (280 mg, 0.36 mmol, 1 equiv.) was combined with 5,6-chrysene-quinone (100 mg, 0.39 mmol, 1 equiv.) and 9:1 MeCN:H_2O (40 mL) and NaOH (1 M, 2 mL) and stirred for 1 h. The solution changed from the bright orange of the free

ligand to a red-brown solution with no precipitate. The reaction was quenched with HCl (1 M, 2 mL), producing an even deeper red solution, and the solvent was removed under vacuum. The red product was purified over a C18 SepPak that had been pre-equilibrated with 0.1%TFA (aq) and eluted with 25% MeCN, 75% of 0.1% TFA (aq). (100 mg, 33% yield).

$[Rh(bpy)(chrysi)(NH_3)_2](TFA)_3$ (100 mg, 0.12 mmol, 1 equiv.) was combined with PPO (23 mg, 0.17 mmol, 1.4 equiv.) in 1:1 EtOH:H_2O (10 mL) and refluxed 12 h. The reaction was monitored by LC-MS (liquid chromatography – mass spectrometry) to determine when the reaction was near-complete to improve yield and prevent over-reacting and producing the bis-chrysi complex. The solvent was removed under vacuum and the product was purified by HPLC (85:15 MeCN:0.1% TFA (aq) to 95:5 MeCN:0.1% TFA (aq) over 30 min). The purified product was converted to the chloride salt using Sephadex QAE resin charged with $MgCl_2$. (24 mg, 30% purified yield).

The mass spectrometry, UV-Visible, and NMR characterization of $[Rh(bpy)(chrysi)(PPO)]^{2+}$ is as follows. The TFA salt of $[Rh(bpy)(chrysi)(PPO)]^{2+}$ is soluble in acetonitrile and minimally soluble in water, whereas the chloride salt of $[Rh(bpy)(chrysi)(PPO)]^{2+}$ is soluble in water and minimally soluble in acetonitrile. As such, MS and NMR experiments were performed using the TFA counteranion and UV-Vis experiments were performed using the chloride counteranion. LCQ-MS (cation): *m/z* calc. 650.1 ($M-1H^+$), 325.6 (M^{2+}); obs. 650.0, 325.8. UV-Vis (H_2O): 259nm (59,800 M^{-1} cm^{-1}), 287nm (43,100 M^{-1} cm^{-1}), 298nm (37,100 M^{-1} cm^{-1}), 312nm (32,000 M^{-1} cm^{-1}), 435nm (10,000 M^{-1} cm^{-1}). ^1H NMR (500 MHz, Acetonitrile-d_3) δ 13.44 (br s, 1.2H), 11.89 (br s, 2H), 9.45 (d, J = 5.6 Hz, 1H), 9.36 (d, J = 5.7 Hz, 0.6H), 8.80 (d, J = 8.0, 1.4

Hz, 1H), 8.71 (d, *J* = 5.3 Hz, 0.6H), 8.62 (d, *J* = 8.2 Hz, 0.6H), 8.60-8.54 (m, 2.6H), 8.43-8.26 (m, 8H), 8.26-8.21 (m, 1H), 8.14 (d, *J* = 8.2, 1.5 Hz, 0.6H), 8.06-7.89 (m, 4.8H), 7.85-7.78 (m, 1,6H), 7.77-7.68 (m, 3.2H), 7.68-7.61 (m, 2.2H), 7.60-7.52 (m, 2.6H), 7.31 (d, 0.6H), 7.29-7.21 (m, 2.6H), 1.91 (s, 3H), 1.87 (s, 1.8H), 1.58 (s, 4.8H), purified as a 1:0.6 mixture of diastereomers.

2.2.2.2 Synthesis and Characterization of $[Rh(HDPA)(chrysi)(PPO)]^{2+}$

$RhCl_3 \bullet 3H_2O$ (1.0 g, 3.8 mmol, 1 equiv.) was refluxed in concentrated HCl (38% w/v, 30 mL) for 3 h at 98 °C. 2,2'-dipyridylamine (HDPA, 1.3 g, 7.6 mmol, 2 equiv) was added in a minimum volume of HCl, followed immediately by boiling water (200 mL). The solution was refluxed for 12 h, then cooled to 4 °C. The golden precipitate was filtered over a Buchner funnel and dried under vacuum. (2.2 g, >100% crude yield).

$[Rh(HDPA)Cl_4][H_3O]$ (2.2 g, 1 equiv.) was added to an oven-dried 25 mL Schlenk flask with stir bar and degassed by cycling argon and vacuum into the flask. Neat triflic acid (10 g, excess) was added to the flask under positive Ar pressure and immediately capped with a rubber septum and vent needle. The solution turned deep red upon triflic acid addition. After two hours, the argon flow was turned off, the vent needle was removed, and the flask was stirred for 12 h. The solution was then added dropwise to 200 mL cold, stirring ether at -78 °C to produce a yellow-brown precipitate. The precipitate was filtered over a medium fritted filter. To prevent the fine precipitate from flowing through the frit, vacuum was applied slowly during the filtration. Filtrate was collected, washed with cold ether, and dried under vacuum.

$[Rh(HDPA)(OTf)_4][H_3O]$ was combined with NH_4OH (28% w/v, 100 mL, excess) and stirred at 40 °C for 45 min, during which the solution became a foggy light

yellow. The solvent was removed under vacuum and the product was dissolved in a minimal amount of water and precipitated with 10:1 ether:EtOH, filtered over a medium fritted filter, and dried further under vacuum. (400 mg, 10% crude yield).

$[Rh(HDPA)(NH_3)_4](OTf)_3$ (400 mg, 0.51 mmol, 1 equiv.) was combined with 5,6-chrysene-quinone (140mg, 0.55 mmol, 1 equiv.) and MeCN (65 mL) and NaOH (1 M, 8 mL) and stirred for 12 h. The solution changed from the bright orange of the free ligand to a red-brown solution with no precipitate. The reaction was quenched with HCl (1 M, 8 mL), producing an even deeper red solution, and the solvent was removed under vacuum. The red product was purified over a C18 SepPak, pre-equilibrated with 0.1%TFA (aq) and eluted with 25% MeCN, 75% of 0.1% TFA (aq). (220 mg, 51% yield).

$[Rh(HDPA)(chrysi)(NH_3)_2](TFA)_3$ (70 mg, 0.08 mmol, 1 equiv.) was combined with PPO (24 mg, 0.17 mmol, 2.1 equiv.) in 1:1 EtOH:H_2O (20 mL) and refluxed 7 d. The reaction was monitored by LC-MS to determine when the reaction was near-complete to improve yield and prevent over-reacting and producing the bis-chrysi complex. The solvent was removed under vacuum and the product was purified by HPLC (85:15 MeCN:0.1% TFA (aq) to 95:5 MeCN:0.1% TFA (aq) over 30 min). The purified product was converted to the chloride salt using Sephadex QAE resin charged with $MgCl_2$. (6 mg, 10% purified yield).

The MS, UV-Visible, and NMR characterization of $[Rh(HDPA)(chrysi)(PPO)]^{2+}$ is as follows. As described above, MS and NMR experiments were performed using the TFA counteranion and UV-Vis experiments were performed using the chloride counteranion for solubility reasons. LCQ-MS (cation): *m/z* calc. 665.2 ($M\text{-}1H^+$), 333.1

(M^{2+}); obs. 665.3, 333.3. UV-Vis (H_2O): 259nm (60,400 M^{-1} cm^{-1}), 283nm (45,900 M^{-1} cm^{-1}), 326nm (18,600 M^{-1} cm^{-1}), 440nm (8,500 M^{-1} cm^{-1}). ^1H NMR (500 MHz, Acetonitrile-d_3) δ 12.49 (br s, 1H), 12.04 (br s, 1H), 8.72 (dd, J = 8.0, 1.3 Hz, 1H), 8.50 (d, J = 6.0 Hz, 1H), 8.38-8.31 (m, 3H), 8.31-8.23 (m, 2H), 8.20-8.13 (m, 2H), 8.08-8.00 (m, 2H), 7.98 (td, J = 8.6, 1.6 Hz, 1H), 7.94-7.81 (m, 4H), 7.69 (m, 3H), 7.51 (ddd, J = 7.6, 6.0, 1.4 Hz, 1H), 7.23 (ddd, J = 7.4, 6.1, 1.3 Hz, 1H), 7.17 (ddd, J = 7.4, 6.2, 1.4 Hz, 1H), 1.78 (s, 3H), 1.56 (s, 3H), purified as a single diastereomer.

2.2.2.3 Synthesis and Characterization of [Rh(4,7-DMP)(chrysi)(PPO)]$^{2+}$

$RhCl_3$•$3H_2O$ (500 mg, 1.9 mmol, 1 equiv.) and KCl (150 mg, 2.0 mmol, 1 equiv.) were refluxed in methanol (10 mL) for 2 h at 98 °C. 4,7-dimethyl-1,10-phenanthroline (4,7-DMP, 400 mg, 1.9 mmol, 1 equiv) was added in a minimum volume of methanol and refluxed for 4 h, during which the deep red solution turned to golden precipitate. The solution was filtered over a medium fritted filter and rinsed with methanol and dried under vacuum (800 mg, 86% crude yield).

[Rh(4,7-DMP)Cl_4]K (800 mg, 1.6 mmol, 1 equiv.) was added to an oven-dried 25 mL Schlenk flask with stir bar and degassed by cycling argon and vacuum into the flask. Neat triflic acid (10 g, excess) was added to the flask under positive Ar pressure and immediately capped with a rubber septum and vent needle. The solution turned deep red upon triflic acid addition. After two hours, the argon flow was turned off, the vent needle was removed, and the flask was stirred for 12 h. The solution was then added dropwise to 250 mL cold, stirring ether at -78 °C to produce a yellow-brown precipitate. The precipitate was filtered over a medium frit. To prevent the fine precipitate from flowing

through the frit, vacuum was applied slowly during the filtration. One all filtrate was collected, it was washed with cold ether, and dried under vacuum. The product, [Rh(4,7-DMP)$(OTf)_4$]K was combined with NH_4OH (28% w/v, 50 mL, excess) and stirred at 40 °C for 1 h, during which the solution became a foggy brown. The solvent was removed under vacuum and the product was suspended in EtOH (5 mL), filtered over a medium fritted filter and rinsed with cold ethanol, and dried further under vacuum. (200 mg, 15% crude yield).

[Rh(4,7-DMP)$(NH_3)_4$]$(OTf)_3$ (200 mg, 0.24 mmol, 1 equiv.) was combined with 5,6-chrysene-quinone (70mg, 0.39 mmol, 1.6 equiv.) and 6:1 MeCN:H_2O (35 mL) and NaOH (1 M, 5 mL) and stirred for 1 h. The solution changed from the bright orange of the free ligand to a green-brown solution with no precipitate. The reaction was quenched with HCl (1 M, 5 mL), producing a deep red solution, and the solvent was removed under vacuum. The red product was HPLC purified (85:15 MeCN:0.1% TFA (aq) to 95:5 MeCN:0.1% TFA (aq) over 30 min). (100 mg, 46% purified yield).

[Rh(4,7-DMP)(chrysi)$(NH_3)_2$]$(TFA)_3$ (50 mg, 0.03 mmol, 1 equiv.) was combined with PPO (9 mg, 0.07 mmol, 2 equiv.) in 1:1 EtOH:H_2O (10 mL) and refluxed 12 h. The reaction was monitored by LC-MS to determine when the reaction was near-complete to improve yield and prevent over-reacting and producing the bis-chrysi complex. The solvent was removed under vacuum and the product was purified by HPLC (85:15 MeCN:0.1% TFA (aq) to 95:5 MeCN:0.1% TFA (aq) over 30 min). The purified product was converted to the chloride salt using Sephadex QAE resin charged with $MgCl_2$. (4 mg, 10% purified yield).

The MS, UV-Visible, and NMR characterization of [Rh(4,7-DMP)(chrysi)(PPO)]$^{2+}$ is as follows. As described above, MS and NMR experiments were performed using the TFA counteranion and UV-Vis experiments were performed using the chloride counteranion for solubility reasons. LCQ-MS (cation): *m/z* calc. 702.2 (M-1H^{+}), 351.6 (M^{2+}); obs. 702,3, 351.8. UV-Vis (H_2O): 269nm (106,800 M^{-1} cm^{-1}), 440nm (11,400 M^{-1} cm^{-1}). ^{1}H NMR (500 MHz, Acetonitrile-d_3) δ 13.31 (br s, 0.8H), 11.75 (br s, 2H), 9.50 (d, *J* = 5.4 Hz, 1H), 9.42 (d, *J* = 5.4 Hz, 0.4H), 8.86 (dd, *J* = 5.5, 0.9 Hz, 1H), 8.83 (dd, *J* = 8.0, 1.3 Hz, 1H), 8.73 (d, *J* = 5.4 Hz, 0.4H), 8.47 (d, *J* = 2.5 Hz, 0.4H), 8.46-8.35 (m, 4.2H), 8.34 (d, *J* = 8.2 Hz, 0.4H), 8.27 (d, *J* = 8.8 Hz, 1H), 8.21-8.17 (m, 1.4H), 8.16 (d, *J* = 8.1 Hz, 0.4H), 8.08 (dd, *J* = 5.4, 1.0 Hz, 1H), 8.04 (d, *J* = 5.4 Hz, 0.4H), 8.00 (dd, *J* = 7.5, 1.7 Hz, 1H), 7.97-7.92 (m, 2.4H), 7.84 (m, 1.8H), 7.77 (m, 1.4H), 7.61-7.51 (m, 5.2H), 7.19-7.15 (m, 0.4H), 7.10-7.03 (m, 2.8H), 3.05 (s, 3H), 3.04 (s, 1.2H), 3.02 (s, 1.2H), 2.99 (s, 3H), 1.95 (s, 3H), 1.92 (s, 1.2H), 1.62 (s, 3H), 1.61 (s, 1.2H), purified as a 1:0.4 mixture of diastereomers.

2.2.2.4 Synthesis and Characterization of [Rh(5,6-DMP)(chrysi)(PPO)]$^{2+}$

$RhCl_3$•$3H_2O$ (1.0 g, 3.8 mmol, 1 equiv.) and KCl (290 mg, 3.9 mmol, 1 equiv.) were refluxed in methanol (15 mL) for 2 h at 98 °C. 5,6-dimethyl-1,10-phenanthroline (5,6-DMP, 790 mg, 3.8 mmol, 1 equiv) was added in a minimum volume of methanol and refluxed for 4 h, during which the deep red solution turned to beige precipitate. The solution was filtered over a medium frit and rinsed with methanol and dried under vacuum (1.7 g, 91% crude yield).

[Rh(5,6-DMP)Cl_4]K (1.7 g, 3.4 mmol, 1 equiv.) was added to an oven-dried 25 mL Schlenk flask with stir bar and degassed by cycling argon and vacuum into the flask. Neat triflic acid (10 g, excess) was added to the flask under positive Ar pressure and immediately capped with a rubber septum and vent needle. The solution turned deep red upon triflic acid addition. After two hours, the argon flow was turned off, the vent needle was removed, and the flask was stirred for 12 h. The solution was then added dropwise to 200 mL cold, stirring ether at -78 °C to produce a yellow-brown precipitate. The precipitate was filtered over a medium frit. To prevent the fine precipitate from flowing through the frit, vacuum was applied slowly during the filtration. One all filtrate was collected, it was washed with cold ether, and dried under vacuum. The product, [Rh(5,6-DMP)$(OTf)_4$]K was combined with NH_4OH (28% w/v, 100 mL, excess) and stirred at 40 °C for 40 min. The solvent was removed under vacuum and the product was dissolved in minimal EtOH and precipitated in ether, filtered over a medium fritted filter, and dried further under vacuum. (2.2 g, 77% crude yield).

[Rh(5,6-DMP)$(NH_3)_4$]$(OTf)_3$ (830 mg, 1.0 mmol, 1 equiv.) was combined with 5,6-chrysene-quinone (250 mg, 1.0 mmol, 1 equiv.) and 11:1 MeCN:H_2O (250 mL) and NaOH (1M, 4 mL) and stirred for 1 h. The solution changed from the bright orange of the free ligand to a green-brown solution with no precipitate. The reaction was quenched with HCl (1 M, 4 mL), producing a deep red solution, and the solvent was removed under vacuum. The red product was HPLC purified (85:15 MeCN:0.1% TFA (aq) to 95:5 MeCN:0.1% TFA (aq) over 30 min). (540 mg, 62% purified yield).

[Rh(5,6-DMP)(chrysi)$(NH_3)_2$]$(TFA)_3$ (40mg, 0.04 mmol, 1 equiv.) was combined with PPO (11 mg, 0.08 mmol, 2 equiv.) in 1:1 EtOH:H_2O (10 mL) and

refluxed 12 h. The reaction was monitored by LC-MS to determine when the reaction was near-complete to improve yield and prevent over-reacting and producing the bis-chrysi complex. The solvent was removed under vacuum and the product was purified by HPLC (85:15 MeCN:0.1% TFA (aq) to 95:5 MeCN:0.1% TFA (aq) over 30 min). The use of Sephadex QAE in the ion exchange of $[Rh(5,6\text{-DPE})(chrysi)(PPO)]^{2+}$ was insufficient; therefore the purified product was converted to the chloride salt using Dowex 1x2 500-100 mesh ion exchange resin. (8 mg, 23% purified yield).

The MS, UV-Visible, and NMR characterization of $[Rh(5,6\text{-DMP})(chrysi)(PPO)]^{2+}$ is as follows. As described above, MS and NMR experiments were performed using the TFA counteranion and UV-Vis experiments were performed using the chloride counteranion for solubility reasons. LCQ-MS (cation): *m/z* calc. 702.2 ($M\text{-}1H^{+}$), 351.6 (M^{2+}); obs. 702.3, 351.8. UV-Vis (H_2O): 267nm (80,600 M^{-1} cm^{-1}), 280nm (81,700 M^{-1} cm^{-1}), 438nm (10,500 M^{-1} cm^{-1}). ^1H NMR (500 MHz, Acetonitrile-d_3) δ 13.40 (br s, 0.3H), 11.77 (br s, 1H), 9.68 (d, J = 5.2 Hz, 1H), 9.59 (d, J = 5.1 Hz, 0.3H), 9.06-8.97 (m, 3.9H), 8.84-8.89 (m, 1.3H), 8.43-8.37 (m, 2.6H), 8.34 (d, J = 8.2 Hz, 0.3H), 8.29-8.14 (m, 5.2H), 8.02-7.97 (m, 2.3H), 7.96-7.89 (m, 2.6H), 7.83-7.73 (m, 1.6H), 7.57 (td, J = 7.4, 1.4 Hz, 2H), 7.55-7.50 (m, 1H), 7.17 (d, J = 5.7 Hz, 0.3H), 7.10-7.02 (m, 2.3H), 2.91 (s, 0.9H), 2.90 (s, 0.9H), 2.89 (s, 3H), 2.87 (s, 3H), 1.93 (s, 3H), 1.90 (s, 0.9H), 1.58 (s, 3.9H), purified as a 1:0.3 mixture of diastereomers.

2.2.2.5 Synthesis and Characterization of $[Rh(DIP)(chrysi)(PPO)]^{2+}$

$RhCl_3 \bullet 3H_2O$ (770 mg, 2.9 mmol, 1 equiv.) and KCl (230 mg, 3.1 mmol, 1 equiv.) were refluxed in methanol (15 mL) for 2 hours at 98 °C. 4,7-diphenyl-1,10-phenanthroline (DIP, 970 mg, 2.9 mmol, 1 equiv) was added in a minimum volume of

methanol and refluxed for 4 h, during which the deep red solution turned to beige-yellow precipitate. The solution was filtered over a medium frit and rinsed with methanol and dried under vacuum (1.7 g, 95% crude yield).

[Rh(DIP)Cl_4]K (1.7 g, 2.8 mmol, 1 equiv.) was added to an oven-dried 25 mL Schlenk flask with stir bar and degassed by cycling argon and vacuum into the flask. Neat triflic acid (10 g, excess) was added to the flask under positive Ar pressure and immediately capped with a rubber septum and vent needle. The solution turned deep red upon triflic acid addition. After two hours, the argon flow was turned off, the vent needle was removed, and the flask was stirred for 12 h. The solution was then added dropwise to 200 mL cold, stirring ether at -78 °C to produce a yellow-brown precipitate. The precipitate was filtered over a medium frit. To prevent the fine precipitate from flowing through the frit, vacuum was applied slowly during the filtration. One all filtrate was collected, it was washed with cold ether, and dried under vacuum. The product, [Rh(DIP)$(OTf)_4$]K was combined with NH_4OH (28% w/v, 100 mL, excess) and stirred at 40 °C for 40 min. The solvent was removed under vacuum and the product was dissolved in minimal EtOH and precipitated in ether, filtered over a medium fritted filter, and dried further under vacuum. (1.9 g, 72% crude yield).

[Rh(DIP)$(NH_3)_4$]$(OTf)_3$ (510 mg, 0.54 mmol, 1 equiv.) was combined with 5,6-chrysene-quinone (140 mg, 0.55 mmol, 1 equiv.) and 11:1 MeCN:H_2O (250 mL) and NaOH (1 M, 4 mL) and stirred for 1 h. The solution changed from the bright orange of the free ligand to a green-brown solution with no precipitate. The reaction was quenched with HCl (1 M, 4 mL), producing a deep red solution, and the solvent was removed under vacuum. The red product was purified over a C18 SepPak, pre-equilibrated with

0.1%TFA (aq), and eluted with 25% MeCN, 75% of 0.1% TFA (aq). (620 mg, >100% crude yield).

[Rh(DIP)(chrysi)(NH_3)$_2$](TFA)$_3$ (52 mg, 0.05 mmol, 1 equiv.) was combined with PPO (15 mg, 0.11 mmol, 2 equiv.) in 9:1 EtOH:H_2O (10 mL) and refluxed 12 h. The solvent was removed under vacuum and the product was purified by HPLC (85:15 MeCN:0.1% TFA (aq) to 95:5 MeCN:0.1% TFA (aq) over 30 min). The use of Sephadex QAE in the ion exchange of $[Rh(DIP)(chrysi)(PPO)]^{2+}$ was insufficient, and therefore the purified product was converted to the chloride salt using Dowex 1x2 500-100 mesh ion exchange resin. (15 mg, 33% yield).

The MS, UV-Visible, and NMR characterization of $[Rh(DIP)(chrysi)(PPO)]^{2+}$ is as follows. As described above, MS and NMR experiments were performed using the TFA counteranion and UV-Vis experiments were performed using the chloride counteranion for solubility reasons. LCQ-MS (cation): m/z calc. 826.2 (M-1H+); obs. 826.3. UV-Vis (H_2O): 267nm (103,000 M^{-1} cm^{-1}). ^{1}H NMR (500 MHz, Methanol-d_4) δ 9.74 (dd, J = 5.5, 0.9 Hz, 1H), 9.70 (dd, J = 5.5, 0.8 Hz, 0.5H), 8.89 (m, 1.5H), 8.76 (m, 1.5H), 8.58-8.46 (m, 4.5H), 8.40-8.28 (m, 6H), 8.14-7.98 (m, 4.5H), 7.81-7.59 (m, 15H), 7.56-7.49 (m, 1.5H), 7.41-7.33 (m, 6H), 7.34-7.23 (m, 3H), 2.07 (s, 3H), 2.02 (s, 1.5H), 1.70 (s, 1.5H), 1.69 (s, 3H), purified as a 1:0.5 mixture of diastereomers.

2.2.3 Enantiomeric Separation of [Rh(phen)(chrysi)(PPO)]Cl_2

Purified [Rh(phen)(chrysi)(PPO)][TFA]$_2$ was dissolved in 1:1 ethanol:water and HPLC purified on an Astec CYCLOBOND chiral column using an isocratic elution method of 40:60 ACN:0.1 M KPF_6 (aq) over 37 min and monitoring the 440 nm absorbance. The column was periodically rinsed with 40:60 MeCN:H_2O to remove KPF_6

buildup. The number of peaks observed during this separation varied by batch, with up to eight peaks being observed. During the preliminary runs, each peak was collected and examined by MS (or LC-MS) to determine if it was a desired product or a side product. Peaks identified as the desired product were collected and the remaining peaks discarded. Injection volume for each run was determined such that a significant dip in absorbance (>50% of the max peak intensity) was observed between the desired peaks. Separated enantiomers were collected and exchanged to the chloride salt using Sephadex QAE resin pre-equilibrated with $MgCl_2$. The enantiomeric nature of the collected fractions was verified using circular dichroism (CD) as follows: 200 μM solutions of Δ- and Λ-[Rh(phen)(chrysi)(PPO)]Cl_2 were made in aqueous solution and their CD spectra recorded in 1 nm increments on an Aviv 62DS spectropolarimeter under a N_2 atmosphere at ambient temperature. The spectra were recorded a second time 30 d later to assess decomposition or racemization of the sample, and none was observed.

2.2.4 Determination of Extinction Coefficients

Aqueous solutions of each [Rh(L)(chrysi)(PPO)]Cl_2 complex were made and a UV-Visible spectrum was recorded for each. The solutions were diluted 50x, 100x, 500x, and 1000x in 2% HNO_3. These dilutions were made based on mass and the precise dilution of each complex was determined using these masses. The dilutions were analyzed for Rh content *via* ICP-MS (inductively coupled plasma mass spectrometry) and the concentration was determined by comparison to a standard curve ranging from 1-100 ppb. Extinction coefficients were determined from the UV-Visible absorbance measurement of the initial solution and the Rh concentration of the dilutions following Beer's law ($A=\varepsilon lc$). L = DIP was observed to significantly adsorb onto plastics; therefore

PTFE (polytetrafluoroethylene) and PFA (perfluoroalkoxy alkane) coated materials (falcon tubes that held the samples, pipette tips used in the dilution step, and the tubing used on the ICP-MS instrument) were used in the workup and analysis of its extinction coefficient.

2.2.5 Partition Coefficient Determination

One-octanol and 10 mM Tris-HCl, pH 7.4 were pre-equilibrated with each other by vigorously shaking the phases together. A solution of each metalloinsertor was made in octanol and the UV-Visible spectrum of the solution recorded. Each solution was combined with an equal volume of aqueous buffer and shaken using a foam insert on a Vortex-Genie 2 running at maximum speed for 16 h. The samples were centrifuged to separate the aqueous and octanol phases and a UV-Visible spectrum of each octanol fraction was recorded. The baseline value obtained at 800 nm was used to normalize the spectra to a common zero point. Provided equal volumes of octanol and water are mixed upon equilibration, absorbance of the ~260 nm peak in the final spectrum can be compared to the initial spectrum to determine the partition coefficient following the literature.[24]

$$Log\ P = Log\left(\frac{Abs_{final}}{Abs_{initial} - Abs_{final}}\right)$$

The partition coefficients from three experiments were measured for each [Rh(L)(chrysi)(PPO)]Cl_2 complex and averaged to determine the partition coefficient.

2.2.6 pK_a Determination of Metalloinsertors

A ~25 μM solution of each metalloinsertor was made in 100 mM NaCl. The pH of the sample was adjusted to 4.5 using HCl (10 mM). NaOH (10 mM) was titrated into the solution, with stirring. The pH and UV-Visible spectrum were recorded after each

addition, up to a pH of 10.5. A back titration to pH 6 was performed to check for decomposition, and none was observed. Since the moles of metalloinsertor do not change throughout this experiment, spectra were corrected for baseline and volume changes using the dilution equation ($M_1V_1 = M_2V_2$). The absorbance of the ~430 nm peak was plotted against pH and fit to a sigmoidal curve in OriginPro v8.5, and the pK_a was determined as the inflection point of the curve. Three pK_a titrations were performed for each $[Rh(L)(chrysi)(PPO)]Cl_2$ complex and averaged to give an average pK_a value.

2.2.7 Binding Constant Experiments

2.2.7.1 Purifying and Radiolabeling DNA

A DNA hairpin (5'-GGCAGG**X**ATGGCTTTTTGCCAT**Y**CCTGCC-3', where **XY**=CG or CC for a well-matched or mismatched hairpin, respectively) was radiolabeled with γ-^{32}P ATP and prepared following the literature.[10,19,22] DNA was purchased from IDT DNA and purified by HPLC on a C18 reverse-phase column. The DNA was quantified using extinction coefficients provided by IDT DNA. The hairpin was incubated with γ-^{32}P ATP and polynucleotide kinase at 37 ℃ for 2.5 h, and then purified using two BioRad Micro Bio-Spin 6 columns following the manufacturer's instructions. Solvent was removed from the DNA, and the DNA was dissolved in 10 mM NaP_i, pH 7.1. A 2 μM solution of DNA was made in 100 mM NaCl and 20 mM NaP_i buffer containing approximately 1% ^{32}P-labeled DNA and 99% unlabeled DNA. To anneal, the DNA was heated on a 90℃ heat block for 10 min, cooled to room temperature over the course of 2.5 h, and then stored at 4 °C prior to use. The hairpin structure does not anneal as readily as the sequence used in reference 22, therefore storage at 4 °C for several hours is essential for properly annealed DNA; cooling to room temperature alone will result in

minimal photocleavage by the photocleaving metalloinsertor. The same purification strategy was employed for the complementary DNA sequences 5'-GACTTATCTAG-**GA**TGATAAGCTCGTC-3' and 5'-GACCAGCTTAT**CAT**ACCTAGATAAGTC-3' which pair to give a 27-mer DNA duplex with a central single base bulge (relavant bases bolded). The later sequence (containing the bulge) was radiolabeled and annealed following the above method.

2.2.7.2 Metalloinsertors Titrations to Determine Binding Affinity

Full details of DNA preparation and purification can be found in the SI. A 4 μM solution of the photocleaving metalloinsertor $[Rh(bpy)_2(chrysi)]Cl_3$ and solutions containing 0-400 μM of a competing metalloinsertor, $[Rh(L)(chrysi)(PPO)]Cl_2$ (which does not photocleave DNA), were made in MilliQ water. Five μL of the $[Rh(bpy)_2(chrysi)]Cl_3$ solution, 5 μL of the competing metalloinsertor, and 10 μL of the hairpin DNA were combined to create a solution containing 1 μM $[Rh(bpy)_2(chrysi)]Cl_3$, 0-100 μM competing metalloinsertor, and 1 μM DNA. Similarly, an experiment was carried out using the single base bulge DNA sequence, $[Rh(bpy)_2(chrysi)]Cl_3$, and the competing metalloinsertor $[Rh(phen)(chrysi)(PPO)]Cl_2$ in the same concentrations described above. The samples were irradiated with an Oriel 1000 W Hg/Xe solar simulator (340-440 nm) for 20 min. After irradiation, solvent was removed from the samples and the samples were counted on a scintillation counter to determine the necessary exposure time (with 300,000 cpm needing a 1 h exposure, 100,000 cpm needing a 3 h exposure, and other exposure times determined from these two points) and they were suspended in a denaturing formamide loading dye. Samples were

electrophoresed on a 20% denaturing polyacrylamide urea gel that was pre-warmed and wells pre-checked for integrity using empty loading dye.

A phosphor screen was exposed to the polyacrylamide gel and imaged using a Typhoon FLA 9000 biomolecular imager. The ratio of photocleaved to uncleaved DNA was quantified using ImageQuant TL software. The ratio was plotted against the concentration of $[Rh(L)(chrysi)(PPO)]Cl_2$ and fit to a sigmoidal curve in OriginPro v8.5 to determine the inflection point of the fit. The binding affinity of the competing metalloinsertor was calculated in Mathematica 9.0 by solving simultaneous equilibria involving DNA, $[Rh(bpy)_2(chrysi)]Cl_3$, and $[Rh(L)(chrysi)(PPO)]Cl_2$. Three photocleavage titrations were performed for each $[Rh(L)(chrysi)(PPO)]Cl_2$ complex and averaged to give the binding affinity.

2.2.8 Melting Temperature Analysis

Melting temperature analysis was performed on a Beckman DU 7400 spectrophotometer equipped with a Tm Analysis Accessory. The short oligomer, 5'-CGGACTCCG-3' (underline denotes mismatch), was purchased from IDT DNA and purified by HPLC. The use of a short oligo was essential in this experiment as the inclusion of a mismatch dramatically reduces the melting temperature of the oligo. The use of longer oligos is possible, however changes in melting temperature will be less dramatic and observable. Samples containing 11 μM ssDNA (ultimately 5.5 μM dsDNA and mismatches) and 6 μM of $[Rh(phen)(chrysi)(PPO)]Cl_2$, $[Rh(bpy)_2(chrysi)]Cl_3$ or no metal complex were prepared in phosphate buffer (5 mM phosphate, 50 mM NaCl, pH 7.0). Samples were heated at a rate of 0.5 °C/min and absorbance was measured at 260 nm every 0.5 °C between 10 °C and 50 °C. Temperatures higher than 50 °C were not

examined due to challenges with sample evaporation leading to interpretable results. Data from three experiments was combined and fit to a sigmoidal curve in OriginPro v8.5 and the melting temperature was taken as the inflection point of the curve.

2.2.9 Cell Culture

HCT116N and HCT116O cells were grown in RPMI (Roswell Park Memorial Institute) 1640 media supplemented with 10% FBS (fetal bovine serum), 2 mM L-glutamine, 0.1 mM non-essential amino acids, 1 mM sodium pyruvate, 100 units/mL penicillin and streptomycin, and 100 μg/mL Geneticin (G418). The cells were incubated in tissue culture flasks or plates at 37 °C in a 5% CO_2 atmosphere. All cell studies were performed with the chloride salt of each metalloinsertor.

2.2.9.1 Cell Proliferation ELISA

Cell proliferation ELISA (enzyme-linked immunosorbent assay) was performed following the manufacturers instructions. Briefly, 2×10^3 HCT116N or HCT116O cells in 100 μL media were plated into each well of a 96-well plate. The cells were allowed to adhere for 24 h before the addition of 100 μL of media containing various concentrations of rhodium metalloinsertor. The plates were incubated for an additional 48 h before the rhodium-containing media was replaced with fresh media, with which the cells were allowed to grow for the remainder of a 72 h period. Cells were then treated with an excess of the unnatural nucleic acid, BrdU (bromodeoxyuridine), for 24 h during which time it could be incorporated into newly synthesized DNA. Cells were then fixed, labeled with a BrdU antibody, and quantified using a colorimetric substrate solution and stop solution. Absorbance was measured at 450 nm (background subtracted at 690 nm). Decrease in cellular proliferation was determined for each metalloinsertor concentration

through comparison to untreated cells. Outliers were removed using a modified Thompson Tau test. An additional variation of this assay was performed in which the cells were treated with rhodium metalloinsertor for 24 h, then directly treated with BrdU in fresh media.

2.2.9.2 MTT Cytotoxicity Assay

Cell proliferation MTT (MTT = 2-(4,5-dimethylthiazol-2-yl)-2,5-diphenyltatrazolium bromide) assays were performed following the manufacturers instructions. Briefly, 5×10^4 HCT116N or HCT116O cells in 100 μL media were plated into each well of a 96-well plate. Various concentrations of a rhodium metalloinsertor were added to each well. The cells were allowed to incubate for 72 h before treatment with MTT for 4 h, during which time MTT could be converted into formazan by metabolically active cells. The formazan crystals were solubilized and quantified by absorbance at 570 nm (background subtracted at 690 nm). Viability was determined for each metalloinsertor concentration through comparison to untreated cells. Outliers were removed using a modified Thompson Tau test. An additional variation of this assay was performed in which the cells were allowed to adhere to the 96-well plate overnight before treated with rhodium metalloinsertor for 24 h, immediately followed by MTT treatment and workup.

2.2.9.3 Metalloinsertor Stability with BSA

Serum proteins represent potential targets or sequestration agents in metalloinsertor treatment. As such, experiments were performed to determine the extent to which bovine serum albumin (BSA) binding influences metalloinsertor activity in the MTT assay. 10,000 cells plated into each well of a 96-well plate. Cells were immediately

incubated with either 0, 0.25 or 0.60 μM $[Rh(phen)(chrysi)(PPO)]^{2+}$ and either a 10, or 100-fold higher concentration of BSA. Controls of metalloinsertor alone (no BSA) and BSA alone (no metalloinsertor were included for comparison and normalization purposes. After a 72 hour incubation, which is representative of the majority of our cytotoxicity experiments, the cells were treated with MTT reagent and analyzed following section 2.2.9.2. Three replicates of each metalloinsertor/BSA concentration were performed.

2.2.9.4 Uptake and Localization Experiments

Whole-cell uptake, mitochondrial localization, and nuclear localization of metalloinsertors were determined following published methods.[25] Prior to whole-cell, mitochondrial, and nuclear rhodium determination, 24-hour ELISA and MTT assays were performed to determine a metalloinsertor concentration that would not result in significant cell death by MTT but showed some anti-proliferative effect by ELISA. The concentrations used in the uptake and localization studies of the $[Rh(L)(chrysi)(PPO)]Cl_2$ family were 0.2 μM for L=DIP, 0.5 μM for L=phen, bpy, HDPA, 4,7-DMP, and 5,6-DMP, and 10 μM for $[Rh(bpy)_2(chrysi)]Cl_3$, which was included as a control.

2.2.9.5 Assay for Whole-Cell Rhodium Concentration

Whole-cell uptake experiments were performed following published protocols.[20] Briefly, 1×10^6 HCT116N or HCT116O cells were plated into 6-well tissue culture treated plates and allowed to adhere for 24 h. Media was aspirated from the cells and fresh media containing a metalloinsertor was added to each well. Cells were allowed to incubate for an additional 0.5-24 h with the Rh-containing media. After incubation, media was aspirated and the cells were rinsed three times with PBS (phosphate buffered saline, pH

7.4) to remove surface rhodium. Cells were lysed directly in the well using 1 mL of 1% SDS solution. These samples were transferred to microcentrifuge tubes and sonicated for 10 s at 20% amplitude on a Qsonica Ultrasonic sonicator. Cell lysate was combined with an equal volume 2% HNO_3. This solution was analyzed for Rh content on an Agilent 8800 Triple Quadrupole ICP-MS and the concentration of Rh in each sample was determined by comparison to a standard curve (ranging from 1-100 ppb Rh) and normalized using the protein content of each sample. The protein content of each sample was determined using a Pierce BCA assay, following the manufacturer's instructions.

2.2.9.6 Assay for Mitochondrial Rhodium Concentration

Mitochondrial uptake experiments were performed following published protocols.[20,26] Briefly, 1.5×10^7 HCT116N and HCT116O cells were plated in T75 tissue culture treated flasks. The cells were allowed to adhere for 24 h, after which media was aspirated from each flask and restored with 20 mL media containing a rhodium metalloinsertor. The cells were allowed to grow in the presence of Rh-containing media for 24 h, then harvested using 0.05% trypsin over 5 minutes. Cells were pelleted by centrifugation at 1200 rpm for 5 min. The pellet was rinsed and suspended in PBS, then pelleted again and the PBS removed. The cell pellet was suspended in 500 μL mitochondrial extraction buffer (200 mM mannitol, 68 mM sucrose, 50 mM PIPES, 50 mM KCl, 5 mM EGTA, 2 mM $MgCl_2$, 1 mM DTT added just before use, and protease inhibitors added just before use) and incubated on ice for 20 min. Each sample was homogenized by 35 passes thorough a 21-gauge needle and syringe. The resultant solution was centrifuged for 5 min at 750 rpm. The supernatant of each sample was transferred to a 1.5 mL microcentrifuge tube and centrifuged for 10 min at 14,000 g. The

supernatant was decanted and the resulting pellet was the mitochondrial fraction. SDS (800 μL of a 1% solution) was added to the pellet and sonicated for 10 s at 40% amplitude on a Qsonica Ultrasonic sonicator. Mitochondrial lysate was combined with an equal volume of 2% nitric acid. This solution was analyzed for Rh content on an Agilent 8800 Triple Quadrupole ICP-MS and the concentration of Rh in each sample was determined by comparison to a standard curve (ranging from 1-100 ppb Rh) and normalized using the protein content of each sample. The protein content of each sample was determined using a Pierce BCA assay, following the manufacturer's instructions.

2.2.9.7 Assay for Nuclear Rhodium Concentration

Nuclear uptake experiments were performed following published protocols.[20] Briefly, 1×10^7 HCT116N and HCT116O cells were plated in T75 tissue culture treated flasks. The cells were allowed to adhere for 24 h before the media was aspirated and restored with 20 mL media containing a rhodium metalloinsertor. The cells were allowed to grow in the presence of Rh-containing media for 24 h, then harvested using 0.05% trypsin over 5 minutes. Cells were pelleted by centrifugation at 1200 rpm for 5 min. The pellet was rinsed and suspended in PBS, then pelleted and the PBS removed. Each cell pellet was suspended in 1 mL hypotonic buffer (20 mM Tris-HCl pH 7.4, 10 mM NaCl, 3 mM $MgCl_2$), transferred to a microcentrifuge tube, and incubated on ice for 15 min. NP-40 (50 μL of a 10% solution) was added to each sample, vortexed for 10 s at the highest setting, and centrifuged at 3000 g for 10 min. The supernatant was decanted and the resulting pellet was the nuclear fraction. SDS (800 μL of a 1% solution) was added to the pellet and then sonicated for 10 s at 40% amplitude on a Qsonica Ultrasonic sonicator. Nuclear lysate was combined with an equal volume of 2% HNO_3. This solution was

analyzed for Rh content on an Agilent 8800 Triple Quadrupole ICP-MS and the concentration of Rh in each sample was determined by comparison to a standard curve (ranging from 1-100 ppb Rh) and normalized using the protein content of each sample. The protein content of each sample was determined using a Pierce BCA assay, following the manufacturer's instructions.

2.2.9.8 Assay for Uptake Mechanism of Metalloinsertors

Mechanism of uptake experiments were adapted from published protocols.[27] RbCl and [Ru(DIP)(dppz)]Cl_2 were used as positive and negative controls, respectively. Briefly, 1×10^6 HCT116N or HCT116O cells were plated into 6-well tissue culture treated plates and allowed to adhere for 24 h. Metabolic inhibitors (5 μM oligomycin in ethanol and 50 mM 2-deoxy-D-glucose) or control solutions (5 mM glucose and ethanol) were added to the cell culture media and samples were incubated for 1 h. Media was removed by aspiration and each well was washed with PBS. Media (3 mL) containing the **Rh−O** metalloinsertor [Rh(phen)(chrysi)(PPO)]Cl_2 (0.5 μM), the parent metalloinsertor [$Rh(bpy)_2$(chrysi)]Cl_3 (10 μM), [Ru(DIP)(dppz)]Cl_2 (2 μM), or RbCl (25 μM) was then added to each well and incubated for 1 h. Media was aspirated and cells were rinsed with PBS to remove surface rhodium, ruthenium, or rubidium. Cells were lysed directly in the well using 1 mL of 1% SDS solution. Samples were transferred to microcentrifuge tubes and sonicated for 10 s at 20% amplitude on a Qsonica Ultrasonic sonicator. Cell lysate was combined with an equal volume of 2% HNO_3 and analyzed for Rh, Ru, and Rb content on an Agilent 8800 Triple Quadrupole ICP-MS, and the concentration of Rh, Ru, or Rb in each sample was determined by comparison to a standard curve (ranging from 1-100 ppb) and normalized using the protein content of each sample. The protein content of

each sample was determined using a Pierce BCA assay, following the manufacturer's instructions. It is of note that temperature-dependence uptake experiments were attempted for these complexes as well, however challenges with solubility of metalloinsertors at low concentrations made results challenging to interpret.

2.3 Results

2.3.1 Establishing the Enantiomeric Activity of $[Rh(phen)(chrysi)(PPO)]^{2+}$

Enantiomeric separation was performed for the complex $[Rh(phen)(chrysi)(PPO)]^{2+}$ to establish the interaction of its Δ- and Λ-enantiomers with DNA *in vitro* and in MMR-deficient or -proficient cells in culture. The Δ- and Λ-enantiomers of $[Rh(phen)(chrysi)(PPO)]^{2+}$ were isolated with >90% and >95% enantiomeric excess, respectively (**Figure 2.3**). Circular dichroism experiments confirmed the enantiomeric nature of the isolated complexes, and no racemization was observed at ambient temperature over 1 month. Competition titrations between $[Rh(phen)(chrysi)(PPO)]^{2+}$ and the photocleaving metalloinsertor $[Rh(bpy)_2(chrysi)]^{3+}$ in the presence of ^{32}P-radiolabeled DNA containing a CC mismatch revealed both enantiomers are capable of binding mismatched DNA base pairs with similar affinity (10^6 M^{-1}, Table 1).[10] Furthermore, both enantiomers were found to have selective cytotoxic effects towards MMR-deficient cells over MMR-proficient cells in MTT experiments (**Figure 2.3**). These studies confirm that both enantiomers of the PPO-containing metalloinsertor, $[Rh(phen)(chrysi)(PPO)]^{2+}$, exhibit binding properties towards mismatched DNA that are consistent with a previous generation of **Rh−O** metalloinsertors. These **Rh-O** complexes show no enantiomeric preference in binding

DNA, unlike parent metalloinsertors, which show a high enantiomeric preference for the D-isomer in binding DNA.[15,19]

2.3.2 Binding of Metalloinsertors to a Single Base Pair Mismatch

The binding affinities of $[Rh(L)(chrysi)(PPO)]^{2+}$ metalloinsertors to DNA containing a single CC mismatch were determined. The $[Rh(L)(chrysi)(PPO)]^{2+}$ complexes do not photocleave DNA upon irradiation, so their binding affinities were assayed *via* a competition titration with $[Rh(bpy)_2(chrysi)]^{3+}$, a complex known to photocleave DNA selectively upon mismatch binding and irradiation.[22] A CC mismatch was used as it is highly destabilized relative to other mismatches and therefore undergoes significant photocleavage in the presence of $[Rh(bpy)_2(chrysi)]^{3+}$. A constant concentration of $[Rh(bpy)_2(chrysi)]^{3+}$ and varying concentrations of the competing $[Rh(L)(chrysi)(PPO)]^{2+}$ metalloinsertor were incubated with a DNA hairpin containing a single CC mismatch, irradiated, and the DNA photocleavage products were separated on a denaturing gel. The ratio of photocleaved DNA to intact DNA was plotted against the log of the rhodium concentration and fit to a sigmoidal curve (**Figure 2.4**). The inflection point of the sigmoidal fit was used to determine the binding affinity of the competing $[Rh(L)(chrysi)(PPO)]^{2+}$ metalloinsertor by solving simultaneous equilibria equations using the known binding affinity of $[Rh(bpy)_2(chrysi)]^{3+}$. The binding affinities of these complexes are shown in Table 1. All complexes were tested as racemic mixtures and exhibit binding affinities in the range of 2.4 to 7.2 $\times$ 10^6 M^{-1} (**Table 2.1**). Despite differences in ligand steric bulk, all **Rh−O** metalloinsertors tested have binding affinities within one order of magnitude of each other, and thus bind DNA with comparable affinity. It is also of note that $[Rh(phen)(chrysi)(PPO)]Cl_2$ was also observed to be able to

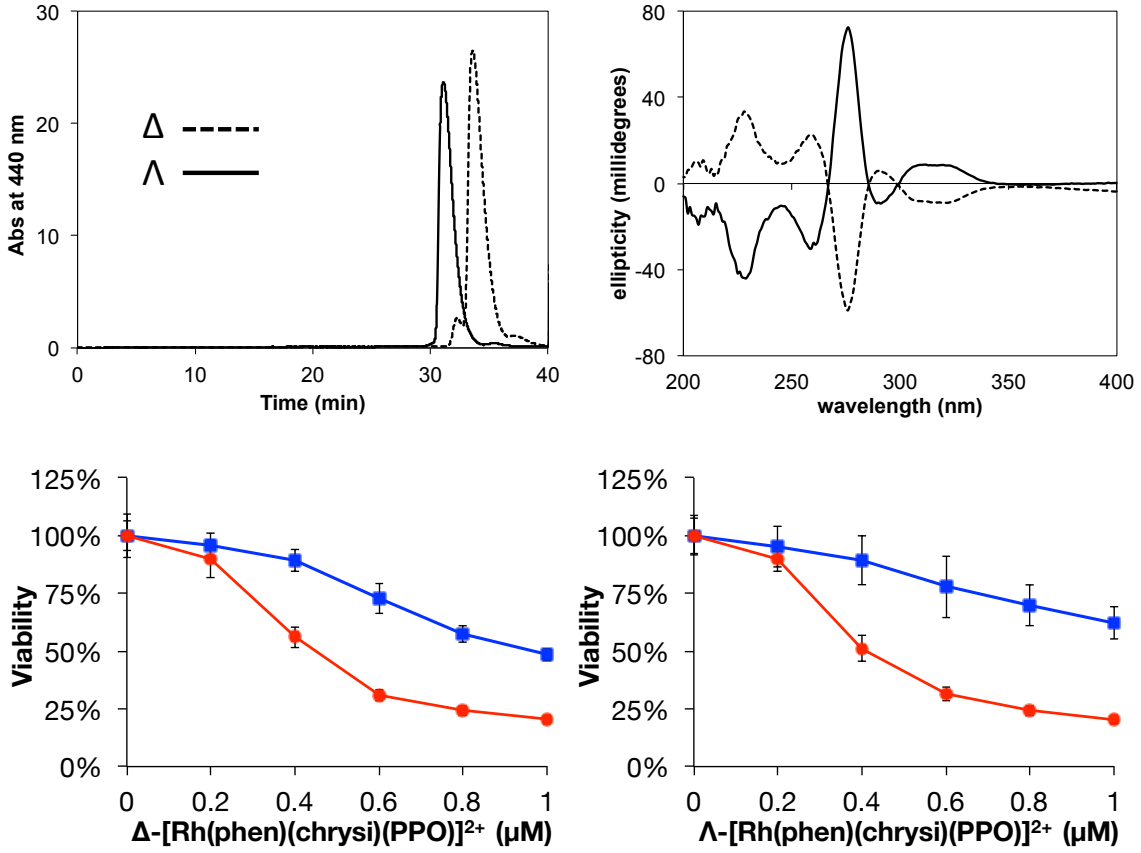

Figure 2.3 Purification and activity of the Δ and Λ enantiomers of $[Rh(phen)(chrysi)(PPO)]^{2+}$. (Top left) HPLC trace of the purified Δ- and Λ-enantiomers, (top right) a CD spectrum showing the enantiomeric nature of the two samples, and MTT assays of the Δ (bottom left) and Λ (bottom right) of $[Rh(phen)(chrysi)(PPO)]Cl_2$ with HCT116N (MMR proficient, blue) and HCT116O (MMR deficient, red) cell lines. Both enantiomers show selective cytotoxicity towards the MMR deficient cell line at similar concentration ranges.

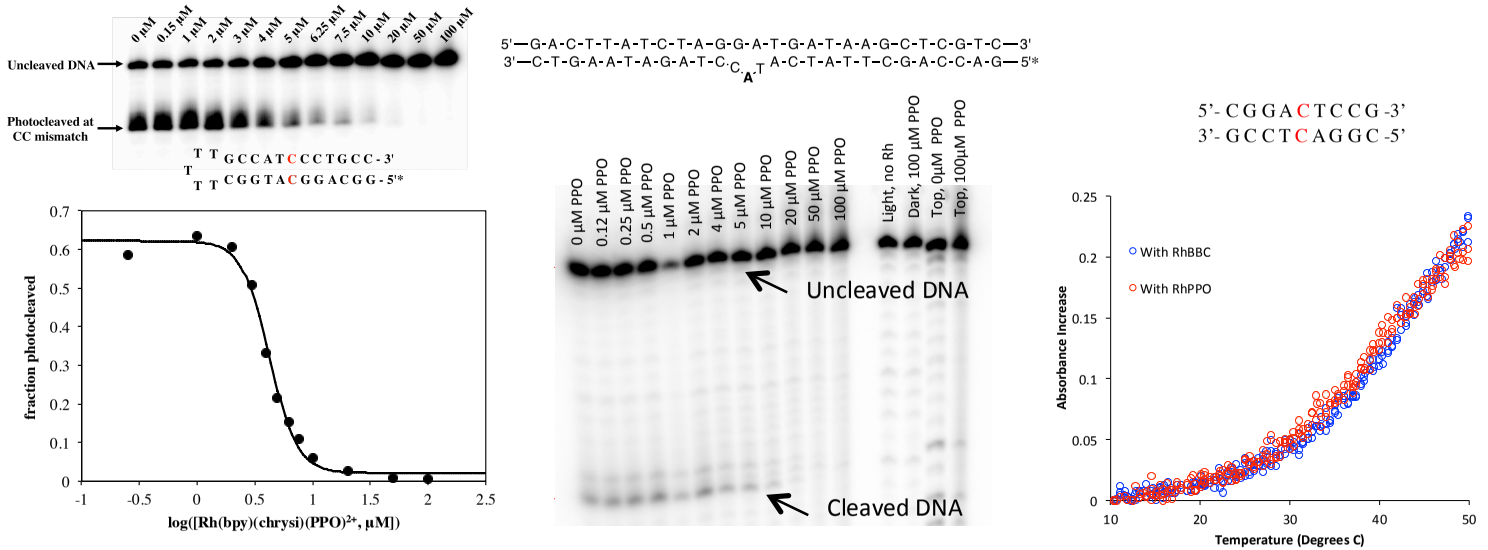

Figure 2.4 Metalloinsertor binding properties to a CC mismatch. (Left) A representative competition titration between [Rh(bpy)(chrysi)(PPO)]$^{2+}$ and [Rh(bpy)$_2$(chrysi)]$^{3+}$ to a hairpin DNA sequence containing a single CC mismatch. As the concentration of [Rh(bpy)(chrysi)(PPO)]$^{2+}$ is increased, [Rh(bpy)$_2$(chrysi)]$^{3+}$ is competed out of the mismatched site and the amount of DNA photocleavage decreases, as seen in the gel image. The photocleaved fraction of DNA is plotted against the log([Rh(bpy)(chrysi)(PPO)$^{2+}$, μM]) and fit with a sigmoidal curve. (Middle) similar results are observed in the presence of a single base bulge. (Right) Melting temperature analysis of a 9-mer containing a central CC mismatch in the presence of [Rh(bpy)$_2$(chrysi)]Cl$_3$ (RhBBC) or [Rh(phen)(chrysi)(PPO)]Cl$_2$ (RhPPO) showed comparable stabilization of the duplex with melting temperatures of 44.9 ± 0.6 and 41.3 ± 0.5 °C, respectively.

bind to a single base bulge, which is representative of insertions/deletions (indels), another potentially biologically relevant target.

Binding was assessed further via melting temperature analysis. A short, palindromic DNA sequence containing a central CC mismatch was incubated in the presence of the parent metalloinsertor, $[Rh(bpy)_2(chrysi)]Cl_3$, or the **Rh−O** metalloinsertor, $[Rh(phen)(chrysi)(PPO)]Cl_2$. The chosen DNA sequence has a low T_m and therefore exists as ssDNA at room temperature.[13] In the presence of metalloinsertor, however, the DNA anneals and the melting temperature increases dramatically to 44.9 ± 0.6 and 41.3 ± 0.5 °C for $[Rh(bpy)_2(chrysi)]Cl_3$ and $[Rh(phen)(chrysi)(PPO)]Cl_2$, respectively (**Figure 2.4**). These results are in good agreement with the results of the DNA binding assay describe above and corroborate the result that parent and **Rh−O** metalloinsertors have comparable binding affinities to mismatches in DNA, with $[Rh(phen)(chrysi)(PPO)]Cl_2$ stabilizing DNA to a slightly lesser extent than $[Rh(bpy)_2(chrysi)]Cl_3$.

2.3.3 pK_a Determination of Metalloinsertors

The pK_a values of $[Rh(L)(chrysi)(PPO)]^{2+}$ metalloinsertors were assessed *via* spectroscopic pH titrations (**Table 2.1**, **Figure 2.5**). The absorbance of a 435-440 nm peak, which corresponds to a charge transfer located on the chrysi ligand, was plotted against the pH of the solution for each complex.[28] Data were fit to a sigmoidal curve and the inflection point was taken as the pK_a of the complex, specifically of the imine proton on the chrysi ligand. All **Rh−O** metalloinsertors exhibited pK_a values in the range of 8.1 to 9.1, which are above physiological pH (**Table 2.1**), indicating that the chrysi ligands of these complexes remain protonated in cell culture media or within cells. It has been

Table 2.1 Binding affinity, pK_a, and Log P values for each metalloinsertor

Metalloinsertor	Binding Constant ($\times 10^6$ M^{-1})[a]	pK_a (2+ to 1+)	Log *P*
Δ-[Rh(phen)(chrysi)(PPO)]$^{2+}$	6.6	–	–
Λ-[Rh(phen)(chrysi)(PPO)]$^{2+}$	9.2	–	–
rac-[Rh(phen)(chrysi)(PPO)]$^{2+}$	5.5[b]	8.3 ± 0.3[a]	1.4 ± 0.1
rac-[Rh(bpy)(chrysi)(PPO)]$^{2+}$	7.2	8.9 ± 0.1	0.68 ± 0.07
rac-[Rh(HDPA)(chrysi)(PPO)]$^{2+}$	3.0	9.1 ± 0.1	0.69 ± 0.08
rac-[Rh(4,7-DMP)(chrysi)(PPO)]$^{2+}$	1.5	9.1 ± 0.1	1.1 ± 0.1
rac-Rh[(5,6-DMP)(chrysi)(PPO)]$^{2+}$	2.3	9.0 ± 0.3	0.71 ± 0.01
rac-[Rh(DIP)(chrysi)(PPO)]$^{2+}$	1.6	8.1 ± 0.1	> 2.0[c]

[a] binding affinities measured using the DNA hairpin 5'-GGCAGG**C**ATGGCTTTTTGCCAT**C**CCTGCC-3' (underline denotes mismatch) in 100 mM NaCl, 20 mM NaP_i, pH 7.1 buffer. Competition titrations were performed against the photocleaving metalloinsertor $[Rh(bpy)_2(chrysi)]Cl_3$.
[b] Values from reference 19
[c] The change in absorbance in the [Rh(DIP)(chrysi)(PPO)]$^{2+}$-containing 1-octanol phase before and after equilibration with the aqueous phase was too small to accurately and consistently measure.

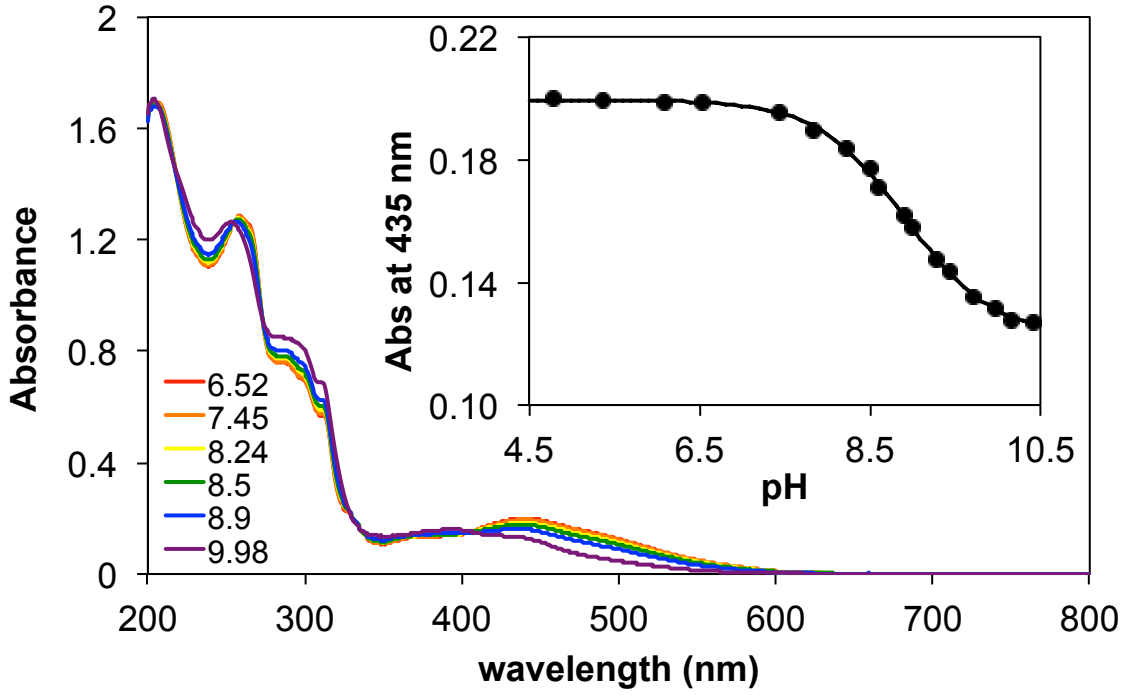

Figure 2.5 Metalloinsertor pH titration to determine pKa. A representative pH titration of $[Rh(bpy)(chrysi)(PPO)]^{2+}$ from a pH of 6.52 to 9.98. The inset shows the absorbance at 435 nm (a chrysi localized charge transfer) plotted against pH and fit to a sigmoidal curve.

shown previously that fully protonated chrysi ligands, which are seen with **Rh−O** metalloinsertors, buckle in contrast to the deprotonated chrysi ligands of the parent metalloinsertors, which are completely flat and thus easy to stack with the DNA base pairs once inserted.[19]

2.3.4 Partition Coefficient and Lipophilicity of Metalloinsertors

The $[Rh(L)(chrysi)(PPO)]Cl_2$ family of metalloinsertors was designed to vary in lipophilicity, and the partition coefficients of each $[Rh(L)(chrysi)(PPO)]^{2+}$ metalloinsertor were determined between aqueous buffer (10 mM Tris-HCl, pH 7.4) and 1-octanol according to literature methods.[24] Absorbance measurements at the ~260 nm peak were made in the 1-octanol phase before and after equilibration with the aqueous phase. These absorbance values were compared to determine the partition coefficient, log P (**Table 2.1, Figure 2.6**). The log P values followed the expected trend with the least bulky complexes ($[Rh(bpy)(chrysi)(PPO)]^{2+}$ and $[Rh(HDPA)(chrysi)(PPO)]^{2+}$) having the lowest log P values and the bulkiest complex ($[Rh(DIP)(chrysi)(PPO)]^{2+}$) having the greatest log P value. Surprisingly, despite their cationic nature, under these conditions the $[Rh(L)(chrysi)(PPO)]^{2+}$ metalloinsertors are all lipophilic and have partition coefficients favoring octanol over water, ranging from 0.68 to >2.0.

2.3.5 Cytotoxic and Anti-Proliferative Effects in Cells

The ability of metalloinsertors to selectively kill or impair growth of MMR-deficient cells is a critical factor in their potential value as chemotherapeutic agents.[19,29] In this structure-activity relationship study, we used ELISA and MTT assays to determine the effect of ligand substitution on biological activity in MMR-deficient and -proficient cells. The ELISA was used to determine the inhibitory effects on DNA synthesis and the

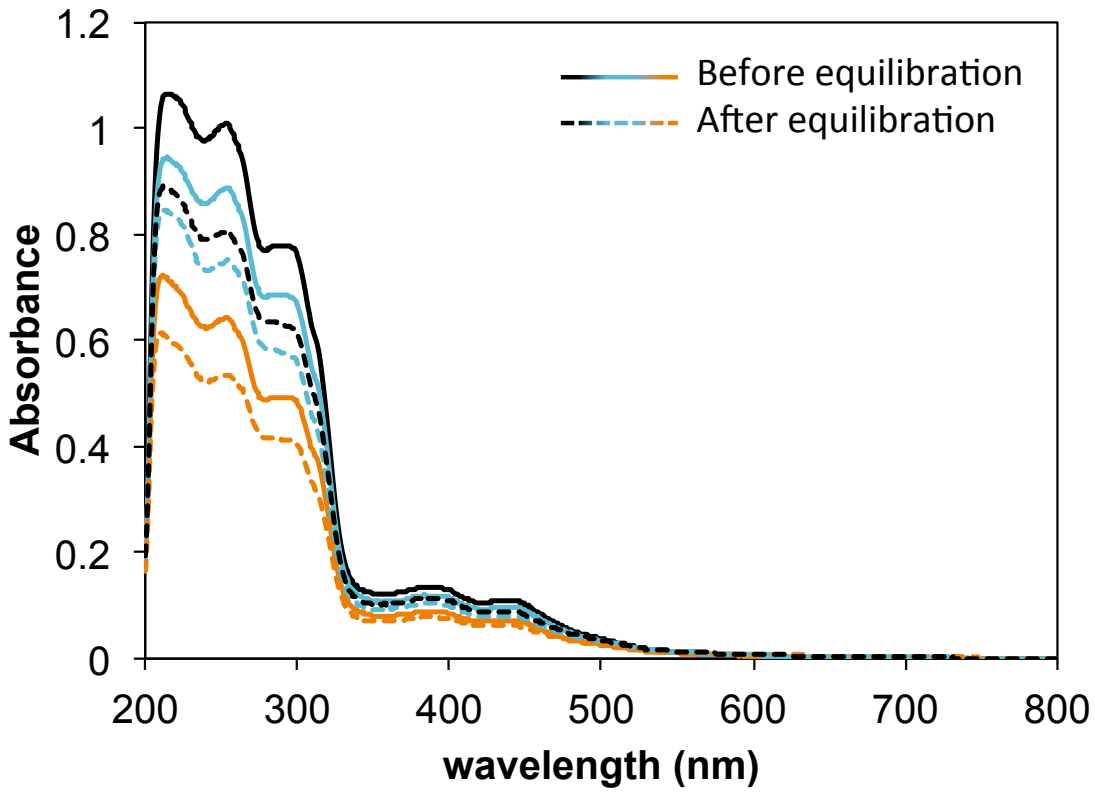

Figure 2.6 Metalloinsertor lipophilicity experiments to determine Log P. A representative absorption spectrum of of $[Rh(bpy)(chrysi)(PPO)]^2$ in 1-octanol before (solid lines) and after (dashed lines) equilibration with an aqueous solution at pH 7.4. Each replicate set (before and after trace) is shown as a different color (black, blue, and orange) with the before trace shown as a solid line and the after trace shown as a dashed line.

MTT assay was performed to establish levels of cytotoxicity. For the ELISA, each metalloinsertor was incubated with HCT116N (MMR-proficient) or HCT116O (MMR-deficient) cells at various concentrations before treatment with the unnatural nucleic acid BrdU. Colorimetric antibody treatment allowed the relative BrdU incorporation into DNA to be quantified, and cellular proliferation was then determined as the ratio of BrdU incorporation between metalloinsertor-treated cells and untreated control cells. The results of the 48-hour metalloinsertor treatment are shown in **Figure 2.7**, and the results of a 24-hour treatment are shown in **Figure 2.8**. All $[Rh(L)(chrysi)(PPO)]^{2+}$ metalloinsertors exhibit anti-proliferative activity with selectivity towards the MMR-deficient cell line. The maximum proliferation difference (referred to as selectivity) between the cell lines and the concentration at which this selectivity occurs (referred to as potency) are as follows: 77 ± 10% at 400 nM for $[Rh(phen)(chrysi)(PPO)]^{2+}$, 78 ± 18% at 2 μM for $[Rh(bpy)(chrysi)(PPO)]^{2+}$, 47 ± 10% at 25 μM for $[Rh(HDPA)(chrysi)(PPO)]^{2+}$, 66 ± 6% at 400 nM for $[Rh(4,7\text{-}DMP)(chrysi)(PPO)]^{2+}$, 67 ± 5% at 400 nM for $[Rh(5,6\text{-}DMP)(chrysi)(PPO)]^{2+}$, and 70 ± 23% at 160 nM for $[Rh(DIP)(chrysi)(PPO)]^{2+}$.

For the MTT assay, each metalloinsertor was incubated with HCT116N (MMR-proficient) or HCT116O (MMR-deficient) cells at various concentrations before the addition of MTT, which can be converted into formazan by mitochondrial reductase activity in a functioning cell. Colorimetric measurements of formazan allow the relative viability to be quantified, and cellular viability is then determined as the ratio of formazan produced between metalloinsertor-treated cells and untreated control cells. The results of the 72-hour treatment are shown in **Figure 2.9** and the results of the 24-hour treatment are shown in **Figure 2.10**. All $[Rh(L)(chrysi)(PPO)]^{2+}$ metalloinsertors exhibit

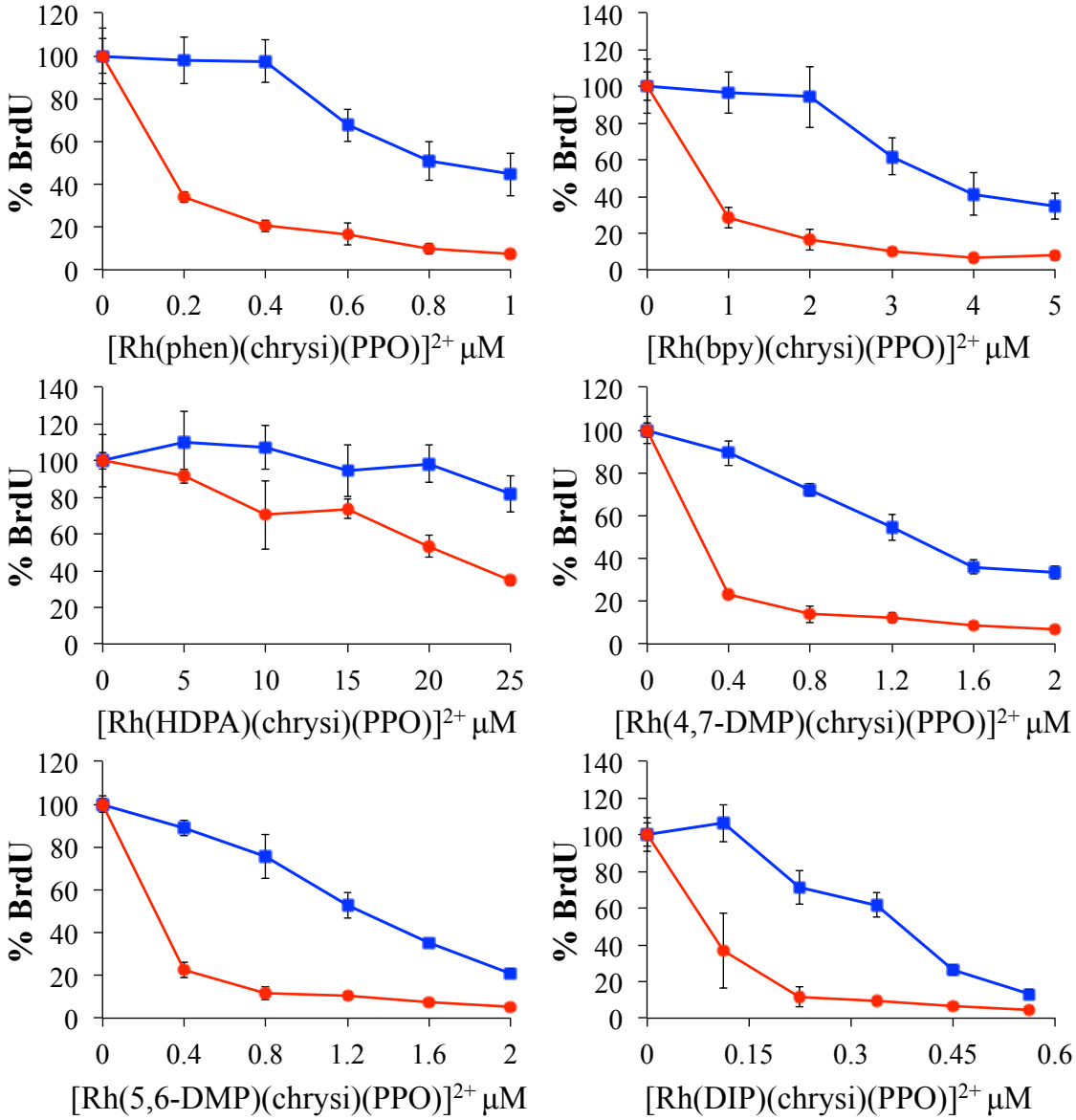

Figure 2.7 48-hour ELISA assay on metalloinsertors. Cellular proliferation ELISA for the $[Rh(L)(chrysi)(PPO)]^{2+}$ metalloinsertors in MMR-deficient (HCT116O, red circles) and MMR-proficient (HCT116N, blue squares) cells. Cells were incubated with various concentrations of metalloinsertor for 48 h before treatment with BrdU. Cell proliferation is shown as %BrdU incorporated into DNA compared to untreated control cells. Error is shown as the standard deviation of 5 replicates.

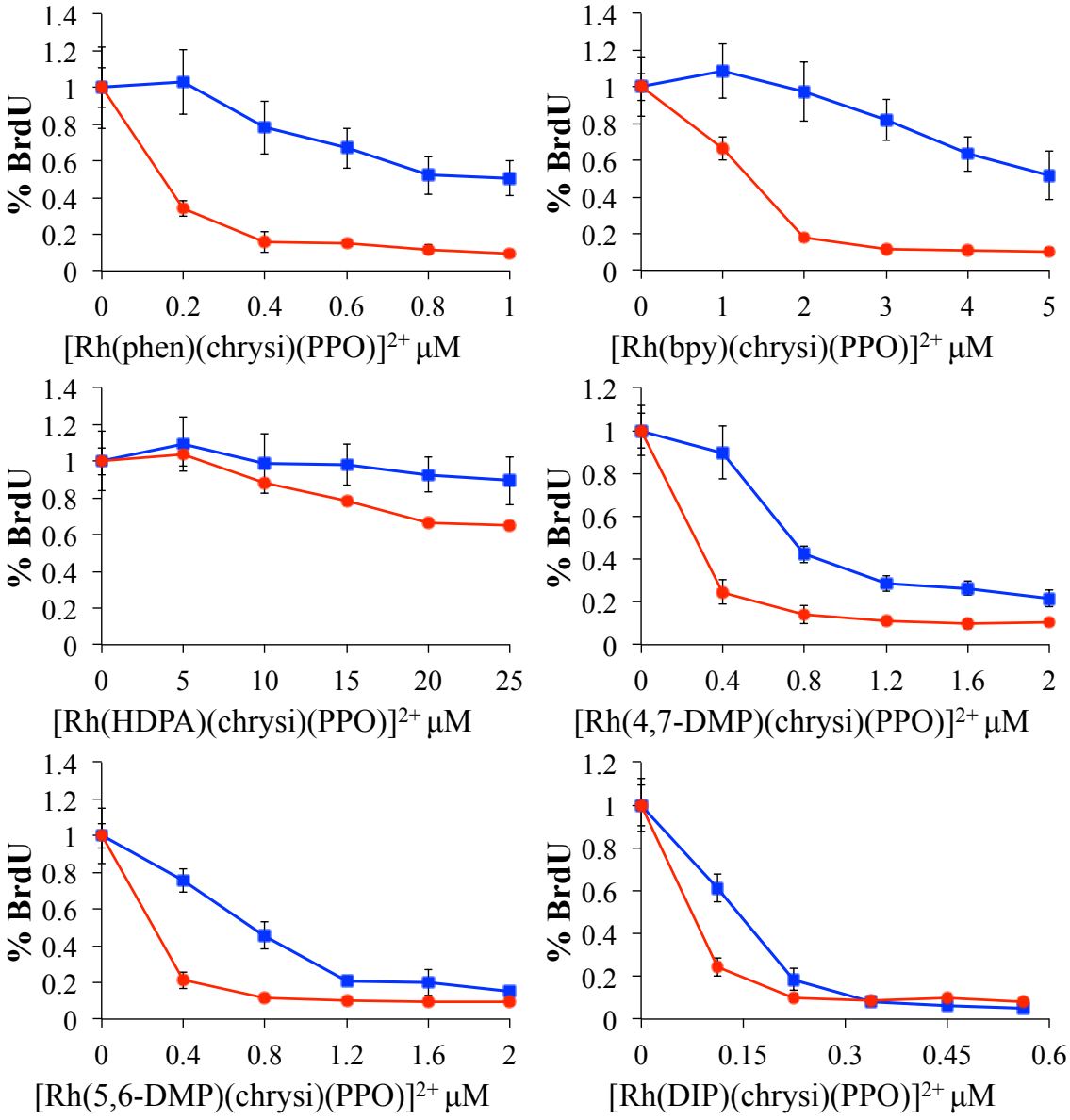

Figure 2.8 24-hour ELISA assay on metalloinsertors. Cellular proliferation ELISA for the $[Rh(L)(chrysi)(PPO)]^{2+}$ metalloinsertors in MMR-deficient (HCT116O, red circles) and MMR-proficient (HCT116N, blue squares) cells. Cells were incubated with various concentrations of metalloinsertor for 24 h before treatment with BrdU. Cell proliferation is shown as %BrdU incorporated into DNA compared to untreated control cells. Error is shown as the standard deviation of 5 replicates.

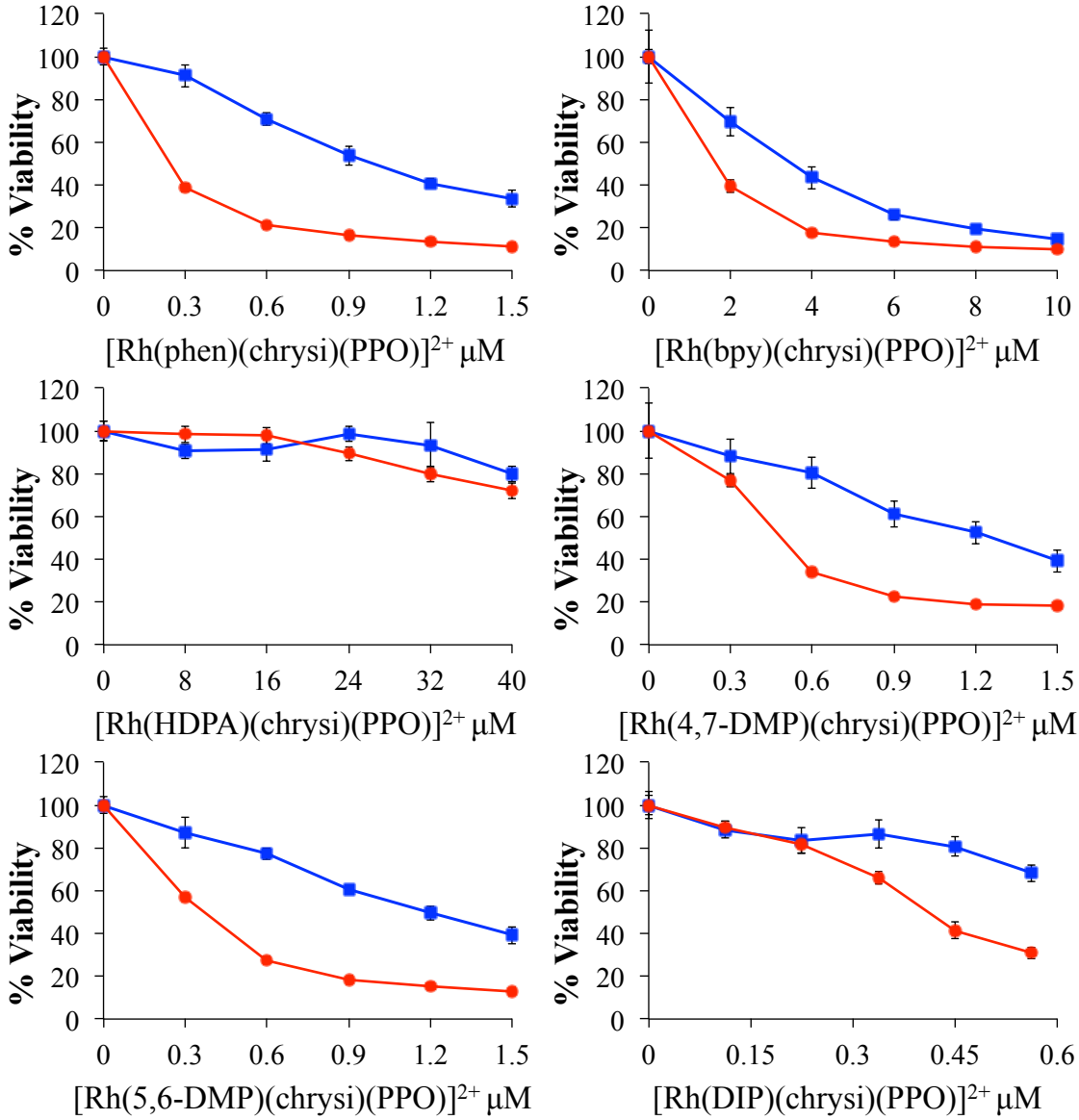

Figure 2.9 72-hour MTT assay on metalloinsertors. Cellular viability MTT assay for the $[Rh(L)(chrysi)(PPO)]^{2+}$ metalloinsertors in MMR-deficient (HCT116O, red circles) and MMR-proficient (HCT116N, blue squares) cells. Cells were incubated with various concentrations of metalloinsertor for 72 h before treatment with MTT. Cell proliferation is shown as % viability from MTT metabolism, compared to untreated control cells. Error is shown as the standard deviation of 5 replicates.

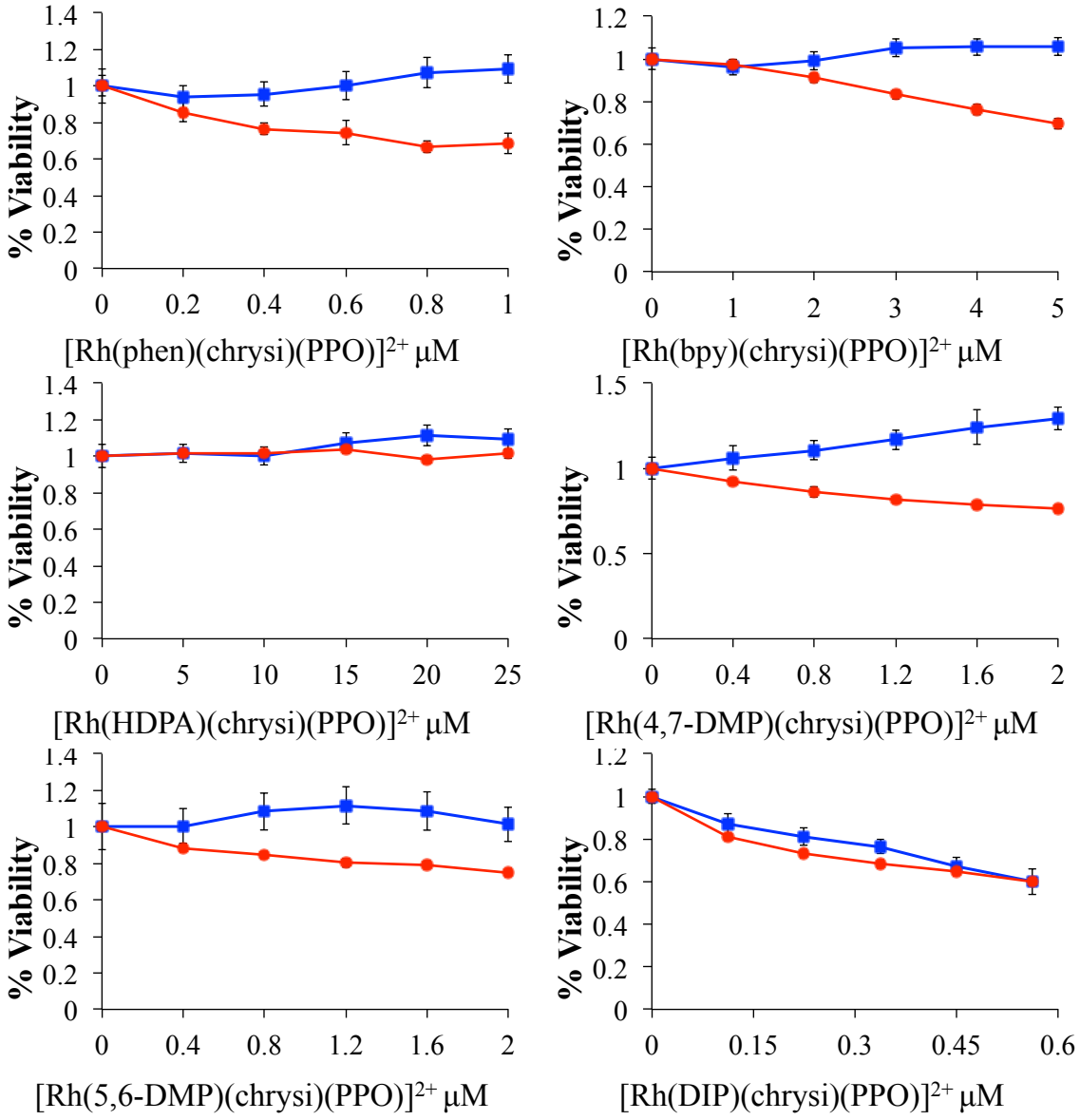

Figure 2.10 24-hour MTT assay on metalloinsertors. Cellular viability MTT assay for the $[Rh(L)(chrysi)(PPO)]^{2+}$ metalloinsertors in MMR-deficient (HCT116O, red circles) and MMR-proficient (HCT116N, blue squares) cells. Cells were incubated with various concentrations of metalloinsertor for 24 h before treatment with MTT. Cell proliferation is shown as % viability from MTT metabolism, compared to untreated control cells. Error is shown as the standard deviation of 5 replicates.

cytotoxic activity with selectivity towards the MMR-deficient cell line. The maximum proliferation difference between the cell lines and the concentration at which this difference occurs are as follows: 52 ± 5% at 300 nM for $[Rh(phen)(chrysi)(PPO)]^{2+}$, 30 ± 7% at 2 μM for $[Rh(bpy)(chrysi)(PPO)]^{2+}$, 13 ± 11% at 32 μM for $[Rh(HDPA)(chrysi)(PPO)]^{2+}$, 46 ± 8% at 600 nM for $[Rh(4,7\text{-}DMP)(chrysi)(PPO)]^{2+}$, 49 ± 3% at 600 nM for $[Rh(5,6\text{-}DMP)(chrysi)(PPO)]^{2+}$, and 39 ± 6% at 640 nM for $[Rh(DIP)(chrysi)(PPO)]^{2+}$. It is of note that these low concentrations are observed even when fetal bovine serum (FBS), which contains proteins that often bind and sequester small molecules, such as BSA, is used. The results of the BSA binding assay showed that pre-incubation of the metalloinsertor with BSA had little effect on metalloinsertor activity in cells (**Figure 2.11**), suggesting that these proteins do no sequester the metalloinsertor or metalloinsertor sequestration is not detrimental to activity.

2.3.6 Whole-Cell Uptake, Uptake Mechanism, and Organelle Localization.

To better understand the range of biological activities of these complexes, cellular uptake and mechanism of uptake were examined *via* ICP-MS based assays. 24-hour ELISA and MTT assays were performed to determine a suitable concentration for uptake and localization studies (which were performed over a 24-hour timescale). To minimize cell death in this assay, a factor which can complicate data interpretation, suitable dosing was determined to be at a concentration at which there was noticeable anti-proliferative effects in the HCT116O cells *via* ELISA but no significant cytotoxicity *via* MTT assay. Whole cell uptake studies were performed with each $[Rh(L)(chrysi)(PPO)]^{2+}$ complex at 0.5 μM with the exception of $[Rh(DIP)(chrysi)(PPO)]^{2+}$, which was performed at 0.2 μM due to its high cytotoxicity at 0.5 μM. For whole cell uptake studies, cells were incubated

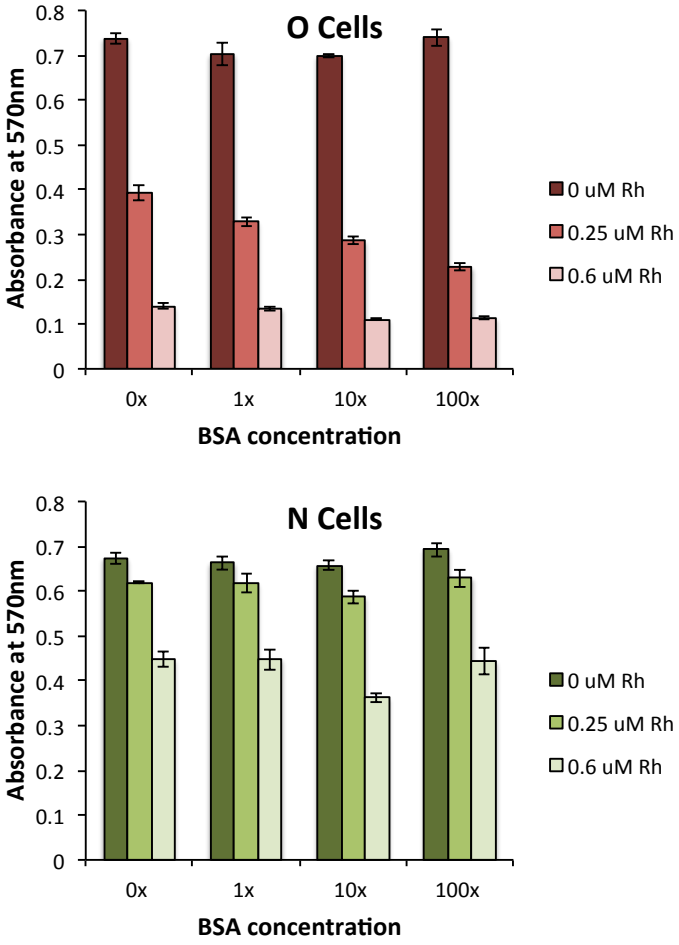

Figure 2.11 Metalloinsertor activity after pre-incubation with BSA. Two concentrations of $[Rh(phen)(chrysi)(PPO)]^{2+}$were pre-incubated with various concentrations of BSA before addition to HCT116N and HCT116O cells. Pre-incubation with BSA appeared to have minimal effect on the toxicity of the metalloinsertor, though some BSA concentration dependence may be visible for the 0.25 μM treatment in HCT116N cells; however, no dependence is seen with 0.25 μM treatment in HCT116N cells or in the 0.60 μM treatment in either cell line.

with metalloinsertors for 24 h before they were lysed and analyzed for rhodium content *via* ICP-MS, with rhodium concentrations normalized to the protein content of each sample. The whole cell uptakes of each metalloinsertor in HCT116O cells are shown in **Figure 2.12**. Similar results were seen in HCT116N cells (**Figure 2.12**). Overall, all $[Rh(L)(chrysi)(PPO)]^{2+}$ complexes exhibit uptake into cells at concentrations within one order of magnitude of each other. The uptake of these complexes correlates generally with their lipophilicity values, with the least lipophilic complexes ($[Rh(HDPA)(chrysi)(PPO)]^{2+}$ and $[Rh(bpy)(chrysi)(PPO)]^{2+}$) having the poorest uptake and the most lipophilic complex ($[Rh(DIP)(chrysi)(PPO)]^{2+}$) having the highest uptake. Lipophilicity has long been correlated with an increase in cellular uptake and a resultant increase in drug potency.[30,31]

In addition to examining whole cell uptake of the $[Rh(L)(chrysi)(PPO)]^{2+}$ metalloinsertors, the uptake over time and the mechanism of uptake were also examined. In the former experiment, cells were incubated with a metalloinsertor for 0.5, 1, 3, 6, 9, or 24 h before being lysed and analyzed for rhodium content by ICP-MS. The whole-cell uptake over time of these metalloinsertors in HCT116O cells is shown in **Figure 2.12**. Similar results were seen in HCT116N cells (**Figure 2.12**). The complexes appear to show significant increases in uptake over the first 3-6 h of incubation with cells, followed by plateau with no evidence of significant efflux during a 24-hour period. These results are consistent with previous studies on metalloinsertors.[20]

A metabolic inhibition assay was performed to better understand the mechanism of cellular uptake of $[Rh(L)(chrysi)(PPO)]^{2+}$ metalloinsertors. HCT116N and HCT116O cells were pre-treated with the metabolic inhibitors oligomycin A, an inhibitor of

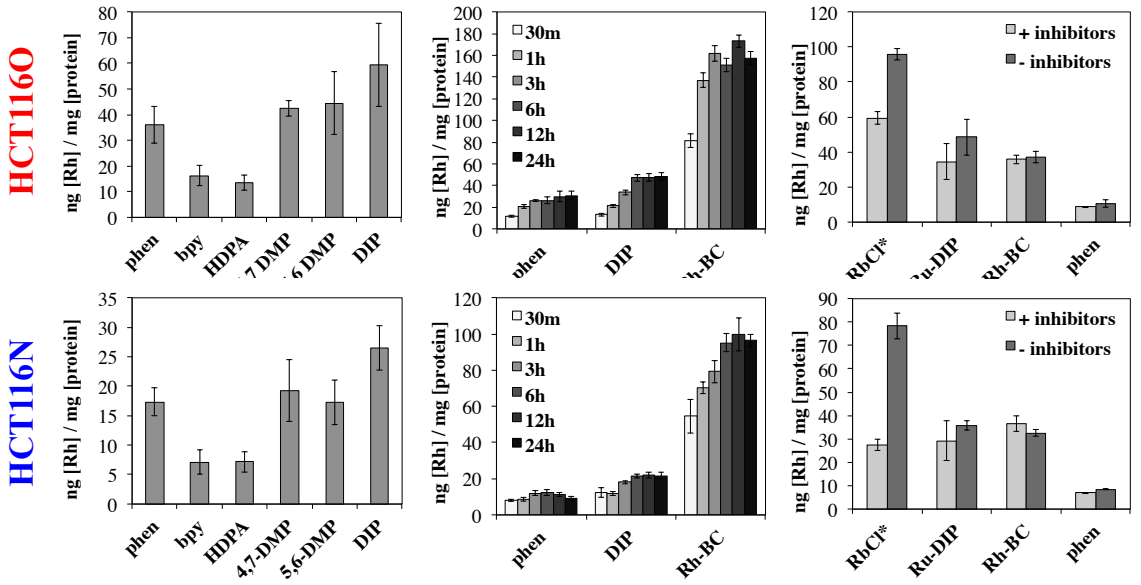

Figure 2.12 Whole-cell rhodium uptake assays in HCT116O (top) and HCT116N (bottom) cells. (Left) Rhodium accumulation was measured by ICP-MS analysis after a 24 hour incubation with $[Rh(\mathbf{L})(chrysi)(PPO)]^{2+}$ metalloinsertors (where **L** = **phen**, **bpy**, **HDPA**, **4,7-DMP**, **5,6-DMP**, or **DIP**). (Middle) Rhodium accumulation over time was measured by ICP-MS for three metalloinsertors, $[Rh(phen)(chrysi)(PPO)]^{2+}$ (**phen**), $[Rh(DIP)(chrysi)(PPO)]^{2+}$ (**DIP**), and the parent metalloinsertor $[Rh(bpy)_2(chrysi)]^{3+}$ (**Rh-BC**). (Right) $[Rh(phen)(chrysi)(PPO)]^{2+}$ (**phen**), $[Rh(bpy)_2(chrysi)]^{3+}$ (**Rh-BC**), $[Ru(DIP)_2(chrysi)]^{2+}$ (**Ru-DIP**), and **RbCl** accumulation was measured by ICP-MS analysis after treatment with or without metabolic inhibitors (oligomycin and 2-deoxy-D-glucose). RbCl* indicates that Rb concentrations for RbCl have been lowered by a factor of 500 in this graphic. Rhodium, ruthenium, and rubidium contents were normalized to protein content determined by BCA assay. Each experiment was performed in triplicate and averaged, with error shown as the standard deviation.

oxidative phosphorylation, and 2-deoxy-D-glucose, an inhibitor of glycolysis.[27] Metabolic inhibition depletes cellular ATP (adenosine triphosphate), so any compound that is taken into the cell *via* an active, ATP-dependent mechanism should have reduced uptake in metabolically depleted cells. Conversely, complexes taken into the cell *via* a passive mechanism, such as passive diffusion, are not affected by metabolic inhibition and therefore the drug should accumulate in inhibited and uninhibited cells at similar concentrations. $[Rh(phen)(chrysi)(PPO)]^{2+}$ and the parent metalloinsertor, $[Rh(bpy)_2(chrysi)]^{3+}$, were studied to determine if the mechanism of metalloinsertor uptake was ATP-dependent. The compounds RbCl and $[Ru(dppz)(DIP)_2]^{2+}$ were included as positive and negative controls, respectively. The rubidium ion of RbCl is transported into the cell by Na,K-ATPase, an ATP-dependent ion pump, while $[Ru(dppz)(DIP)_2]^{2+}$ has previously been shown to enter the cell *via* passive diffusion.[27, 32] Cells were treated with each compound for 1 h before they were lysed and analyzed by ICP-MS for metal content. As rubidium, ruthenium, and rhodium are not naturally present in cells or cell culture reagents, all three elements can be analyzed as low-background analytes by ICP-MS. The results of each compound in HCT116O cells are shown in **Figure 2.12**. Similar results were seen in HCT116N cells (**Figure 2.12**). As expected, RbCl showed a significant decrease in uptake when pre-treated with metabolic inhibitors and $[Ru(dppz)(DIP)_2]^{2+}$ was unaffected by inhibitor pre-treatment. Similar to $[Ru(dppz)(DIP)_2]^{2+}$, $[Rh(phen)(chrysi)(PPO)]^{2+}$ and $[Rh(bpy)_2(chrysi)]^{2+}$ were also unaffected by inhibitor pre-treatment, suggesting these complexes are also taken into the cell via an ATP-independent mechanism, such as passive diffusion. Since these complexes are all lipophilic and cationic, passive diffusion is a reasonable uptake

mechanism, with the negative membrane potential driving diffusion and relatively high lipophilicity facilitating the process as the molecules can more readily partition into the cellular membranes.[33]

Subcellular localization into the nucleus (the on-target organelle) and mitochondria (a major off-target organelle) were also examined by an ICP-MS assay. Localization studies were performed with each $[Rh(L)(chrysi)(PPO)]^{2+}$ metalloinsertor at 0.5 μM with the exception of $[Rh(DIP)(chrysi)(PPO)]^{2+}$, which was performed at 0.2 μM. For localization studies, cells were incubated with metalloinsertors for 24 h before they were lysed and analyzed for rhodium content via ICP-MS, with rhodium concentrations normalized to the protein content of each sample. The whole cell uptakes of each metalloinsertor in HCT116O cells are shown in **Figure 2.13**. Similar results were seen in HCT116N cells (**Figure 2.13**). Overall, all $[Rh(L)(chrysi)(PPO)]^{2+}$ complexes have comparable nuclear uptakes and mitochondrial uptakes to one another with the exception of $[Rh(DIP)(chrysi)(PPO)]^{2+}$, which has nuclear and mitochondrial uptakes that are 2-3 times higher than other complexes despite being dosed at a lower concentration. All complexes appear to enter the nucleus at high enough concentrations to bind DNA mismatches, with a significant enrichment in nuclear concentration over the extracellular concentration of rhodium (**Table 2.2**).

2.4 Discussion

Early generations of rhodium metalloinsertors, which exclusively contain Rh−N ligand coordination, are a richly studied family of metal complexes that can selectively bind to DNA base pair mismatches and lead to selective cell death in MMR-deficient cells. Across multiple studies, these metalloinsertors were determined to have several

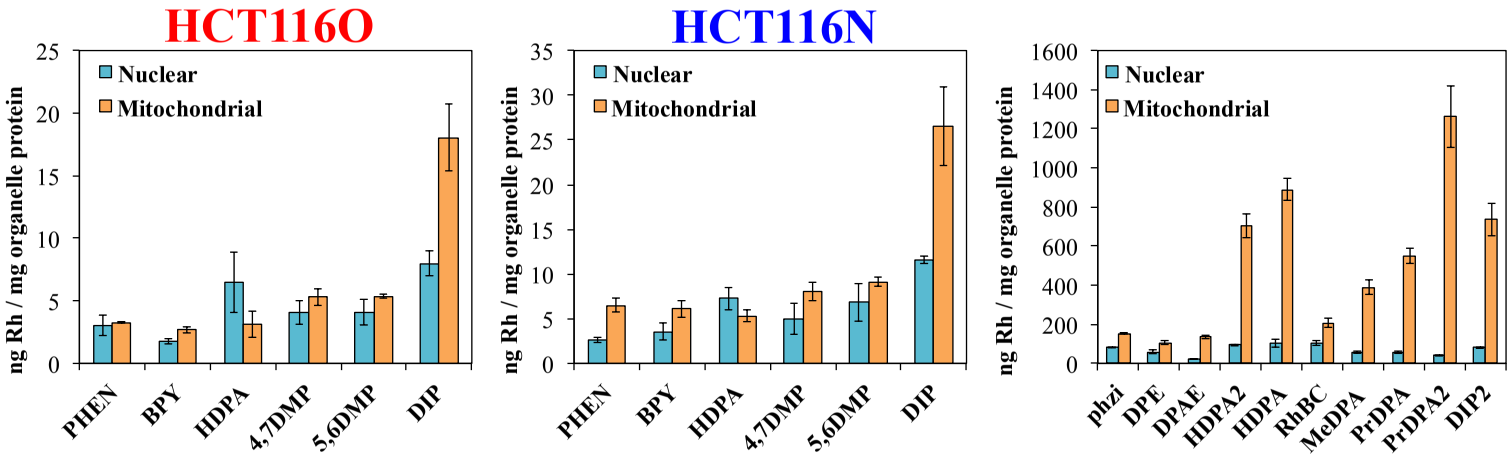

Figure 2.13 ICP-MS assay for nuclear and mitochondrial uptake of rhodium metalloinsertors. Rhodium accumulation in HCT116O (left) and HCT116N (middle) cells was measured by ICP-MS analysis after a 24 hour incubation with $[Rh(\mathbf{L})(chrysi)(PPO)]^{2+}$ (where **L** = **phen**, **bpy**, **HDPA**, **4,7-DMP**, **5,6-DMP** or **DIP**), and (right) comparison to a similar study on metalloinsertors from reference 20 (dosed at 10 μM for all but **DIP2**, 2 μM for **DIP2**). Rhodium content was normalized to protein content of each organelle fraction determined by BCA assay. The ratio of mitochondrial uptake (in ng[Rh]/mg[mitochondrial protein]) to nuclear uptake (in ng [Rh]/mg [nuclear protein]) for each complex is shown above each data set. The results of 4 independent studies were averaged and error is shown as the standard deviation.

Table 2.2 Converted nuclear rhodium content values

	Compound	ng [Rh] / mg [nuclear protein]	ng [Rh] / nuclei × 10^{-8} [a]	[Rh] µM [b]	Increase over extracellular [Rh] [c]
N Cells	**PHEN**	3.0	10.0	3.6	7.2
	BPY	1.8	5.8	2.1	4.2
	HDPA	6.5	21.3	7.7	15.5
	4,7DMP	4.1	13.3	4.8	9.6
	5,6DMP	4.1	13.5	4.9	9.8
	DIP	8.0	26.2	9.5	47.5
	RhBC	26.6	87.2	31.6	3.2
O Cells	**PHEN**	2.6	8.6	3.1	6.3
	BPY	3.5	11.6	4.2	8.4
	HDPA	7.3	23.8	8.6	17.2
	4,7DMP	5.0	16.4	5.9	11.9
	5,6DMP	6.8	22.4	8.1	16.2
	DIP	11.6	38.0	13.7	68.7
	RhBC	37.3	122.2	44.3	4.4

[a] a conversion factor of 3.28×10^{-8} mg nuclear protein / nuclei was determined in reference 20

[b] the nucleus was approximated as a sphere of radius 4µm as described in reference 20

[c] Increase taken as ratio between the nuclear rhodium concentration and the dosing concentration of each metalloinsertor.

characteristic and consistent behaviors. Through *in vitro* experiments, we have observed that only the Δ- enantiomer of these Rh−N coordinated complexes is capable of binding mismatches in B-form DNA.[34] In cellular studies, these metalloinsertors have been observed to selectively kill cells in concentration ranges of 5-40 μM.[20,21] In one structure-activity relationship study, the steric bulk of the ancillary ligands on a metalloinsertor was seen to influence DNA binding properties and, ultimately, alter cellular selectivity.[21] In another structure-activity relationship study, the lipophilicity of the ancillary ligands on a metalloinsertor was seen to dramatically influence its subcellular localization within a cell and, again, alter cellular selectivity.[20]

While the above trends seem to ring true across parent metalloinsertors containing exclusively Rh−N ligand coordination, the recent emergence of a new family of metalloinsertors that contain Rh−O ligand coordination has challenged many of these characteristics and behaviors.[19] For instance, both enantiomers of **Rh−O** metalloinsertors are capable of binding DNA mismatches *in vitro*, and are furthermore capable of inducing selective cellular toxicity at *nanomolar* concentrations. Additionally, changes in lipophilicity and steric bulk of the O-containing ligand seemed to have little, if any, effect on DNA binding affinity and cellular selectivity. This remarkable shift in metalloinsertor activity revealed that these **Rh−O** complexes have distinct *in vitro* characteristics and biological properties from their parent metalloinsertor complexes. As such, a new family of **Rh−O** metalloinsertors has been synthesized, characterized, and investigated for biological activity. In contrast to the first generation of **Rh−O** metalloinsertors in which the O-containing ligand was varied, in this new family an ancillary ligand was varied and the O-containing ligand was kept constant. This family is of the form

[Rh(L)(chrysi)(PPO)]$^{2+}$, where L = bpy, phen, HDPA, 4,7-DMP, 5,6-DMP, and DIP. This ligand variation influences many features of the metalloinsertor, including steric bulk and lipophilicity, both of which have previously been seen to affect DNA binding and cellular activity of the parent metalloinsertors.[20,21] In studying this family of complexes, we aimed to test the unique biological activity of metalloinsertors containing the **Rh−O** ligand framework and begin to understand the high potency and improved selectivity exhibited by these metalloinsertors over parent metalloinsertors and other DNA-binding complexes.

2.4.1 Robustness of Biological Activity of the Rh−O Ligand Framework

A primary aim of this structure-activity relationship study was to determine if altering the ancillary ligand of **Rh−O** metalloinsertors would significantly affect the biological activity of these complexes. Biological activity was assessed through both ELISA and MTT assays in two cell lines, HCT116N and HCT116O. These cells are derived from the same colorectal carcinoma cell line but differ primarily in that HCT116N cells are MMR-proficient whereas HCT116O cells are MMR-deficient.[35] For this reason, HCT116O cells have a higher relative abundance of DNA mismatches over HCT116N cells and therefore should be more sensitive to mismatch-targeting metalloinsertors.[36]

Indeed, all complexes prepared showed highly selective anti-proliferative or cytotoxic effects toward the MMR-deficient cells over the MMR-proficient cells in both ELISA (**Figure 2.7**) and MTT assays (**Figure 2.9**), with the exception of [Rh(HDPA)(chrysi)(PPO)]$^{2+}$, which only shows activity in the ELISA. While selectivity was seen for all complexes, the effective concentrations varied by two orders of

magnitude across the family. For instance, $[Rh(HDPA)(chrysi)(PPO)]^{2+}$ has very low potency and little selectivity compared to other **Rh-O** metalloinsertors. Although it does appear to interfere selectively with DNA synthesis *via* ELISA, this biological interaction does not appear significant enough to produce cytotoxic effects in the MTT assay, even at high drug concentrations (**Figure 2.9**). HDPA is the only ligand containing a labile proton and the only ligand that forms a 6-ring chelate with the metal, and it seems possible that these structural features ultimately influence the biological activity of the $[Rh(HDPA)(chrysi)(PPO)]^{2+}$. It is possible that the 6-member chelate could cause structural aberrations and the proton on HDPA could cause hydrogen-bonding interactions that ultimately alter DNA-binding or DNA-processing by proteins, which could cause a decrease in toxicity. $[Rh(bpy)(chrysi)(PPO)]^{2+}$ has the second lowest potency of this new family, though remarkably this complex still shows higher potency than the parent metalloinsertors containing only Rh−N coordination.[20] The phenanthroline-derived metalloinsertors, $[Rh(phen)(chrysi)(PPO)]^{2+}$, $[Rh(4,7\text{-}DMP)(chrysi)(PPO)]^{2+}$, and $[Rh(5,6\text{-}DMP)(chrysi)(PPO)]^{2+}$, all show comparable nanomolar potencies and selectivities in the ELISA and MTT assays.

Perhaps the most surprising biological activity is seen with $[Rh(DIP)(chrysi)(PPO)]^{2+}$. Historically, metalloinsertors containing the bulky DIP ligand have shown no selectivity for the MMR-deficient cell line.[21] This lack of selectivity was attributed to substantially lower mismatch binding affinities (10^4 M^{-1} for $[Rh(DIP)_2(chrysi)]^{3+}$) owing to ancillary bulk, as well as off-target localization into the mitochondria, a property that is common with lipophilic cations.[20,37] $[Rh(DIP)(chrysi)(PPO)]^{2+}$, however, *does* exhibit selective cytotoxicity towards MMR-

deficient cells over proficient cells in both the ELISA and MTT assays. In fact, $[Rh(DIP)(chrysi)(PPO)]^{2+}$ displays a similar selectivity and ~2-fold higher potency than $[Rh(phen)(chrysi)(PPO)]^{2+}$ when measured by ELISA (**Figure 2.7**).

Overall, these results confirm that **Rh−O** metalloinsertor biological selectivity is minimally influenced by substitution at the ancillary ligand.[19] Thus far, all of the **Rh−O** metalloinsertors, derivatized at the O-containing ligand or ancillary ligand, have exhibited selectivity in ELISA and/or MTT assays, regardless of steric bulk or lipophilicity, factors that had heavily influenced (and sometimes abolished) the selectivity of parent metalloinsertors. It is noteworthy that this selectivity profile, wherein the **Rh−O** metalloinsertors selectively kill MMR-deficient cells, is shared with the parent complexes and is in stark contrast to what is seen with all other DNA-targeting therapeutics, which preferentially kill MMR-proficient cells.[17,18] Although parent and **Rh−O** metalloinsertors share this unique selectivity profile and have similar *in vitro* binding properties, suggesting they should interact with DNA in a similar way, the **Rh−O** metalloinsertors are dramatically more potent than the parent metalloinsertors, with nearly all **Rh−O** complexes (with the sole exception being $[Rh(HDPA)(chrysi)(PPO)]^{2+}$) having greater cytotoxicity in MMR-deficient cells than *any* of the parent metalloinsertors. It stands to reason, then, that the high potency and selectivity of these **Rh−O** complexes does not reflect a difference in DNA binding affinity from the parent complexes, but rather it must instead reflect a difference in structure associated with the DNA-metalloinsertor lesion. That is, if the frequency of DNA binding is comparable between the **Rh−O** and parent metalloinsertors, the lesion formed by **Rh−O** metalloinsertors must activate a cellular response at lower concentrations.

2.4.2 Uptake Characteristics

Although the $[Rh(L)(chrysi)(PPO)]^{2+}$ family shows consistent activity towards MMR-deficient cells, the selectivities and potencies of these complexes vary significantly across the family from 160 nM to 25 μM. It was initially hypothesized that these differences in biological activity could be due to differences in cellular uptake. In particular, it seemed possible that the least potent complexes, $[Rh(HDPA)(chrysi)(PPO)]^{2+}$ (which has almost no cytotoxic properties at 40 μM) and $[Rh(bpy)(chrysi)(PPO)]^{2+}$ (which has nearly 10-fold lower potency than $[Rh(phen)(chrysi)(PPO)]^{2+}$), could be less effective due to low uptake. Similarly, it was proposed that increased uptake could be responsible for the high potency of $[Rh(DIP)(chrysi)(PPO)]^{2+}$. Indeed, it does seem possible that uptake may explain some of the observed potency trends: despite being dosed at 0.2 μM, $[Rh(DIP)(chrysi)(PPO)]^{2+}$ exhibits similar uptake to $[Rh(phen)(chrysi)(PPO)]^{2+}$, which was dosed at 0.5 μM. The finding suggests that $[Rh(DIP)(chrysi)(PPO)]^{2+}$ may induce biological effects at roughly half the concentration of $[Rh(phen)(chrysi)(PPO)]^{2+}$ as a result of complexes exhibiting similar uptakes at these concentrations. However, uptake alone appears insufficient to explain the potencies of other complexes. For instance, $[Rh(HDPA)(chrysi)(PPO)]^{2+}$ and $[Rh(bpy)(chrysi)(PPO)]^{2+}$ have comparably low uptake into the cell despite a >10-fold difference in activity.

Organelle-specific uptake is also worthy of consideration when examining the activity of these complexes. Studies on previous generations of parent metalloinsertors bearing solely Rh-N ligand coordination showed that off-target mitochondrial uptake is strongly influenced by ligand lipophilicity, with the most lipophilic parent

metalloinsertors having high mitochondrial uptake and low selectivity for MMR-deficient cells.[20,38] Surprisingly, *all* **Rh-O** metalloinsertors studied here are more lipophilic than *any* of the parent metalloinsertors described above, yet all **Rh-O** complexes exhibit selective cytotoxicity towards MMR-deficient cells, making their selectivity patterns distinct from trends followed by the parent metalloinsertors. To better understand this marked change in trends, on-target nuclear localization and off-target mitochondrial localization experiments were performed to assess the biological activity of $[Rh(L)(chrysi)(PPO)]^{+2}$ complexes, particularly DIP, which shows selectivity despite its very high lipophilicity.

As indicated, all $[Rh(L)(chrysi)(PPO)]^{2+}$ metalloinsertors enter the nuclei to a similar extent and at high enough concentrations to bind DNA mismatches (**Figure 2.13, Table 2.2**). Similarly, all $[Rh(L)(chrysi)(PPO)]^{2+}$ metalloinsertors enter the mitochondria to a comparable extent. Although nuclear and mitochondrial uptake cannot be compared directly (since each is normalized to the total protein in the organelle), the localization patterns of **Rh−O** versus parent metalloinsertors can be compared (**Figure 2.13**). This comparison shows that, unlike their Rh-N coordinated predecessors, **Rh−O** metalloinsertor localization into the mitochondria is not significantly influenced by lipophilicity. In fact, despite being lipophilic, **Rh−O** complexes exhibit uptake profiles that are comparable to *hydrophilic* parent metalloinsertors (which have low mitochondrial uptake) and are distinct from *lipophilic* parent metalloinsertors (which have high mitochondrial uptake). This trend in localization is consistent with the biological activity we observed; similar to the hydrophilic parent metalloinsertors, **Rh−O** complexes are highly selective and show little off-target cytotoxicity. Overall, these data indicate that

Rh−O metalloinsertors are able to maintain their high selectivity and potency because the ligand substitutions do not strongly influence their subcellular localization. Since these complexes exhibit low mitochondrial uptake, off-target mitochondria-induced toxicity does not overwhelm the biological response, and the selective nuclear- and mismatch-mediated response can prevail.

It is also interesting to note that both MMR-proficient HCT116N cells and MMR-deficient HCT116O cells had comparable levels of uptake and similar localization profiles, showing that metalloinsertors enter HCT116N and HCT116O cells at the same rate, through the same passive mechanism, and to the same extent (**Figure 2.12** and **Figure 2.13**). These details support the idea that the biological selectivity seen in these cells is not a feature of different cellular uptake or elimination properties. Furthermore, the nuclear uptake into the MMR-deficient and proficient cells are comparable. Therefore, with similar concentrations of metalloinsertors entering the nuclei and similar mismatch binding affinities, any DNA-mediated cytotoxicity must result from a difference in how the drugs interact with the DNA. Rationally, this difference must depend upon an increased mismatch targeting in MMR-deficient cells, where DNA base pair mismatches are more abundant.[36]

2.4.3 Source of Potency for the Rh−O Metalloinsertors

Although MMR-deficient cells have a relative abundance of mismatches compared to MMR-proficient cells, the total number of mismatches formed during each cellular replication is ultimately small due to the high fidelity and proofreading abilities of polymerases. It is clear, therefore, that the lesion formed by parent metalloinsertors must be significantly potent such that even a small number of metalloinsertor-DNA

lesions can result in selective cell death. Moreover, despite their similar mismatch binding affinities, the **Rh−O** metalloinsertors are even more potent than parent metalloinsertors, and therefore these **Rh−O** metalloinsertors must produce a unique lesion structure at the mismatched site that can activate a response at even lower concentrations (and therefore fewer metalloinsertor-DNA lesions) than parent metalloinsertors.

Could the increase in potency be attributed to a difference in how these **Rh−O** metalloinsertors bind to DNA within the cell?[19] As discussed above, both the Δ- and Λ-enantiomers of $[Rh(phen)(chrysi)(PPO)]^{2+}$ can bind to DNA mismatches *in vitro* and selectively kill MMR-deficient cells in culture. This behavior is distinct from parent metalloinsertors, for which only the Δ-enantiomer can bind mismatches and produce biological effects.[15] The ability of both enantiomers of **Rh−O** metalloinsertors to bind mismatched DNA suggests the binding interaction must be fundamentally distinct from that of the parent metalloinsertors; these new **Rh−O** metalloinsertors must bind DNA in a way that can accommodate the Λ-enantiomer.

Furthermore, some evidence suggests that even the DNA-binding ability of the Δ-enantiomer may be altered in these **Rh−O** metalloinsertors. Previously, it was observed that bulky parent metalloinsertors, such as $[Rh(DIP)_2(chrysi)]^{3+}$, exhibited poor binding affinities ($10^4\ M^{-1}$) and could not easily be modeled to fit into a mismatched DNA lesion due to significant steric clashing between the DIP ligands and the DNA backbone.[21] In contrast, significant differences in ancillary ligand steric bulk have minimal effect on the binding affinities of **Rh−O** metalloinsertors, which all bind to DNA with micromolar affinity. Even the most sterically bulky complex, $[Rh(DIP)(chrysi)(PPO)]^{2+}$, has a

relatively high affinity for mismatched DNA (10^6 M^{-1}) despite containing the bulky DIP ligand. It therefore seems that the inclusion of the DIP ligand is not sufficient to preclude DNA binding, and perhaps this dramatic increase in binding affinity of a DIP-containing metalloinsertor may indicate that a new binding interaction exists that can accommodate the steric bulk of these **Rh−O** metalloinsertors.

Another consideration is the conformation of the chrysi ligand of these new **Rh−O** metalloinsertors. All **Rh−O** complexes have chrysi imine pK_a values above physiological pH, indicating that they remain protonated in the intracellular environment. This protonation results in steric clashing between the imine proton and an aromatic proton in the chrysi system and, as a result, the chrysi ligand becomes buckled relative to the rhodium center to relieve the steric strain.[19] This is in stark contrast to parent metalloinsertors which deprotonate at cellular pH and therefore do not exhibit steric clashing between the imine and aromatic protons. As a result, the chrysi ligand lays planar in these parent metalloinsertors. Distortion of the chrysi ligand, the ligand that interacts most intimately with the DNA, likely disrupts the overall metalloinsertor-DNA binding interaction, further suggesting there is likely a difference in how **Rh−O** and parent metalloinsertors bind to DNA.[19]

Lastly, the **Rh−O** complexes reported here are lipophilic (log P > 0), whereas comparable parent metalloinsertors are hydrophilic (log P < 0).[38] This change in lipophilicity could alter the way **Rh−O** complexes interact with the hydrophobic bases of DNA or even DNA-processing proteins that may be responsible for recognizing the DNA-metalloinsertor lesion. Overall, these results suggest that the **Rh−O** metalloinsertors interact with DNA differently than parent metalloinsertors. While these

complexes still appear to undergo metalloinsertion, as evidenced by their ability to bind mismatched DNA *in vitro* with high affinity, it is unclear how their binding might be distinct from parent metalloinsertors. It seems possible that a subtle difference in the extent or orientation of mismatched base ejection or in the unwinding of the DNA helix by the metalloinsertor could ultimately result in a difference in how that lesion is recognized or processed within the cell, which could lead to overall cellular response and increased potency. Crystallographic studies of **Rh−O** metalloinsertors with DNA are currently underway to investigate the potential difference between parent and **Rh−O** metalloinsertor binding. Attempts towards these crystallographic are detailed in Chapter 4 of this thesis.

2.5 Conclusions and Implications for Future Metalloinsertor Design

The $[Rh(L)(chrysi)(PPO)]^{2+}$ family of metalloinsertors described herein display biological selectivity and potency that are maintained across various ligand frameworks varying in size and lipophilicity. When compared with other **Rh−O** metalloinsertors in which the PPO-type ligand is varied, metalloinsertors containing the **Rh−O** motif are consistent in their biological selectivity (and, to a large extent, potency) for MMR-deficient cells regardless of significant alterations to their ancillary ligands. It has previously been shown that the metalloinsertors with DIP ligands and PPO-type ligands cannot be easily modeled into a mismatched DNA lesion due to steric clashes with the DNA structure.[19,21] Despite steric bulk, **Rh−O** metalloinsertors have comparable binding affinities to parent metalloinsertors and significantly improved biological activity. Furthermore, these complexes show little enantioselectivity; both isomers bind DNA and show high potency, further supporting that their metalloinsertion binding interaction

markedly differs from parent metalloinsertors. Taken together, these observations show that the **Rh−O** metalloinsertor framework has great potential for the design of new therapeutics and for the attachment of new payloads, while maintaining biological selectivity.[39–43] The consistently high potency and cell selectivity of these complexes is unique and provides the basis for new generations of metalloinsertors and metalloinsertor conjugates.

1.6 References

(1) Cheung-Ong, K.; Giaever, G.; Nislow, C. *Chem. Biol.* **2013**, *20*, 648–659.

(2) Wang, D.; Lippard, S. J. *Nat. Rev. Drug Discov.* **2005**, *4*, 307–320.

(3) Kelland, L. *Nat. Rev. Cancer* **2007**, *7*, 573–584.

(4) Nitiss, J. L. *Nat. Rev. Cancer* **2009**, *9*, 338–350.

(5) *DNA-targeting Molecules as Therapeutic Agents*, 2nd ed.; Waring, M. J., Ed.; Chemical Biology; The Royal Society of Chemistry, 2018.

(6) Shoshan, M. C.; Linder, S. *Expert Opin. Drug Metab. Toxicol.* **2008**, *4*, 273–280.

(7) Tham, K. C.; Kanaar, R.; Lebbink, J. H. G. *DNA Repair (Amst).* **2016**, *38*, 75–83.

(8) Arzimanoglou, I. I.; Gilbert, F.; Barber, H. R. K. *Cancer* **1998**, *82*, 1808–1820.

(9) Pino, M. S.; Mino-Kenudson, M.; Wildemore, B. M.; Ganguly, A.; Batten, J.; Sperduti, I.; Iafrate, A. J.; Chung, D. C. *J. Mol. Diagnostics* **2009**, *11*, 238–247.

(10) (a) Jackson, B. A.; Barton, J. K. *J. Am. Chem. Soc.* **1997**, *119*, 12986–12987. (b) Jackson, B. A.; Barton, *Biochemistry* **2000**, *39*, 6176–6182

(11) Zeglis, B. M.; Boland, J. A.; Barton, J. K. *J. Am. Chem. Soc.* **2008**, *130*, 7530–7531.

(12) Jackson, B. A.; Alekseyev, V. Y.; Barton, J. K. *Biochemistry* **1999**, *38*, 4655–4662.

(13) Cordier, C.; Pierre, V. C.; Barton, J. K. *J. Am. Chem. Soc.* **2007**, *129*, 12287–12295.

(14) (a) Pierre, V. C.; Kaiser, J. T.; Barton, J. K. *Proc. Natl. Acad. Sci.* **2007**, *104*, 429–434; (b) Zeglis, B.M.; Pierre, V.C.; Kaiser, J.T.; Barton, J.K. *Biochem.* **2009**, *48*, 4247-4253.

(15) Hart, J. R.; Glebov, O.; Ernst, R. J.; Kirsch, I. R.; Barton, J. K. *Proc. Natl. Acad. Sci.* **2006**, *103*, 15359–15363.

(16) Bailis, J. M.; Gordon, M. L.; Gurgel, J. L.; Komor, A. C.; Barton, J. K.; Kirsch, I. R. *PLoS One* **2013**, *8*, e78726.

(17) Fink, D.; Nebel, S.; Aebi, S.; Zheng, H.; Cenm, B.; Nehmã, A.; Christen, D.; Howell, S. B. *Cancer Res.* **1996**, *56*, 4881–4886.

(18) Fink, D.; Nebel, S.; Norris, P. S.; Aebi, S.; Kim, H. K.; Haas, M.; Howell, S. B. *Br. J. Cancer* **1998**, *77*, 703–708.

(19) Komor, A. C.; Barton, J. K. *J. Am. Chem. Soc.* **2014**, *136*, 14160–14172.

(20) Komor, A. C.; Schneider, C. J.; Weidmann, A. G.; Barton, J. K. *J. Am. Chem. Soc.* **2012**, *134*, 19223–19233.

(21) Ernst, R. J.; Song, H.; Barton, J. K. *J. Am. Chem. Soc.* **2009**, *131*, 2359–2366.

(22) Zeglis, B. M.; Barton, J. K. *Nat. Protoc.* **2007**, *2*, 357–371.

(23) Lee, J. R.; Lung, J. W. *J. Chinese Chem. Soc.* **2003**, *50*, 227–232.

(24) Sangster, J. Octanol-Water Partition Coefficients of Simple Organic Compounds. *Journal of Physical and Chemical Reference Data*, 1989, *18*, 1111–1229.

(25) Komor, A. C.; Schneider, C. J.; Weidmann, A. G.; Barton, J. K. *J. Am. Chem. Soc.* **2012**, *134*, 19223–19233.

(26) Ahmad, K. A.; Iskandar, K. B.; Hirpara, J. L.; Clement, M. V.; Pervaiz, S. *Cancer Res.* **2004**, *64*, 7867–7878.

(27) Puckett, C. A.; Barton, J. K. *Biochemistry* **2008**, *47*, 11711–11716.

(28) Sitlani, A.; Long, E. C.; Pyle, A. M.; Barton, J. K. *J. Am. Chem. Soc.* **1992**, *114*, 2303–2312.

(29) Bailis, J. M.; Weidmann, A. G.; Mariano, N. F.; Barton, J. K. *Proc. Natl. Acad. Sci.* **2017**, *114*, 6948–6953.

(30) Reithofer, M. R.; Bytzek, A. K.; Valiahdi, S. M.; Kowol, C. R.; Groessl, M.; Hartinger, C. G.; Jakupec, M. A.; Galanski, M.; Keppler, B. K. *J. Inorg. Biochem.* **2011**, *105*, 46–51.

(31) Waring, M. J.; Johnstone, C. *Bioorganic Med. Chem. Lett.* **2007**, *17*, 1759–1764.

(32) Landero Figueroa, J. A.; Stiner, C. A.; Radzyukevich, T. L.; Heiny, J. A. *Sci. Rep.* **2016**, *6*, 20551.

(33) Liu, X.; Testa, B.; Fahr, A. *Pharm. Res.* **2011**, *28*, 962–977.

(34) Hart, J. R.; Glebov, O.; Ernst, R. J.; Kirsch, I. R.; Barton, J. K. *Proc. Natl. Acad. Sci.* **2006**, *103*, 15359–15363.

(35) Koi, M.; Umar, A.; Chauhan, D. P.; Cherian, S. P.; Carethers, J. M.; Kunkel, T. A.; Boland, C. R. *Cancer Res.* **1994**, *54*, 4308–4312.

(36) Glaab, W. E.; Tindall, K. R. *Carcinogenesis* **1997**, *18*, 1–8.

(37) Modica-Napolitano, J. S.; Aprille, J. R. *Adv. Drug Deliv. Rev.* **2001**, *49*, 63–70.

(38) Weidmann, A. G.; Komor, A. C.; Barton, J. K. *Philisophocal Trans. R. Soc.* **2013**, *371*, 20120117.

(39) Weidmann, A. G.; Barton, J. K. *Inorg. Chem.* **2015**, *54*, 9626–9636.

(40) Petitjean, A.; Barton, J. K. *J. Am. Chem. Soc.* **2004**, *126*, 14728–14729.

(41) Chari, R. V. J. *Acc. Chem. Res.* **2008**, *41*, 98–107.

(42) Zeglis, B. M.; Barton, J. K. *J. Am. Chem. Soc.* **2006**, *128*, 5654–5655.

(43) Nano, A.; Boynton, A. N.; Barton, J. K. *J. Am. Chem. Soc.* **2017**, *139*, 17301–17304.

Chapter 3

TARGETING DNA: MISMATCH-MEDIATED CELL DEATH RENDERS A RHODIUM METALLOINSERTOR MORE POTENT THAN CISPLATIN*

3.1 Introduction

Colorectal cancer (CRC) is a diverse set of diseases that affects millions of men and women during their lifetimes.[1] Recently, many researchers have attempted to identify different subtypes of colorectal cancer that are defined by common mutations or aberrations in gene, mRNA, and protein expression levels.[2] One such subtype of colorectal cancer is defined by microsatellite instabilities (MSI), a defect caused by malfunctioning or absent mismatch repair (MMR) machinery. MMR-deficient tumors represent over 14% of all colorectal cancer cases, as well as up to 20% of all solid tumors.[2,3] MMR machinery comprises a tetramer of proteins that are responsible for identifying and correcting mismatches and indels (insertions and deletions) that occur during replication.[4] In healthy tissues, MMR machinery corrects these lesions with high efficiency, but in cancer cells that are MMR deficient, these lesions remain uncorrected and ultimately propagate into mutations. The high mutational load of these cancers has been targeted by the immunotherapeutic pembrolizumab, a programmed death 1 (PD-1) inhibitor that was recently FDA approved for MSI-high tumors.[5] However, the abundance of transient DNA base pair mismatches and indels serves as another possible

---

* Adapted from Boyle, K. M.; Nano, A.; Day, C.; Barton, J. K. Cellular Target of a Rhodium Metalloinsertor is the DNA Mismatch, **2018**, *Submitted.* K.M.B designed experiments and performed cytotoxicity and whole cell uptake experiments and wrote the majority of the text. A.N. designed and performed fluorescence titration experiments and wrote the experimental methods for fluorescence experiments. C.D. assisted in troubleshooting and performing cytotoxicity experiments.

target for MSI tumors that has yet to be utilized in a clinical setting. Furthermore, these lesions could serve as a target for direct detection and diagnosis of MMR deficiencies in tumors, something that is commonly measured indirectly through tests of mutational frequency instead of number of mismatches.[6] Such a diagnostic would further support the promise of a mismatch- and indel-targeted therapeutic agent.

To address these needs, our group has developed a unique family of metal complexes called rhodium metalloinsertors. Rhodium metalloinsertors selectively target thermodynamically destabilized regions of DNA, such as base pair mismatches, abasic sites, and single base bulges (a type of indel), making these complexes ideal candidates for targeting and detecting the DNA lesions found in MMR-deficient tumors (**Figure 3.1**).[7–9] Rhodium metalloinsertors achieve this selective binding through a sterically expansive aromatic 5,6-chrysenequinone diimine (chrysi) ligand. In this DNA-binding mode, termed metalloinsertion, the rhodium complex binds the mismatched DNA from the minor groove, inserts the chrysi ligand into the DNA base-stack, ejects the mismatched bases, and π-stacks with the flanking well-matched base pairs. This binding mode has been confirmed through crystallographic and NMR solution studies, and the properties of these DNA-binding complexes have been rigorously studied *in vitro*: we have observed that this binding interaction correlates with the thermodynamic destabilization of a DNA lesion, making it a general binding mode capable of targeting over 80% of all DNA base pair mismatches regardless of sequence context, as well as abasic sites and single base bulges.[7,8,10] Furthermore, this targeting occurs with over 1000:1 selectivity for mismatches over well-matched base pairs and micromolar binding

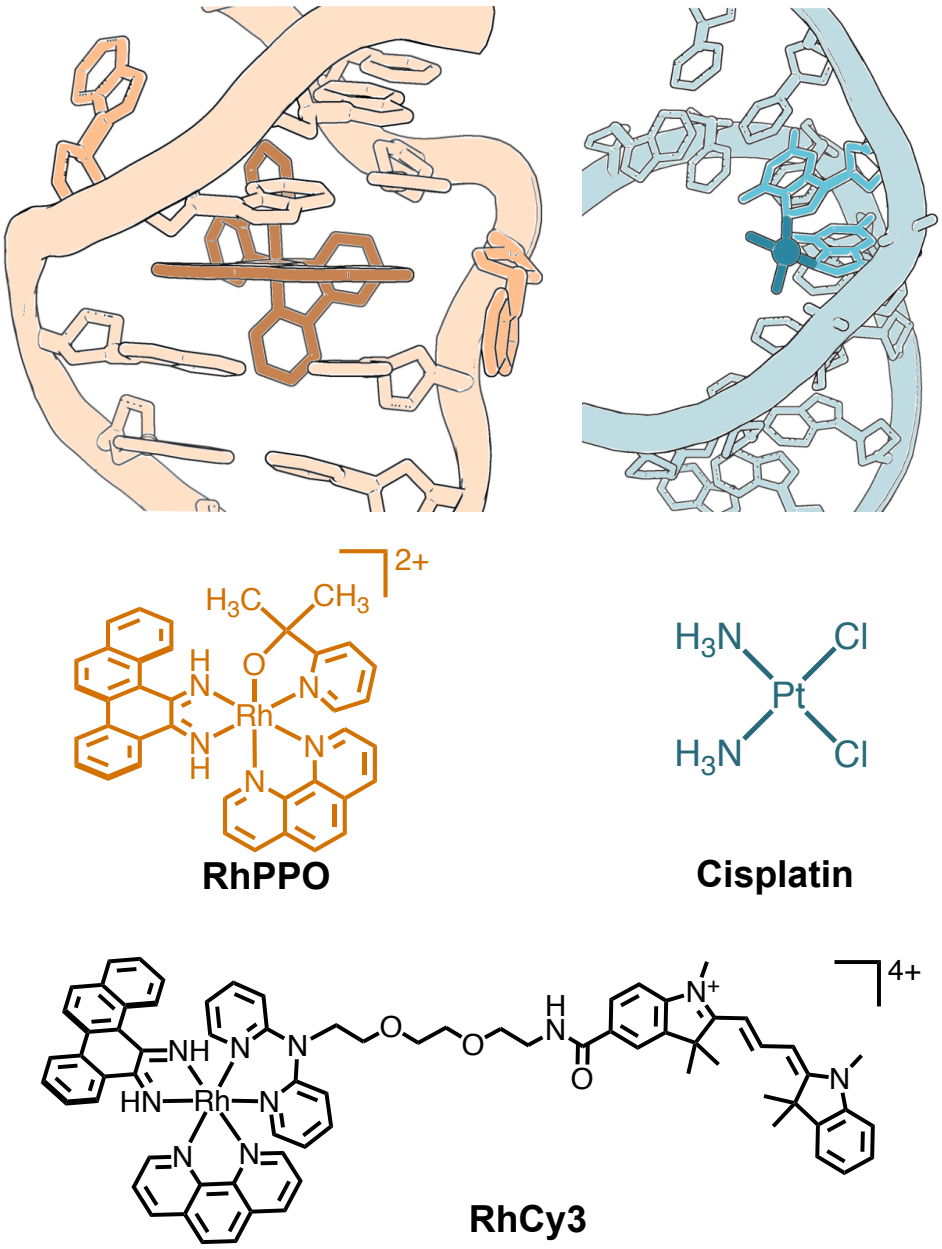

Figure 3.1 The binding and structure of a metalloinsertor and cisplatin. As observed crystallographically in previous studies, a classic metalloinsertor binds selectively to a mismatch in DNA (top left, PDB 3GSK), while cisplatin binds to a d(GpG) site in DNA (top right, PDB 1AIO). The structures of $[Rh(phen)(chrysi)(PPO)]^{2+}$ (middle left), cisplatin (middle right), and RhCy3 (bottom).

affinities, further supporting its potential as a selective therapeutic agent capable of targeting of mismatches and other lesions inside of MMR-deficient cancer cells.

Rhodium metalloinsertors have been rigorously studied in several pairs of matched cancer cell lines which differ primarily in the presence or absence of functioning MMR machinery: a pair of $MLH1^+$ and $MLH1^-$ colorectal cancer cell lines derived from a common parent cell line, mouse fibroblast cells derived from $MSH2^+$ and $MSH2^-$ litter mates, and an inducible lung cancer cell line that is $MLH1^+$ or $MLH1^-$ in the absence or presence (respectively) of a doxycycline inducer.[11,12] In every matched pairing, metalloinsertors are significantly more cytotoxic towards the MMR-deficient cell line compared to their MMR-proficient counterpart (a feature we refer to as selectivity). These results demonstrate that rhodium metalloinsertors can target MMR deficiencies in a complex cellular context, however they do not prove the specific cellular target of metalloinsertors to be DNA mismatches. Furthermore, these cell pairings are not reflective of the diversity of clinical colorectal cancer (CRC) cases; in reality, the differences between tumors in two different patients or healthy and cancerous tissues in a single patient will be far greater than just the presence or absence of a single MMR protein.[13,14] While many colorectal cancer patients do exhibit tumors with MSI, there can be countless differences in mutations and expression profiles of other genes, proteins, and mRNAs that make each individual tumor a unique therapeutic challenge, and it is possible that these additional variables may complicate the selective mismatch targeting of metalloinsertors in cells. As such, to better anticipate and understand the potential clinical challenges of rhodium metalloinsertors, it is imperative to study molecularly distinct colorectal cancer cell lines that are derived from different patients.

To understand more fully the potential clinical applicability of rhodium metalloinsertors, we examined our most potent and selective metalloinsertor, $[Rh(phen)(chrysi)(PPO)]^{2+}$ (**Figure 3.1**), across 27 CRC cell lines (**Table 3.1**).[15] These cell lines are derived from 24 unique patients and represent a diverse set of tumors, spanning the four subtypes of CRC and both MMR-deficient and MMR-proficient phenotypes.[16,17] Here, the toxicities of $[Rh(phen)(chrysi)(PPO)]^{2+}$ were compared to cisplatin, an FDA approved chemotherapeutic agent, in this cell line panel using a luciferase-based luminescence assay which measures ATP from living cells. We further examined the influence that cellular uptake and number of genomic DNA lesions (as measured by the rhodium metalloinsertor-cyanine dye conjugate RhCy3) could have on the cytotoxicity of $[Rh(phen)(chrysi)(PPO)]^{2+}$ across different cell lines.

3.2 Experimental Procedures

3.2.1 Materials

All commercially available reagents were used as received. The metalloinsertors $[Rh(phen)(chrysi)(PPO)]^{2+}$ and RhCy3 were synthesized and purified following published protocols.[18,19] All experiments were performed with the chloride salt of these metalloinsertors. Cell culture media, supplements, and PureLink™ Genomic DNA Mini Kits were purchased from Life Technologies (Carlsbad, CA). CellTiter-Glo® Luminescent Cell Viability Assay kits were purchased from Promega (Madison, WI). BCA Protein Assay Kits were purchased from Pierce (Waltham, MA). Cell lines used in the experiment were purchased from ATCC (Manassas,VA) or provided by collaborators at AMGEN (Thousand Oaks, CA).

Table 3.1 List of cell lines used in this experiment with origin and growth conditions.

Cell Line	Obtained from	Type of Media	% FBS	Media Supplements
CaCo2 [a,b]	AMGEN	DMEM	20	100 U/mL PenStrep
Colo205 [a,b]	AMGEN	RPMI 1640	10	100 U/mL PenStrep
Colo320DM [a]	AMGEN	RPMI 1640	10	100 U/mL PenStrep
Colo678 [a,b]	AMGEN	DMEM	10	100 U/mL PenStrep
CW2 [a,b]	AMGEN	DMEM	10	100 U/mL PenStrep
DLD-1 [a,b,c,d]	AMGEN	RPMI 1640	10	100 U/mL PenStrep
HCC2998 [a,b]	AMGEN	RPMI 1640	10	100 U/mL PenStrep
HCT116 [a,b,c]	AMGEN	McCoy's 5A	10	100 U/mL PenStrep
HCT15 [a,b,d]	AMGEN	RPMI 1640	10	100 U/mL PenStrep
HT29 [a,b,d]	AMGEN	McCoy's 5A	10	100 U/mL PenStrep
KM12 [a]	AMGEN	RPMI 1640	10	100 U/mL PenStrep
LoVo [a]	AMGEN	Ham's F-12K	10	100 U/mL PenStrep
Ls1034 [a,b]	AMGEN	RPMI 1640	10	100 U/mL PenStrep
Ls123 [a,b]	AMGEN	DMEM	10	100 U/mL PenStrep
Ls174T [a,b]	AMGEN	DMEM	10	100 U/mL PenStrep
NCI-H716 [a,b]	AMGEN	RPMI 1640	10	100 U/mL PenStrep
NCI-H508 [a]	AMGEN	RPMI 1640	10	100 U/mL PenStrep, 2 mM GlutaMAX
RKO [a,b]	AMGEN	DMEM	10	100 U/mL PenStrep
SW1116 [a,b]	AMGEN	RPMI 1640	10	100 U/mL PenStrep
SW1463 [a]	AMGEN	RPMI 1640	10	100 U/mL PenStrep
SW403 [a,b]	AMGEN	RPMI 1640	10	100 U/mL PenStrep, 2 mM GlutaMAX
SW48 [a,b]	AMGEN	RPMI 1640	10	100 U/mL PenStrep
SW480 [a,d]	AMGEN	RPMI 1640	10	100 U/mL PenStrep
SW620 [a,b,d]	AMGEN	RPMI 1640	10	100 U/mL PenStrep
SW837 [a]	AMGEN	RPMI 1640	10	100 U/mL PenStrep
SW948 [a,b]	ATCC	RPMI 1640	10	100 U/mL PenStrep, 2 mM GlutaMAX
WiDr [a,b,d]	AMGEN	DMEM	10	100 U/mL PenStrep
AN3-CA [c]	AMGEN	DMEM	10	100 U/mL PenStrep
DU-145 [c]	ATCC	DMEM	10	100 U/mL PenStrep
HCT-116N [c]	--	RPMI 1640	10	100 U/mL PenStrep, 2 mM L-glutamine, 0.1 mM non-essential amino acids, 1 mM sodium pyruvate, 400 ug/mL Geneticin (G418)
HCT-116O [c]	--	RPMI 1640	10	100 U/mL PenStrep, 2 mM L-glutamine, 0.1 mM non-essential amino acids, 1 mM sodium pyruvate, 400 ug/mL Geneticin (G418)
HEC-1-A [c]	ATCC	McCoy's 5A	10	100 U/mL PenStrep

[a] Cell lines used in cytotoxicity assay
[b] Cell lines used in whole cell uptake assay
[c] Cell lines used in RhCy3 fluorescence assay
[d] DLD-1/HCT15, HT29/WiDr, SW480/SW620 pairings are derived from a common patient.

3.2.2 Cell Culture

The specific growth conditions of each cell line, including the type of medium and added supplements, can be found in **Table 3.1**. In general, cell lines were grown in RPMI 1640, DMEM, McCoy's 5A, or Ham's F-12K media supplemented with 10% FBS (20% FBS for the cell line CaCo2), 100 units/mL penicillin, 100 units/mL streptomycin. Cells were grown in tissue culture treated flasks at 37 °C under a humidified 5% CO_2 atmosphere.

3.2.3 CellTiter-Glo Viability Assay of Metalloinsertors and Cisplatin

CellTiter-Glo Luminescent Cell Viability Assays were performed following the protocols provided in the kit. Briefly, cell lines were plated at a density of 10,000 cells in 100 μL media per well in an opaque, tissue culture treated 96-well plate and allowed to adhere for 24 h. One of two compounds, $[Rh(phen)(chrysi)(PPO)]^{2+}$ or cisplatin, was added to each well at a final concentration of 0-150 μM, and the cells were allowed to incubate with the therapeutic for 72 h. After incubation with a therapeutic agent, the cell solutions were treated with an equal volume of the CellTiter Glo reagent, which contains beetle luciferin and a recombinant luciferase. The luciferase can catalyze a reaction between the luciferin and ATP provided by viable cells to produce a luminescence that is proportional to the number of viable cells. Luminescence was recorded on a FlexStation 3 Multi-Mode Plate Reader with integration time of 0.500 seconds. Percent viability was determined by the ratio of the luminescence of therapeutic-treated cells compared to untreated cells. IC50 values were determined by fitting the cell viability curve to a sigmoidal curve in OriginPro v 8.5 and using the resultant parameters to calculate the concentration at which 50% of cells were viable. Each therapeutic dose was performed in

triplicate and each experiment was repeated 2-3 times to confirm reproducible viability curves. For statistical analyses, cell lines from a common patient (DLD-1/HCT15, HT29/WiDr, SW480/SW620) were averaged and counted as a single cell line to avoid double-counting cancer from a single patient, as the IC50 values of these pairs were unsurprisingly similar.

3.2.4 Exploration of Other Viability Assays

Several different viability assays were attempted to determine the best viability assay for the experiment described in this chapter. Ultimately, the CellTiter-Glo assay was selected as the most fit assays for our purposes, but the other attempted assays are described below. Additionally, preliminary experiments using etoposide (a DNA intercalator) and MNNG (a DNA alkylating agent) were performed using the resazurin reductase assay, but ultimately cisplatin was selected as the most interesting control compound for these experiments due to its high clinical use, its resistance profile towards MMR-deficient cancers, and its inorganic nature.

3.2.4.1 MTT Cytotoxicity Assay

MTT Cytotoxicity Assays were performed following the protocols provided in the kit. Briefly, cell lines were plated at a density of 10,000 cells in 100 μL media per well in clear plastic tissue culture treated 96-well plate. Immediately following plating, $[Rh(phen)(chrysi)(PPO)]^{2+}$ was added to each well at a final concentration of 0-40 μM, and the cells were allowed to incubate with the metalloinsertor for 72 h. After incubation, 10 μL of MTT reagent (2-(4,5-dimethylthiazol-2-yl)-2,5-diphenyltatrazolium bromide) was added to each well and incubated at 37 °C for four h. MTT can be converted to a purple complex, formazan, in metabolically activity. The formazan crystals were

solubilized and quantified by absorbance at 570 nm (background subtracted at 690 nm). Viability was determined for each metalloinsertor concentration through comparison to untreated cells. A derivative of the MTT assay was also attempted in which after incubation with the MTT reagent the media was removed and replaced with DMSO, which more sufficiently dissolves the formazan crystals.

3.2.4.2 Nuclear Count Assay

The nuclear count assay was performed following procedures provided by a collaborator. 1000 to 5000 cells of HCT116N, HCT116O, or DLD-1 were plated in 100 μL into each well of a black-walled, clear bottom, tissue culture treated 96-well plate. The plate was incubated overnight to allow the cells to adhere to the plate. The following day, the HCT116N and HCT116O cells were treated to a final concentration of 0-1 μM $Rh(phen)(chrysi)(PPO)]^{2+}$ and the DLD-1 cells were treated to a final concentration of 0-10 μM $[Rh(phen)(chrysi)(PPO)]^{2+}$. The cells were allowed to incubate with the metalloinsertor for up to 72 h. After incubation, the cells were treated with either a Hoechst-based protocol or a DAPI-based nuclear staining protocol, described below. Hoechst and DAPI are fluorescent molecules that bind non-covalently to DNA. Each well of a 96-well plate can be imaged and the fluorescent nuclear spots can be counted to determine the viability of cells treated with the metalloinsertor relative to an untreated control.

Hoechst Protocol: After metalloinsertor incubation, media was removed from each plate by gently dumping the solution over paper towels (plates were not tapped or vigorously shaken). 50 μL of a solution containing 0.25% formaldehyde, 0.1% saponin, and 2 μg/mL Hoechst dye was added to each well. Plates were then incubated at 37 °C

for 30 min. After incubation, plates were gently washed with 100 μL PBS (phosphate buffered saline) 3 times. PBS was removed by gentle dumping over paper towels. Finally 100 μL of PBS was added to each plate. The plate was sealed with clear packing tape and the lids were made opaque using duct tape. The samples were kept in the dark in the fridge (4 °C) overnight before being delivered to collaborators at City of Hope, where they were kept at 4 °C until being examined on a Molecular Devices ImageXpress high-content screening system. It is of note that many cells were lost in the rinsing procedures using this staining method, likely due to the low concentration of paraformaldehyde used. As such, the DAPI staining protocol was used for the majority of the NC experiments performed.

DAPI Protocol: After metalloinsertor incubation, media was removed from each plate by gently dumping the solution over paper towels (plates were not tapped or vigorously shaken). 50 μL of 4% formaldehyde in water was added to each well and the plates were allowed to incubate at room temperature for 20 min. The formaldehyde was removed and replaced with 50 μL of 0.5% triton-X. The plates again sat at room temperature for 15-20 min. Finally, triton-X was removed and the cells were incubated in the dark with 50 μL per well of a 2 μg/mL DAPI solution for 30 min. After incubation, excess stain was removed by gently washing the cells with 100 μL PBS 3 times. PBS was removed by gentle dumping over paper towels. Finally 100 μL of PBS was added to each plate. The plate was sealed with clear packing tape and the lids were made opaque using duct tape. The samples were kept in the dark in the fridge (4 °C) overnight before being delivered to collaborators at City of Hope, where they were kept at 4 °C until being examined on a Molecular Devices ImageXpress high-content screening system.

3.2.4.3 Resazurin Reduction Assay

The resazurin reduction assay was performed following the literature.[20] Briefly, cells were plated in an opaque-walled, clear bottomed, tissue culture treated 96-well plate at 10,000 cells/well. HCT116N, HCT116O, and DLD-1 cells were incubated with various concentrations of $[Rh(phen)(chrysi)(PPO)]^{2+}$. HCT116N and HCT116O cells were treated to a final concentration of 0-1 μM metalloinsertor. DLD-1 cells were treated to a final concentration of 0-15 μM metalloinsertor. The cells were allowed to incubate with the metalloinsertor for 72 h. After incubation, the plate was centrifuged for 10 min at 230 g (~1100 rpm) to concentrate the cells to the bottom of the plate. Cell media was then removed be either multichannel pipette or gentle tapping onto paper towels. The resazurin reagent was prepared from solid powder to create a 0.025 mg/mL solution in PBS and 100 μL was added to each well. The cells were then re-incubated for 4 h at 37 °C. During this time, resazurin (blue) can be metabolized by viable cells to produce resorufin (pink). Absorbance and emission can both be used as readouts of this assay. As such, absorbance was measured at 570 nm (with reference wavelength of 630 nm). For emissions, the samples were excited at 560 nm and emission at 590 nm was recorded. Viability was determined for each metalloinsertor concentration through comparison to untreated cells

This method is comparable to the MTT assay (both use metabolic activity to produce a signal change) and is significantly cheaper to use, therefore this assay was used in preliminary experiments with cisplatin (a covalent DNA binder), etoposide (a DNA intercalator), and MNNG (a DNA alkylating agent) to assess a reasonable concentration range for each drug before assessing them using the more expensive CellTiter-Glo assay.

3.2.4.4 Sulforhodamine B Assay

The Sulforhodamine B assay was performed following the literature.[20,21] Briefly, cells were plated in an opaque-walled, clear bottom tissue culture treated 96-well plate at 10,000 cells/well. HCT116N, HCT116O, and DLD-1 cells were incubated with various concentrations of $[Rh(phen)(chrysi)(PPO)]Cl_2$. HCT116N and HCT116O cells were treated to a final concentration of 0-1 μM metalloinsertor. DLD-1 cells were treated to a final concentration of 0-15 μM. The cells were allowed to incubate with the metalloinsertor for 72 h. At this point, a 20% w/v solution of trichloroacetic acid was chilled on ice and 50 μL was added to each well to fix the cells. The plate was then stored in the refrigerator for 1 hour to allow the cells to be fixed. Following this, the TCA/media was removed with gentle tapping, and then washed with running tap water 4 times, patted dry on paper towels, and allowed to air dry for 1 h. Once dry, a 0.057% w/v solution of sulforhodamine B in 1% acetic acid was prepared from solid and 100 μL was added to each well. The cells were incubated at room temperature for 30 min to allow the dye to bind to proteins that have been fixed to the tissue culture flask, and excess sulforhodamine B was then rinsed away with 4 aliquots of acetic acid. The plates were again allowed to dry for 30 min before 200 μL of TRIS buffer (10 mM, pH 10.5) was added to each well to redissolve the sulforhodamine dye. The plates were then shaken for 30 min to dissolve the stain and absorbance was measured at 540 nm with a reference of 630 nm. Viability was determined for each metalloinsertor concentration through comparison to untreated cells.

3.2.4.5 Neutral Red Viability Assays

The Sulforhodamine B assay was performed following the literature.[20,22] Briefly, cells were plated in an opaque-walled, clear bottom tissue culture treated 96-well plate at 10,000 cells/well. HCT116N, HCT116O, and DLD-1 cells were incubated with various concentrations of $[Rh(phen)(chrysi)(PPO)]^{2+}$. HCT116N and HCT116O cells were treated to a final concentration of 0-1 μM metalloinsertor. DLD-1 cells were treated to a final concentration of 0-15 μM. The cells were allowed to incubate with the metalloinsertor for 72 h. Prior to dye incubation, a 0.04 mg/mL solution of neutral red was made in cell media and pre-heated in the 37 °C incubator for 2 h. The neutral red solution was centrifuged at 1800 rpm to pellet any undissolved dye crystals. Media was removed from the 96-well plate by gentle tapping, then 100 μL of neutral red was added to each well. The cells were incubated for 3 h at 37 °C to allow for uptake of the dye into the lysosomes of viable cells. There did not appear to be any dye crystallization over this time period. Excess neutral red media was removed by tapping and the cells were washed with 150 μL of PBS three times before 100 μL of destain solution (50:49:1 ethanol:water:acetic acid) was added to each well. The plate was shaken for 10 min to extract the neutral red. The absorbance of the plate was measured at 540 nm. An additional fluorescence measurement was taken with excitation of 530 nm and emission of 645 nm. Viability was determined for each metalloinsertor concentration through comparison to untreated cells.

3.2.5 ICP-MS Assay for Whole Cell Uptake of $[Rh(phen)(chrysi)(PPO)]^{2+}$

Whole cell uptake experiments were performed following previously published protocols with slight modifications.[23] Briefly, cells were plated at a density of 1,000,000

cells in 3 mL media per well in a 6-well plate and allowed to adhere for 24 h. Cells were then treated with $[Rh(phen)(chrysi)(PPO)]^{2+}$ to a final concentration of 0.5 μM. For adherent cell lines, the rhodium-containing medium was aspirated from each well after 24 h and each well was washed 2x with 1 mL of PBS then harvested by trypsinization and transferred to centrifuge tubes. For mixed or suspended cell lines, the rhodium-containing medium was transferred to a centrifuge tube before the PBS rinses and trypsinization. Harvested cells were centrifuged at 1500 rpm for 5 minutes. The supernatant was decanted and the cell pellet was suspended in 1 mL PBS. Centrifugation and PBS washing was repeated three times total. For suspension cell lines (mixed or complete), the suspended and trypsinized aliquots were combined during the second wash. An aliquot from the final suspension was reserved and analyzed for protein content using a Pierce BCA Protein Assay Kit following the manufacturers instructions. To lyse the cells and destroy membrane integrity, each cell suspension was sonicated for 20 s at 40% amplitude with a Qsonica Ultrasonic sonicator, then frozen and lyophilized for 72 h. The resulting cell particulate was suspending in 1 mL of 6% nitric acid and heated at 110 °C for 8 h to facilitate total digestion prior to ICP-MS analysis. Each sample was then diluted to 2% nitric acid and centrifuged to separate any undigested cell components. The solutions were analyzed for Rh content on an Agilent 8800 Triple Quadrupole ICP-MS. The concentration of Rh in each sample was determined by comparison to a standard curve ranging from 0.01 to 100 ppb. Rh concentrations were normalized to the protein content of each sample determined by BCA assay. The measurements were repeated two times using two biological replicates for each cancer cell line.

3.2.6 Genomic DNA Extraction and Purification

The genomic DNA was extracted and purified using PureLink® Genomic DNA Kits following the manufacturer's protocol. Prior to DNA extraction, the cells subjected to genomic DNA (gDNA) extraction were seeded and grown in their respective cellular medium (**Table 3.1**) to near confluence. Lysates were prepared by removing the growth medium from cells, then cells were harvested by trypsinization then re-suspended in 200 µL PBS. ProteinaseK (20 µL) and RNase (20 µL) were added to the sample, mixed by vortexing and incubated at room temperature for 2 min. 200 µL of PureLink® Genomic Lysis/Binding Buffer were added, mixed and vortexed to obtain a homogenous solution. The samples were incubated at 55 °C for 10 min to promote digestion then 200 µL of 96-100% ethanol was added to the lysate which was further mixed by vortexing for 5 s. The DNA was washed by adding 500 µL of Wash Buffer 1 then Wash Buffer 2 provided by the kit, followed by DNA eluting process using the spin columns. The spin columns were eluted with sterile MilliQ water (200 µl) two times to recover the gDNA. The samples were lyophilized and the dry DNA was solubilized in Tris buffer solution (5 mM Tris, 50 mM NaCl, pH = 8.0) in order to obtain a highly concentrated solution. The purity and concentration of the gDNA solutions were determined using a NanoDrop 2000 Spectrophotometer. The concentrations of the stock solutions of gDNA used during the fluorescence titrations were adjusted at 3140 ng/µl (4.7 mM base pairs DNA) in Tris buffer (200 mM NaCl, 5 mM Tris, pH 8.1).

3.2.7 Fluorescence Titrations with Genomic DNA

Fluorescence titrations were performed following the literature.[19] Luminescence spectra were recorded using a QE Pro High Performance Spectrometer with a back-

thinned, TE-cooled CCD detector controlled by the OceanView data acquisition and Ocean Optics analysis software package. Sample excitation was provided by a 455 nm LED. The fluorescence titrations in this study were performed with genomic DNA extracted from eight cancer cell lines characterized by different phenotypes (HCT116N, HCT116O, HCT116, DLD-1, HEC-1A, SW480, AN3-CA, DU-145). The emission spectra were recorded in Tris buffer solution (5 mM Tris, 200 mM NaCl, pH = 7.4) at 25 °C using a water circulation system. Excitation wavelength was λ_{Ex} = 455 nm and emission integral was reported after each addition of genomic DNA, as a scalar function from 548 to 675 nm. The measurements were repeated three times using three biological replicates for each cancer cell line.

3.2.8 Literature Analysis of Colorectal Cancer Cell Lines

Recently, many researchers, including Berg *et al.* and Linnekamp *et al.*, have explored the genetic and epigenetic features of colorectal cancer cell lines and provided rich repositories of information for other researchers to utilize.[16,17] As such, we attempted to identify correlations between the IC50 of [Rh(phen)(chrysi)(PPO)]Cl_2 and common genetic and epigenetic aberrations observed in colorectal cancer cell lines, including consensus molecular subtype (CMS), CpG island methylator phenotype (CIMP), and mutations in TP53, KRAS, BRAF, PIK3CA, and PTEN.

3.3 Results

3.3.1 Determining an Appropriate Viability Assay

The Barton group has traditionally only utilized the HCT116N and HCT116O cell lines in the majority of their experiments on new metalloinsertor complexes. MTT viability assays have worked consistently well in these experiments; therefore we initially

examined the cytotoxicity of $[Rh(phen)(chrysi)(PPO)]^{2+}$ in our diverse cell lines using the MTT assay. It was observed that several of these cell lines did not reach near-0% viability, instead they leveled off at 20-40% viability even at high metalloinsertor concentrations (> 40 μM, **Figure 3.2**). Indeed, it has been reported that the MTT assay, though widely used to measure cytotoxicity, is not always the most reliable or straightforward assay.[20] Additionally, since the MTT assay measures mitochondrial activity, it is possible that senescent cells that are no longer viable would still register as viable. As such, a variety of viability assays were performed to identify a suitable viability measure for the experiments described herein. These assays include the resazurin reduction assay (RES), the sulforhodamine B assay (SRB), the neutral red uptake assay (NRU), and the nuclear count assay (NC). Each assay was performed on HCT116N and HCT116O cells as well-studied controls and on the cell line DLD-1, which only reached 40% viability in MTT assays, even at high concentrations. RES, SRB, and NRU assays produced similar outcomes to the MTT assay, with DLD-1 never reaching near-0% viability (**Figure 3.3**). It is of note that the RES assay is significantly cheaper and simpler than the MTT assay, therefore it was used to pre-screen drug concentration ranges of cisplatin, etoposide, MNNG, and $[Rh(phen)(chrysi)(PPO)]^{2+}$. These results are summarized in **Figure 3.4**, however only cisplatin was studied in full as a control due to its high clinical use, its resistance profile towards MMR-deficient cancers, and its inorganic nature.

The NC assay provided very promising results in published metalloinsertor experiments, and was therefore initially used in these experiments.[24] Indeed, cell lines that were not able to reach near-0% viability in the MTT assay were able to reach ~10%

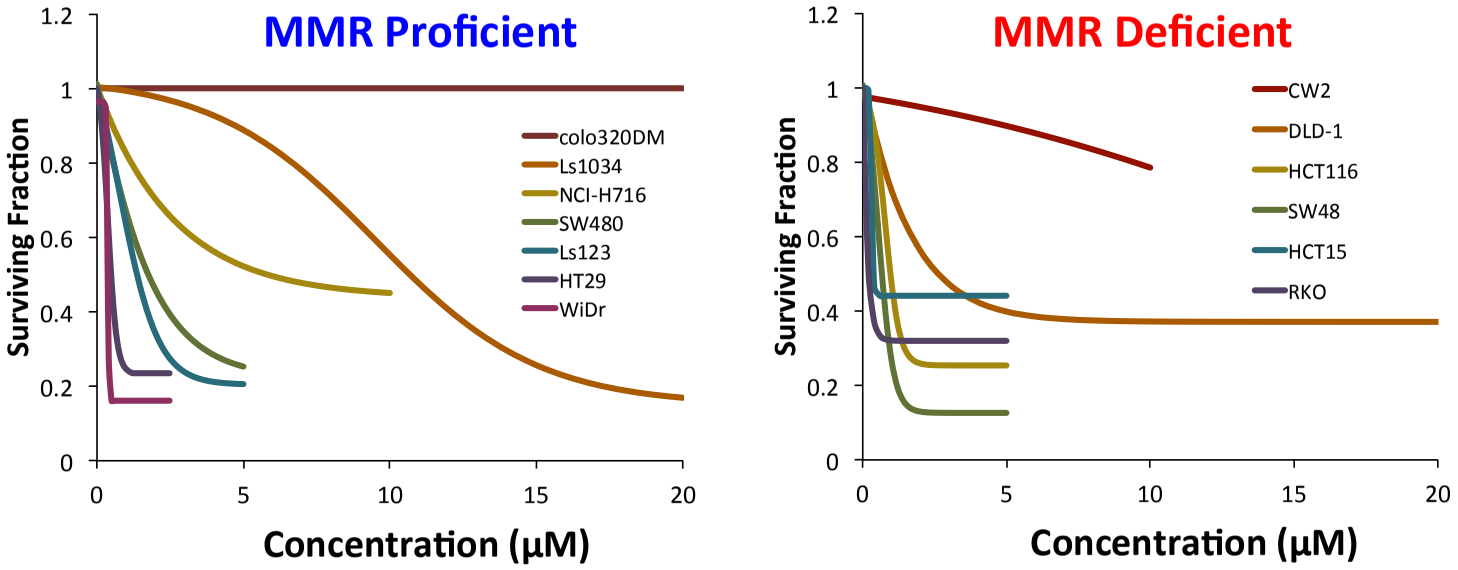

Figure 3.2 MTT Viability assay in a subset of colorectal cancer cell lines. When using the MTT viability assay, many cell lines never reach near-0% viability, even at high concentrations. Instead, they plateau as high as 40% viability, leading to challenges in data interpretation and comparison.

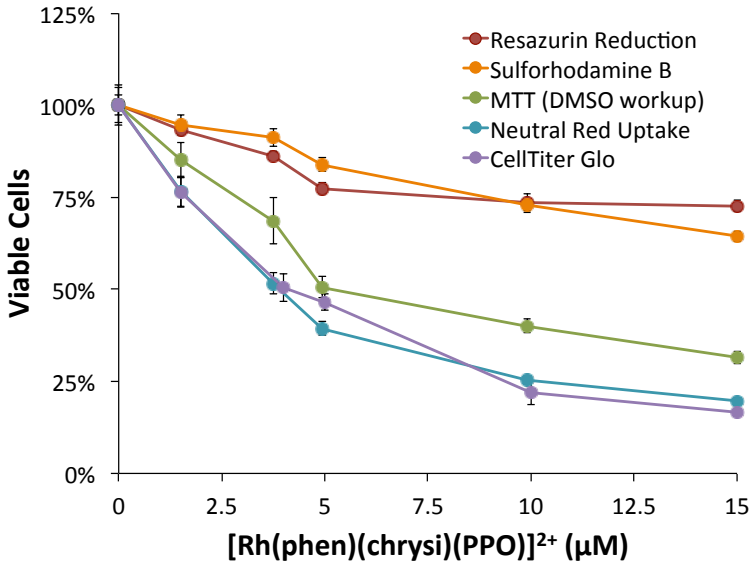

Figure 3.3 Comparison of different viability assays in the DLD-1 cell lines. The resazurin reduction, sulforhodamine B, MTT (with DMSO workup), neutral red, and CellTiter-Glo assays were performed on DLD-1 cells that had been incubated with varying concentrations of $[Rh(phen)(chrysi)(PPO)]^{2+}$ to establish the best viability method.

Cell Line	MMR +/-	Rh ~IC50 (uM)	Cisplatin ~IC50 (uM	MNNG ~IC50 (uM	Etoposide ~IC50 (uM
HCT116	–	1	23	25+	25+
DLD-1	–	6	14	20+	20
HCT15	–	16	13	18	20
LoVo	–	4	10	25+	2
Sw48	–	0.2	2	10	< 0.2
Ls174T	–	10	20+	20+	3
CW2	–	6	7	25	25+
RKO	–	0.15	11	20+	15
HT29	+	0.2	25+	25+	25
WiDr	+	0.2	25+	25	25+
Colo320DM	+	20+	4	6	8
NCI-H716	+	9	7	5	20+
SW620	+	1	8	10	4
Sw480	+	0.5	8	20+	13
Ls1034	+	1	15	20+	20+
Ls123	+	0.5	25	25+	7

= highest IC50

= lowest IC50

Figure 3.4 Comparison of a rhodium metalloinsertor to other chemotherapeutics across a panel of cell lines. The IC50 values of $[Rh(phen)(chrysi)(PPO)]^{2+}$ (**Rh**), cisplatin, MNNG, and etoposide in 16 cell lines, with a gradient color scheme applied to show the variation in IC50 from low (pink) to high (blue) concentrations. Overall the metalloinsertor is generally more potent than the other therapeutics (ex. in HCT116, RKO, SW480, etc.), though there are some cell lines where it has similar activity (HCT15) or is less potent (Colo320DM) than the other therapeutics.

viability in the NC assay under certain conditions (**Figure 3.5**). Despite this, challenges with this assay prevented its practical use. Specifically, several of the cell lines examine grow in islands—that is, cells will grow on top of each other instead of spreading out across the tissue culture dish, even at low cell densities (**Figure 3.5**). Cells that grow vertically will have overlapping nuclei when imaging from above, and these overlapping spots are either not fully counted (i.e., two spots directly overlapped will look like one spot) or are automatically not counted by the instrument (i.e., if the spot is too large it will not be considered a nucleus by the instrument). While this problem can be reduced by ensuring islands are broken apart before plating in the 96-well plate, the long dosing periods (72 h) necessary for metalloinsertor-induced cell death results in the untreated cells growing new islands during the duration of the experiment, complicating the analysis of these samples. Lastly, the required plate readers for these experiments are not readily available, therefore plates were brought to collaborators at City of Hope. As such, data could only be examined on City of Hope computers and it was unclear if the instrumentation was being set up to count nuclei in a fashion similar to the literature. While nuclear count experiments were ongoing, initial experiments using the CellTiter-Glo assay were performed and showed equally promising results to the NC assay but with none of the aforementioned complications. As such, the CellTiter-Glo assay was used for the remainder of the experiments.

3.3.2 Toxicity of $[Rh(phen)(chrysi)(PPO)]^{2+}$ and Cisplatin

We examined the potency of $[Rh(phen)(chrysi)(PPO)]^{2+}$ and the FDA-approved cisplatin, in 27 colorectal cancer cell lines to better understand the generality of the metalloinsertor's cytotoxic effects in diverse cell lines. We used a luciferase-based

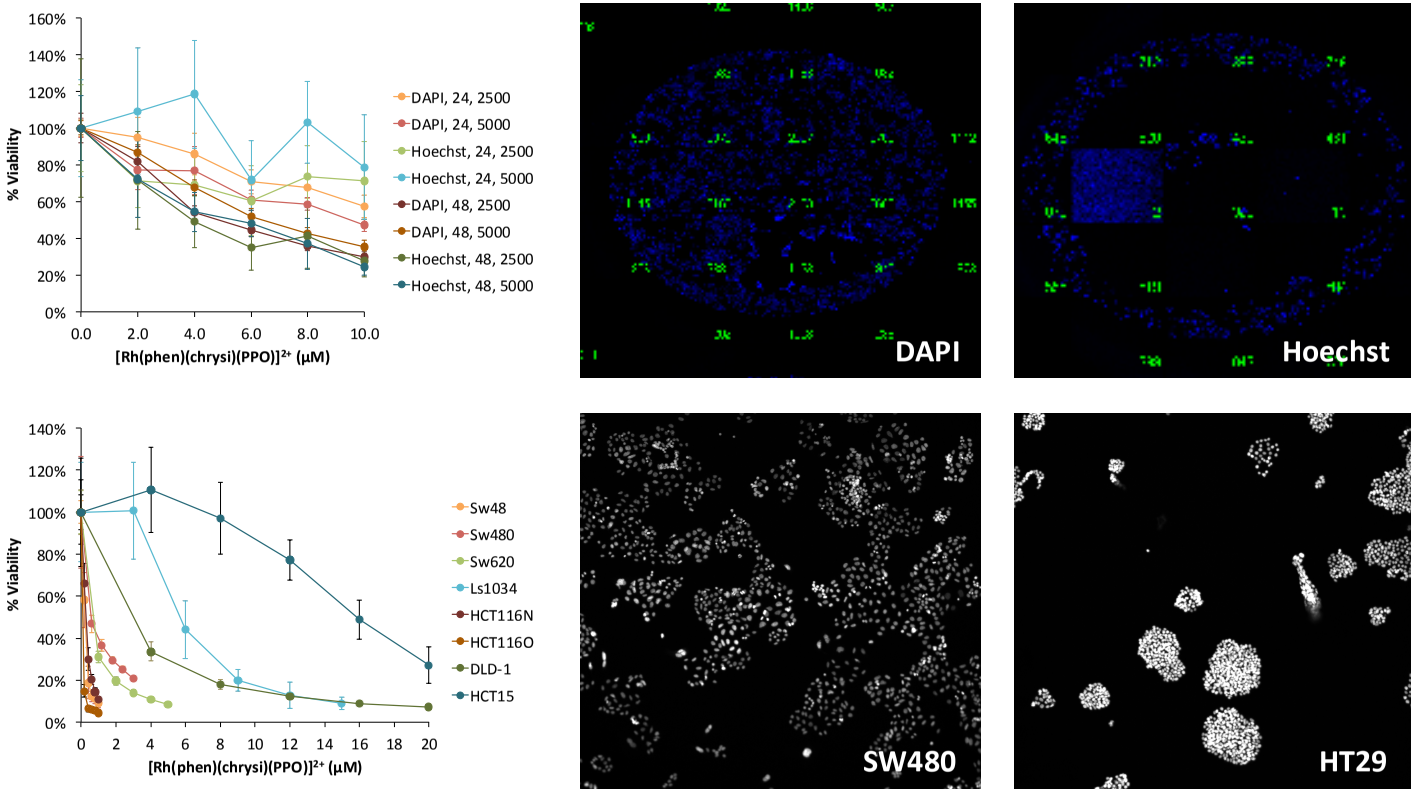

Figure 3.5 Nuclear Count assay in a subset of colorectal cancer cell lines. (Top left) comparison of DAPI and Hoechst staining methods at various seeding densities and time points. (Top middle) The DAPI protocol results in good cellular staining and distribution, while (Top right) the Hoechst protocol results in cell loss from the center of the well due to poor fixing. (Bottom) The DAPI protocol was used on several cell lines and most reached near-0% viability; however cellular clumping varied between cell lines, complicating result interpretation (bottom middle and right).

luminescence assay, which measures ATP of living cells, to develop a dose-response curve and determine the IC50 (50% inhibitory concentration) values for both drugs in all cell lines. As can be seen in **Figure 3.6**, the dose-response curves of $[Rh(phen)(chrysi)(PPO)]^{2+}$ vary dramatically across the 27 cell lines, with IC50 values spanning nearly three orders of magnitude and ranging from 63 ± 3 nM for Colo205 cells to 18 ± 3 μM for Colo320DM cells. Similarly, a range of IC50 values is observed for cisplatin (IC50 values from 2.2 ± 0.3 μM in SW48 cells to 36 ± 3 μM in Colo205 cells), however these IC50 values span only a single order of magnitude. The IC50 values for $[Rh(phen)(chrysi)(PPO)]^{2+}$ and cisplatin in each cell line can be found in **Table 3.2**. As can be seen in **Figure 3.6**, nearly every cell line is more sensitive to $[Rh(phen)(chrysi)(PPO)]^{2+}$ than it is to cisplatin, with the IC50 values of $[Rh(phen)(chrysi)(PPO)]^{2+}$ being on average 5 times lower than those of cisplatin ($[Rh(phen)(chrysi)(PPO)]^{2+}$ average IC50 = 2.9 μM; cisplatin average IC50 = 13.2 μM).

As can be seen in **Figure 3.7**, a wide range of sensitivities is seen for both MMR-deficient and MMR-proficient cell lines with no clear selectivity towards the MMR deficient cell lines. $[Rh(phen)(chrysi)(PPO)]Cl_2$ shows some selectivity towards the MMR-deficient cells (average IC50 of 2.5 μM; range 0.25-9.2 μM) compared to MMR-proficient cells (average IC50 of 3.0 μM; range 0.063-18.0 μM).[25] The selectivity increases further when looking only at cell lines with deficiencies in MLH1 or MSH2, the two most essential MMR proteins (average IC50 of 2.1 μM; range 0.25-9.2 μM). While these results are promising and follow the expected trend, due to the large ranges they cannot be considered statistically different, and in fact the same trend is observed for cisplatin, which is not MMR-selective in matched cell lines (**Figure 3.7**).

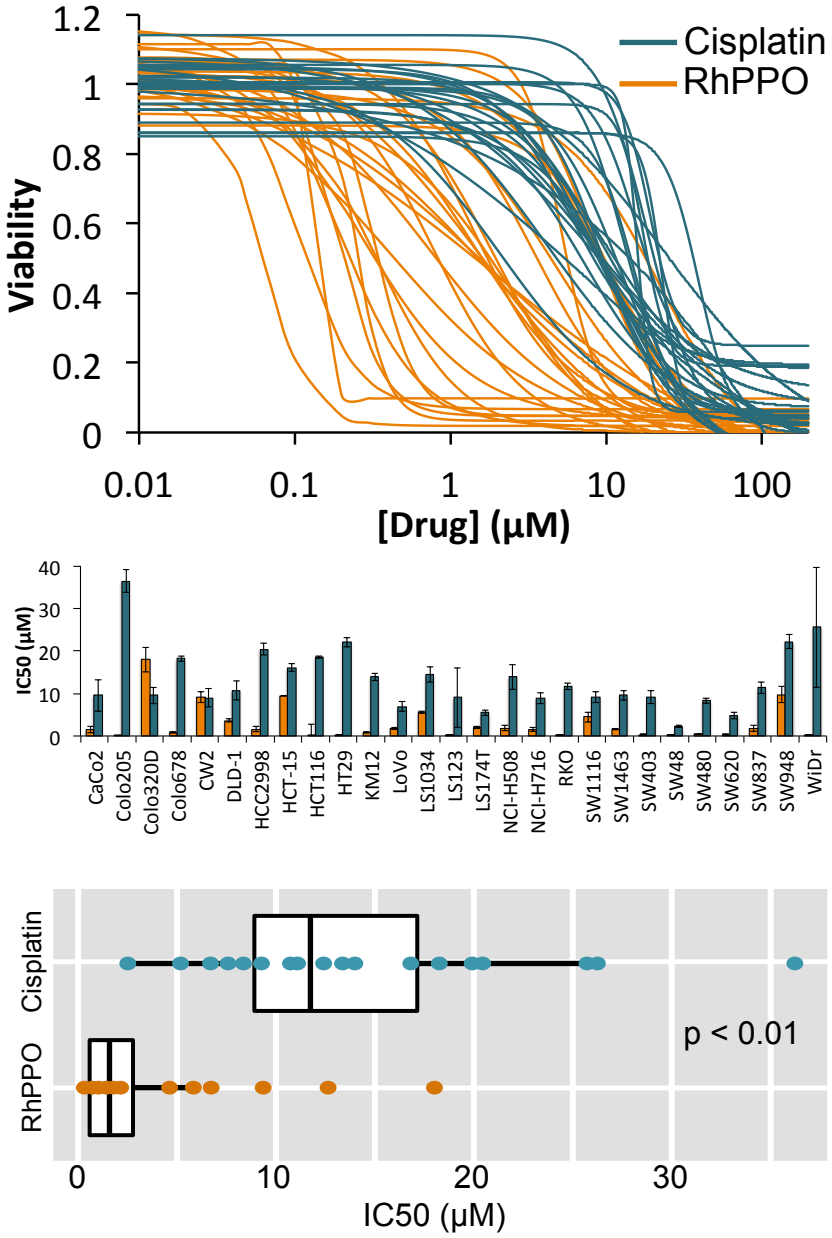

Figure 3.6 Cytotoxicity of $[Rh(phen)(chrysi)(PPO)]^{2+}$ (**RhPPO**) and cisplatin in 27 colorectal cancer cell lines. Dose response curves of $[Rh(phen)(chrysi)(PPO)]^{2+}$ and cisplatin in CRC cell lines (top). Direct IC50 comparison of $[Rh(phen)(chrysi)(PPO)]^{2+}$ and cisplatin in 27 CRC cell lines (middle) and boxplot representation, with an average IC50 for $[Rh(phen)(chrysi)(PPO)]^{2+}$ of 3.02 µM and a median of 1.34 µM, and an average IC50 for cisplatin of 13.89 µM and a median of 11.62 µM (bottom).

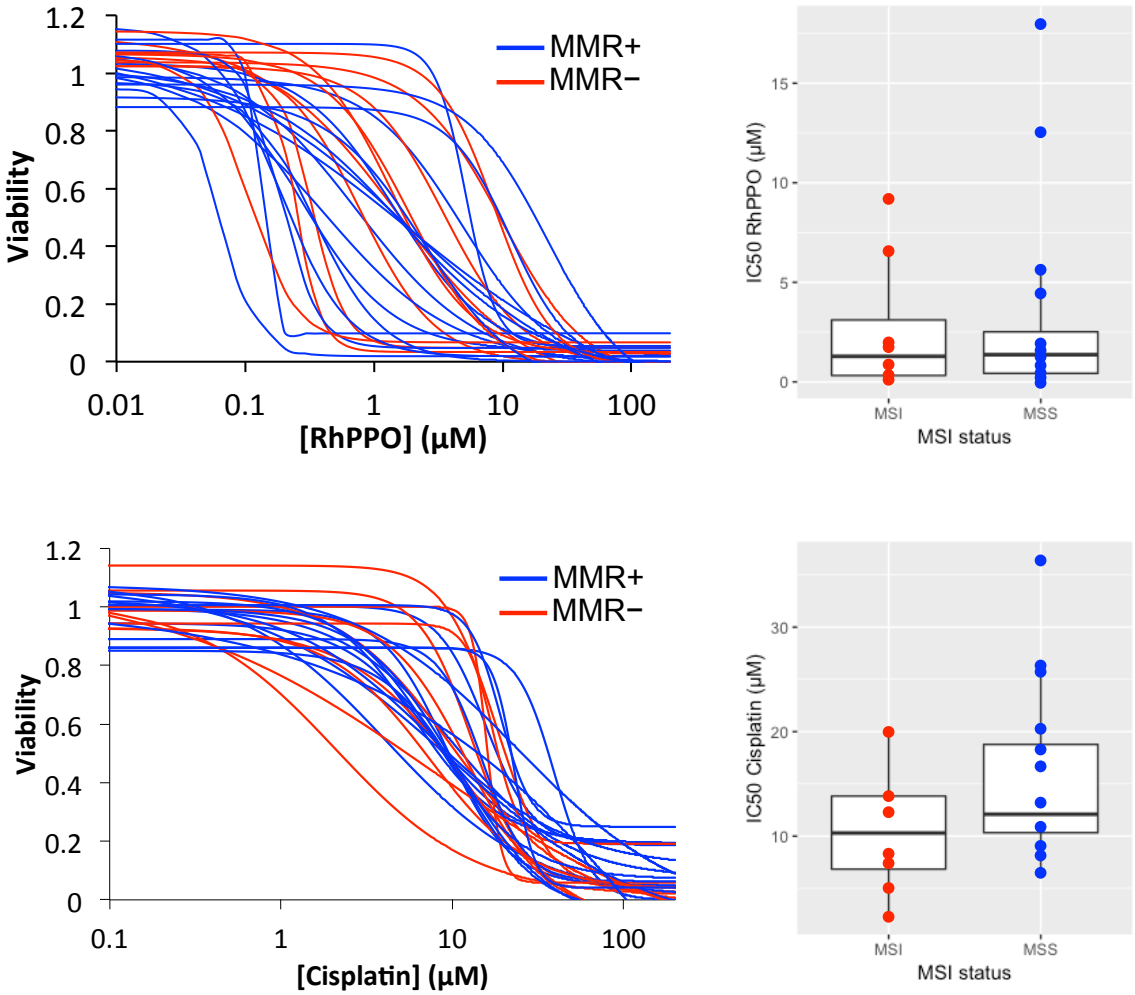

Figure 3.7 Cytotoxicity of a therapeutic in 27 colorectal cancer cell lines. (Top) Dose response curves of $[Rh(phen)(chrysi)(PPO)]^{2+}$ (**RhPPO**) in MMR-proficient (MMR+) and -deficient (MMR−) cell lines, with a comparison of the IC50 values shown in box plot form. The average IC50 of $[Rh(phen)(chrysi)(PPO)]^{2+}$ in MMR+ cells is 3.22 μM and the median is 1.37 μM. The average IC50 of $[Rh(phen)(chrysi)(PPO)]^{2+}$ in MMR− cells is 2.62 μM and the median is 1.28 μM. (Bottom) Dose response curves of cisplatin in MMR+ and MMR− cell lines, with a comparison of the IC50 values shown in box plot form. The average IC50 of cisplatin in MMR+ cells is 15.65 μM and the median is 12.09 μM. The average IC50 of cisplatin in MMR− cells is 10.38 μM and the median is 10.30 μM.

Table 3.2 IC50 values of $[Rh(phen)(chrysi)(PPO)]^{2+}$ and cisplatin in a panel of cell lines.

Cell Line	IC50 RhPPO (μM)	IC50 Cisplatin (μM)	IC50 RhPPO /IC50 Cisplatin	Cancer Type	MMR Status, (Mutated Protein)
CaCo-2	1.5 ± 0.8	9.5 ± 3.7	6.2	Colorectal	MMR+
Colo 205	0.063 ± 0.03	36.4 ± 2.8	580	Colorectal	MMR+
Colo 320DM	18.0 ± 2.9	9.5 ± 2.0	0.5	Colorectal	MMR+
Colo 678	0.81 ± 0.15	18.2 ± 0.7	22.4	Colorectal	MMR+
CW-2	9.2 ± 1.3	9.0 ± 2.1	1.0	Colorectal	MMR−, (−MLH1)
DLD-1 [c]	3.6 ± 0.3	10.7 ± 2.2	3.0	Colorectal	MMR−, (−MSH6)
HCC2998 [a]	1.6 ± 0.6	20.4 ± 1.4	12.6	Colorectal	MMR+, (−POLE)
HCT-116 [c]	0.25 ± 0.01	18.5 ± 0.9	73.3	Colorectal	MMR−, (−MLH1)
HCT-15	9.5 ± 2.5	16.1 ± 0.3	1.7	Colorectal	MMR−, (−MSH6)
HT-29	0.21 ± 0.01	22.1 ± 1.1	106	Colorectal	MMR+
KM-12	0.83 ± 0.07	13.9 ± 0.9	16.7	Colorectal	MMR−, (−MLH1)
LoVo	1.7 ± 0.2	7.0 ± 1.2	4.0	Colorectal	MMR−, (−MSH2)
Ls1034	5.6 ± 0.3	14.4 ± 1.9	2.6	Colorectal	MMR+
Ls123	0.23 ± 0.03	9.0 ± 7.0	39.7	Colorectal	MMR+
Ls174T	2.0 ± 0.2	5.4 ± 0.6	2.8	Colorectal	MMR−, (−MLH1)
NCI-H716	1.8 ± 0.6	13.9 ± 2.9	7.7	Colorectal	MMR+
NCI-H508	1.5 ± 0.4	8.8 ± 1.4	5.9	Colorectal	MMR+
RKO	0.12 ± 0.01	11.6 ± 0.7	97.5	Colorectal	MMR−, (−MLH1)
SW-1116	4.4 ± 1.2	9.1 ± 1.4	2.1	Colorectal	MMR+
SW-1463	1.6 ± 0.2	9.5 ± 1.1	6.0	Colorectal	MMR+
SW-403	0.34 ± 0.04	9.1 ± 1.5	27.1	Colorectal	MMR+
SW-48	0.34 ± 0.02	2.2 ± 0.2	6.4	Colorectal	MMR−, (−MLH1)
SW-480 [c]	0.44 ± 0.13	8.3 ± 0.6	12.0	Colorectal	MMR+
SW-620	0.33 ± 0.04	4.8 ± 0.8	14.7	Colorectal	MMR+
SW-837	1.8 ± 0.7	11.4 ± 1.3	6.2	Colorectal	MMR+
SW-948	9.7 ± 1.9	22.1 ± 1.7	2.3	Colorectal	MMR+
WiDr	0.13 ± 0.01	25.5 ± 14.1	198.7	Colorectal	MMR+
AN3-CA [c]	0.086 ± 0.003	--	--	Endometrial	MMR−, (−MLH1)
DU-145 [c]	0.67 ± 0.04	--	--	Prostate	MMR−, (−MLH1, PMS2)
HEC-1-A [c]	0.39 ± 0.02	--	--	Endometrial	MMR−, (−PMS2)
HCT-116N [b, c]	1.12 ± 0.27	--	--	Colorectal	MMR+
HCT-116O [b, c]	0.15 ± 0.06	--	--	Colorectal	MMR−, (−MLH1)

[a] HCC2998 is mutated in the POLE gene, leading to an increase in polymerase errors such as mismatches and indels. While it is not technically MMR-deficient, it will have higher mismatch and indel occurrences than other MMR-proficient cell lines.

[b] IC50 values from reference 24

[c] Cell lines used as the test set for the RhCy3 assay. Note that since the colorectal cancer cell lines examined in the cytotoxicity studies were primaily deficient in the MLH1 gene, this test set includes several cell lines of non-colorectal origin that span deficiencies in different MMR genes as well.

3.3.3 Whole Cell Uptake of $[Rh(phen)(chrysi)(PPO)]^{2+}$ Across Different Cell Lines

We examined the whole cell uptake of $[Rh(phen)(chrysi)(PPO)]^{2+}$ in twenty colorectal cancer cell lines by ICP-MS to determine if whole cell uptake of the metalloinsertor influenced its cytotoxicity in a given cell line. Cells were allowed to incubate for 24 h with the metalloinsertor, as we had previously observed that metalloinsertor uptake plateaus in both HCT116N and HCT116O cells by 24 h.[26] A concentration of 0.5 μM was selected to be great enough to ensure Rh detection by ICP-MS, but low enough to avoid significant cell death in sensitive cell lines (which could lead to challenges in data analysis). A correlation (Pearson's $r = -0.63$, $p < 0.01$) was observed between metalloinsertor uptake and log(IC50) of $[Rh(phen)(chrysi)(PPO)]^{2+}$ in different cell lines, as can be seen in **Figure 3.8.** This data confirms that uptake may play a role in overall cytotoxicity, as $[Rh(phen)(chrysi)(PPO)]^{2+}$ is more potent in cell lines exhibiting high uptake and the metalloinsertor is less potent in cell lines exhibiting low uptake.

3.3.4 Genomic DNA Binding of RhCy3 Across Different Cell Lines

To determine if the number of genomic DNA binding sites (mismatches, indels, and abasic sites) in different cell lines could explain the wide range of IC50 values observed for the $[Rh(phen)(chrysi)(PPO)]^{2+}$, we performed fluorescence titrations with the mismatch-specific fluorescent metalloinsertor, RhCy3 (**Figure 3.1**). Since the MMR-deficient colorectal cancer cell lines examined in the cytotoxicity assays are primarily deficient in the MLH1 gene, the test set used in this experiment included cell lines of non-colorectal origin that span deficiencies in different MMR genes (**Table 3.2**).[27] In

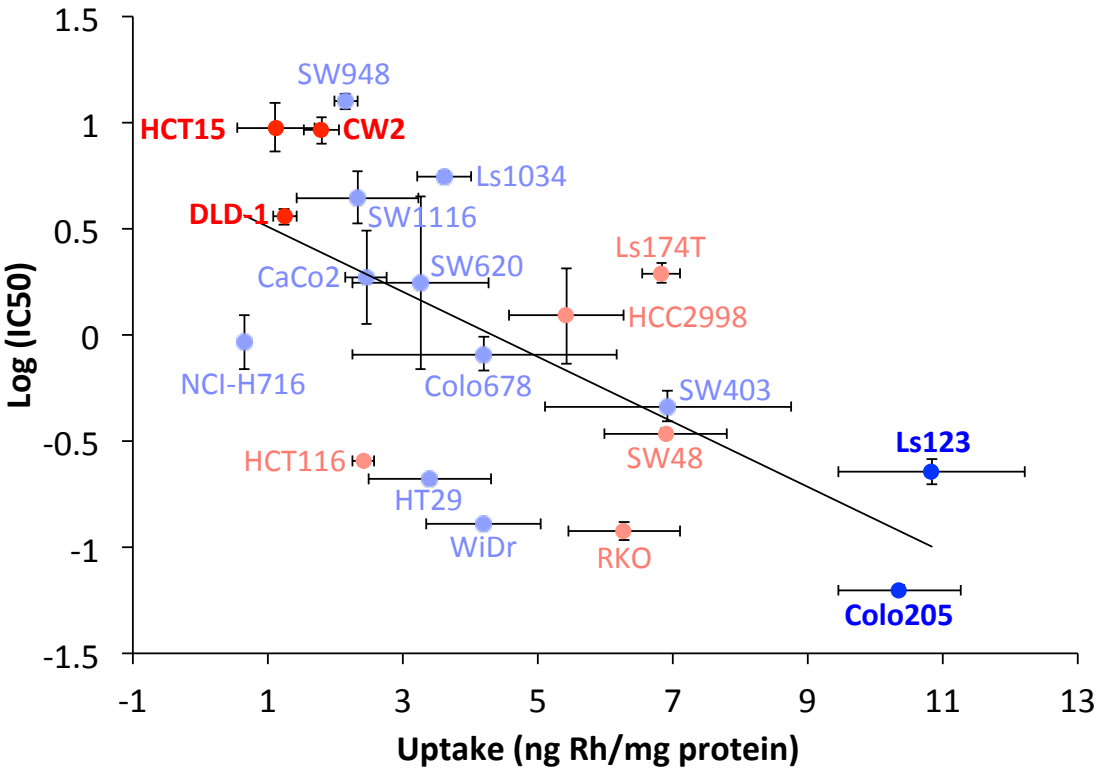

Figure 3.8 A correlation between whole cell uptake and IC50 for $[Rh(phen)(chrysi)(PPO)]^{2+}$. A correlation of -0.63 was observed. MMR-deficient cells are shown in pink and red, MMR-proficient cells are shown in light blue and blue. All cell lines are labeled and select cell lines discussed in the text are bolded and highlighted in red and blue.

these experiments, genomic DNA was extracted from the different cell lines and titrated into a solution of RhCy3 (**Figure 3.9**). As can be seen in **Figure 3.10,** a correlation (Pearson's r = -0.52, $p < 0.2$) was observed between the log(IC50) of $[Rh(phen)(chrysi)(PPO)]^{2+}$ and the fluorescence intensity of RhCy3 with genomic DNA of a given cell line. This correlation is increased upon the exclusion of a potential outlier, DU145 (Pearson's r = -0.81, $p < 0.05$). Overall, $[Rh(phen)(chrysi)(PPO)]^{2+}$ is more potent in cell lines exhibiting more lesions in their genomic DNA and less potent in cell lines exhibiting fewer lesions.

3.3.5 Genomic Features of Colorectal Cancer Cell Lines

While uptake and number of genomic lesions clearly correlate with cytotoxicity and can explain some unexpected trends and observations, there is also the possibility that additional factors may influence the MMR selectivity of $[Rh(phen)(chrysi)(PPO)]^{2+}$, such as the presence or absence of specific cancer-associated mutations or proteins. We examined the relationship between IC50 and the presence or absence of various proteins or phenotypes (CMS, CIMP, TP53, KRAS, BRAF, PIK3CA, and PTEN) according to the literature (**Figure 3.11**).[16,17] Overall, we observed no statistically significant ($p < 0.05$) correlations between IC50 and these genetic or epigenetic features, however some non-significant trends were visible in the data. For instance, cell lines with wild type p53 were more sensitive to $[Rh(phen)(chrysi)(PPO)]^{2+}$ (average IC50: 0.87 μM, range: 0.12-1.96 μM) than cell lines containing mutated p53 (average IC50: 3.74 μM, range: 0.06-18.0 μM). p53 is considered the guardian of the genome and plays a role in growth arrest, DNA repair, and apoptosis within the cell.[28] It is possible that wild-type p53 is involved in processing metalloinsertor-DNA lesions towards cell death, and therefore mutated

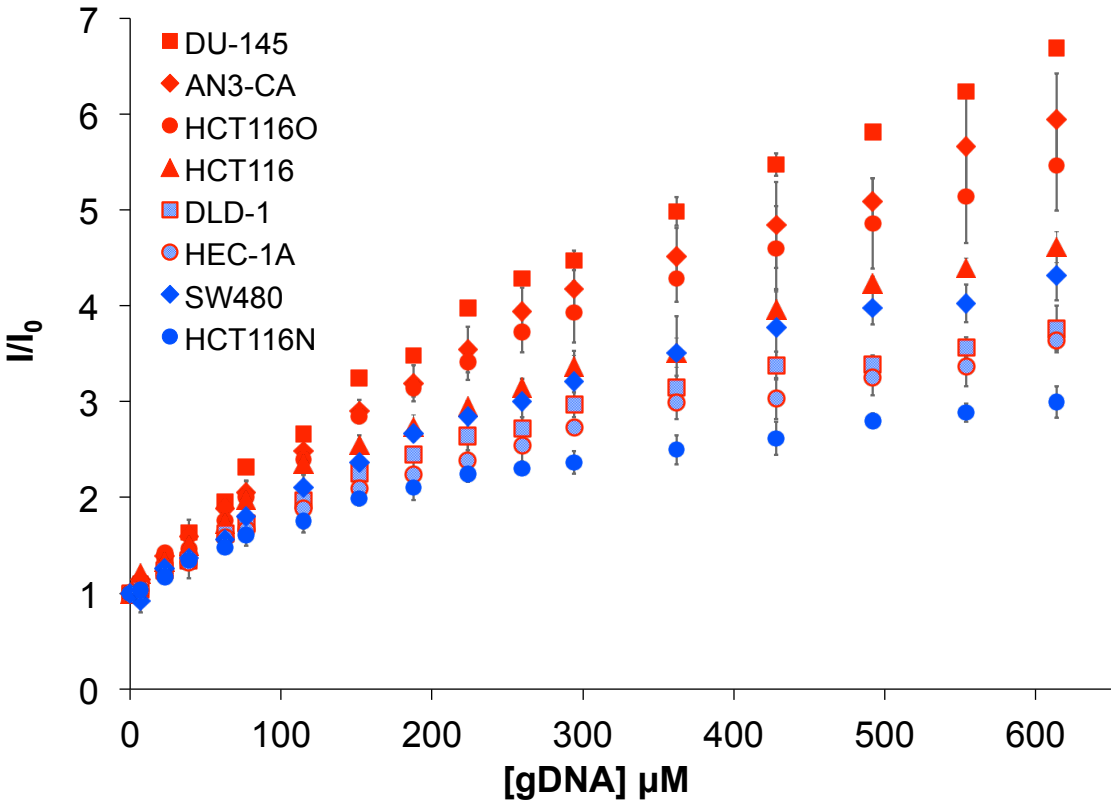

Figure 3.9 RhCy3 fluorescence titrations with genomic DNA. Full fluorescence titrations of gDNA extracted from eight different cancer cell lines. gDNA concentration is given as per base pair, I is the emission intergral from 548-675 nm as a scalar function measured after each addition of gDNA, and I_0 is the emission integral of RhCy3 solutions without gDNA.

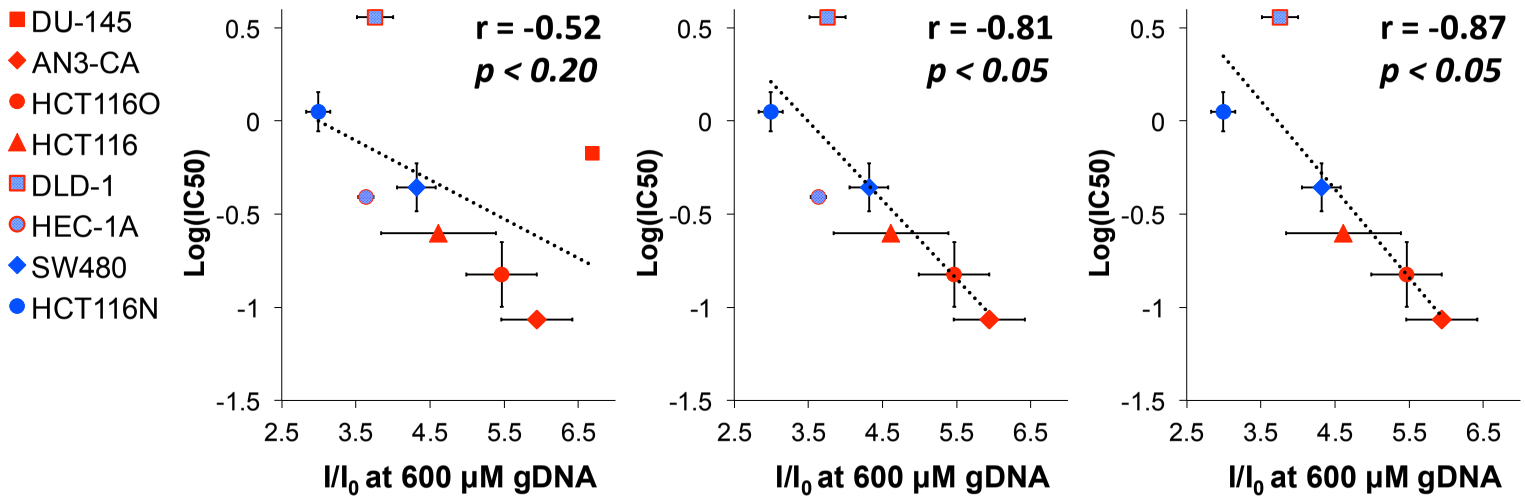

Figure 3.10 Relationship between gDNA lesion and IC50 of $[Rh(phen)(chrysi)(PPO)]^{2+}$ in assorted cell lines. gDNA lesions were measured using the fluorescent metalloinsertor RhCy3 and IC50 values were determined for the metalloinsertor $[Rh(phen)(chrysi)(PPO)]^{2+}$. (Left) The comparison of these properties across eight cell lines prodvides a Pearson's correlation of r = -0.52. (Middle) This correlation is increased to r=-0.81 if the potential outlier, DU145, is removed. (Right) The correlation is also improved if the PMS2-deficient cell lines, DU145 and HEC-1-A, are removed, resulting in a correlation of r=-0.87.

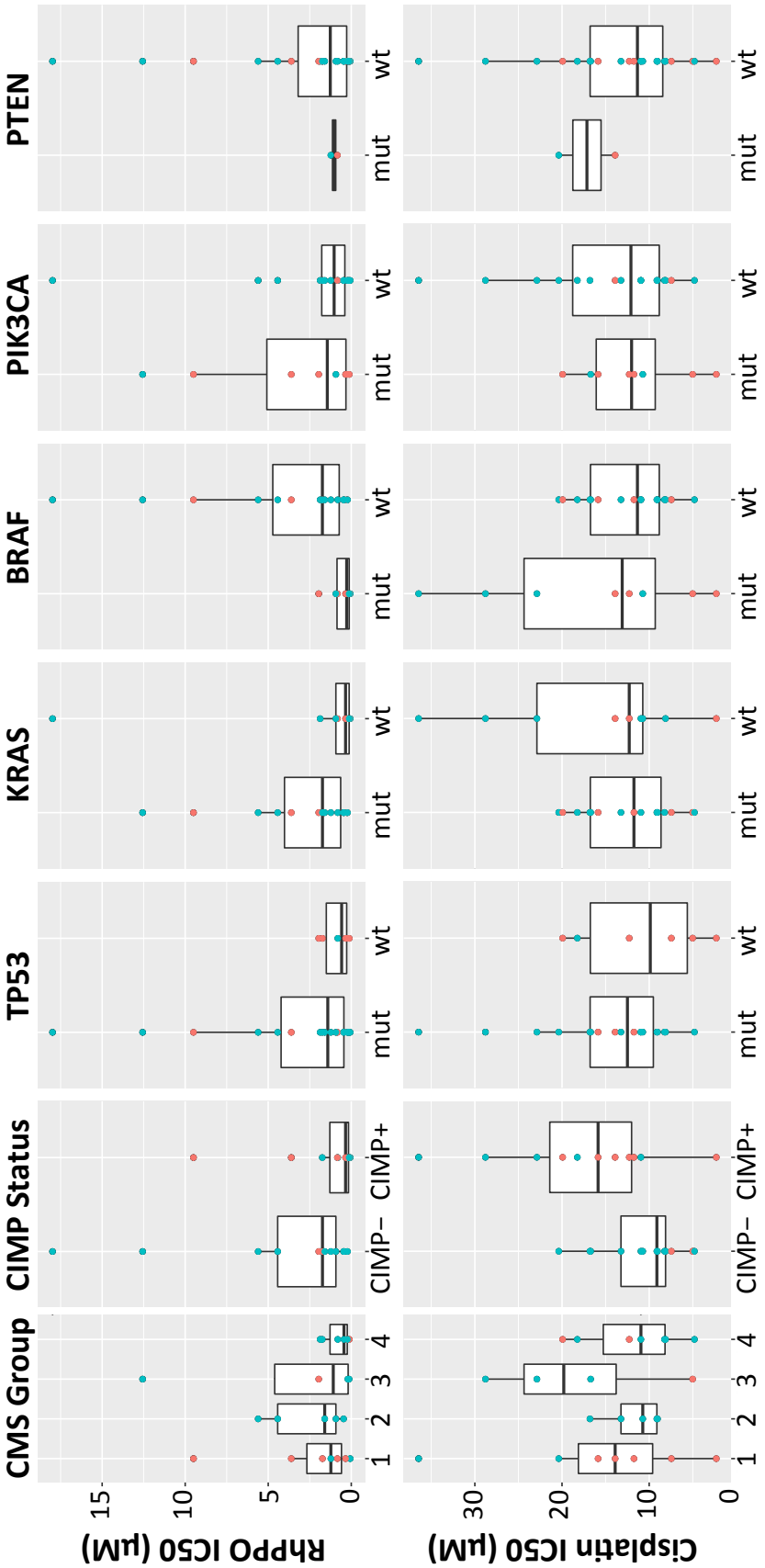

Figure 3.11 Relationship between IC50 of a therapeutic and selected biomarkers. Boxplot representations of the relationship between IC50 of $[Rh(phen)(chrysi)(PPO)]^{2+}$ and cisplatin to CMS subtype, CIMP status, and mutations in TP53, KRAS, BRAF, PIK3CA, and PTEN. MMR-deficient cell lines are shown in pink and MMR-proficient cell lines are shown in blue. Biomarker information taken from references 16 and 17.

p53 could lead to less effective processing of this lesion and therefore decreased cytotoxicity. There may also be a trend between IC50 and CIMP status with CIMP+ cell lines being more sensitive (average IC50: 3.24 μM, range 0.06-9.2 μM) than CIMP− cell lines(average IC50: 4.33 μM, range 0.23-18.0 μM). CIMP+ cells exhibit high methylation of CpG-rich DNA segments, including many promoter regions in DNA.[29] As such, inappropriate gene silencing is common CIMP+ cancers can cause deregulation of many essential genes, including genes involved in DNA repair and apoptosis. It is possible, therefore, that some of these deregulated genes could be involved in correcting or otherwise processing metalloinsertor-DNA lesions, leading to sensitivity in these cell lines. Non-significant trends are also observed with KRAS and BRAF genes, with cells containing wild-type KRAS and mutated BRAF being more sensitive than their counterparts. As mentioned before, there are no statistical differences between these groups; therefore this is all highly speculative.

3.4 Discussion

Rhodium metalloinsertors have shown great promise as potential chemotherapeutic agents for MMR-deficient cancers. As discussed above, metalloinsertors exhibit excellent cytotoxic selectivity towards MMR-deficient cancer cells over their MMR-proficient counterparts in matched pairings of cell lines. While these studies clearly demonstrate that rhodium metalloinsertors can target DNA mismatches when all other variables are kept constant, they are not necessarily predictive of clinical outcomes due to their lack of genetic and molecular diversity.

Here, we aimed to address this gap in our understanding by examining rhodium metalloinsertors in diverse colorectal cancers. We expanded our colorectal cancer cell

library to include 27 colorectal cancer cell lines that are largely unmatched and commercially available. These cell lines were selected to represent a diverse set of well-studied colorectal cancer cell lines: 9 have MMR deficiencies and 18 are MMR-proficient, the cell lines span the four distinct consensus molecular subtypes (CMS) of colorectal cancer, and a wealth of information has been gathered on the genetic, epigenetic, proteomic and transcriptomic differences between these cell lines by researchers in recent years.[16,30] We examined our most potent metalloinsertor, $[Rh(phen)(chrysi)(PPO)]^{2+}$ in these diverse cell lines to better understand its potential successes and limitations in a clinical setting.

3.4.1 Cytotoxicity Across 27 Colorectal Cancer Cell Lines

The *in vitro* potency of a drug has long been considered a key predictor of its clinical success.[31,32] Drugs with potencies in the nanomolar range are highly sought after, as they require lower dosing conditions for patients, they have the potential for lower off-target effects, and they circumvent solubility issues that commonly limit drug dosage.[31,33] Furthermore, potency is often the primary consideration for determining new drug leads and optimizing drug candidates in high throughput screening assays.[31]

To understand more fully the potential clinical applicability of rhodium metalloinsertors, we examined our most potent and selective metalloinsertor, $[Rh(phen)(chrysi)(PPO)]Cl_2$ (**Figure 3.1**), and compared it to the potency of the FDA approved chemotherapeutic agent cisplatin. Both metallodrugs target features of DNA for therapeutic activity, however they do so in dramatically different ways. $[Rh(phen)(chrysi)(PPO)]^{2+}$ binds preferentially to DNA base pair mismatches, which are non-abundant, through a non-covalent interaction. In contrast, cisplatin covalently binds

the abundant d(GpG) motifs present in DNA (**Figure 3.1**). Despite both having DNA as a target, $[Rh(phen)(chrysi)(PPO)]^{2+}$ is more potent than cisplatin in nearly every cell line, with the IC50 values of $[Rh(phen)(chrysi)(PPO)]^{2+}$ being on average 5 times lower than those of cisplatin (2.9 μM *vs.* 13.2 μM, respectively, **Figure 3.6**). This result is remarkable considering that DNA mismatches are significantly less abundant than d(GpG) sites and metalloinsertors interact only through non-covalent stacking with these mismatches. This high potency of $[Rh(phen)(chrysi)(PPO)]^{2+}$ relative to cisplatin highlights its great therapeutic potential. Furthermore, in the cell lines least sensitive to cisplatin (Colo205, HT29, and WiDr), $[Rh(phen)(chrysi)(PPO)]^{2+}$ is over 100 times more potent than cisplatin, with $[Rh(phen)(chrysi)(PPO)]^{2+}$ being 580 times more potent than cisplatin in the cell line Colo205 (**Table 3.2),** suggesting this metalloinsertor could be a particularly useful therapeutic for treatment of clinically challenging cisplatin-resistant tumors.

3.4.2 Selectivity Towards Cell Lines with MMR-deficiencies

A major clinical challenge of many small molecule chemotherapeutic agents, including cisplatin, is the development of off-target effects in patients. These off-target effects can often be detrimental to quality of life and even dose-limiting.[34] As such, the selectivity of a drug for cancer tissues over healthy tissues has been recognized as an increasingly important feature of new therapeutics, perhaps even more so than potency. As stated previously, rhodium metalloinsertors do exhibit high selectivity for deficiencies in MMR (which never occur in healthy tissues) when comparing matched cell lines. This study aimed to determine if MMR selectivity is conserved in unmatched, genetically diverse colorectal cancer cell lines.

When considering MMR status, a wide range of sensitivities is observed for both MMR-deficient and MMR-proficient cell lines (**Figure 3.7**). The sensitivities of some cell lines are contrary to what we expected based solely on MMR status; some MMR-deficient cell lines (DLD-1, HCT15, and CW2) show minimal sensitivity to $[Rh(phen)(chrysi)(PPO)]^{2+}$, whereas some MMR-proficient cell lines (HT29, WiDr, Ls123, and Colo205) show high sensitivity to $[Rh(phen)(chrysi)(PPO)]^{2+}$. Overall $[Rh(phen)(chrysi)(PPO)]^{2+}$ shows moderate selectivity towards the MMR-deficient cell lines (average IC50 of 2.5 μM) compared to MMR-proficient cell lines (average IC50 of 3.0 μM), and the selectivity increases further when looking only at cell lines with deficiencies in MLH1 or MSH2, the two most essential MMR proteins (average IC50 of 2.1 μM, **Figure 3.7).** These results are promising and follow the expected trend, however they are not as significant as anticipated.

The range observed for both MMR-deficient and MMR-proficient cell lines can be rationalized; unlike in matched cell lines, cell lines in this panel differ in mutations and regulation of many proteins.[16,17] It is generally accepted that the development of colorectal cancer requires multiple key driver mutations, with recent publications suggesting 3-10 driver mutations may be necessary.[13,14] While some of these mutations are more common than others (for instance, mutations in the BRAF and KRAS proteins are common in certain CMS groups of colorectal cancer), overall the mutations in different tumors can vary greatly, and epigenetic, transcriptomic, and proteomic aberrations can lead to even greater diversity.[2,16] Accordingly, there are several factors that could obscure the strong MMR-deficient selectivity we expected based on our hypothesis. We investigated two such factors that seemed likely to influence

metalloinsertor toxicity: cellular uptake and the number of lesions in genomic DNA that can be targeted by metalloinsertors. We also looked to available databases describing the molecular landscape of our colorectal cancer cells lines to attempt to identify other factors. While some correlations were observed, none were significant and therefore will not be discussed further.

3.4.3 The Influence of Cellular Uptake on Cytotoxicity

The biological target of the rhodium metalloinsertor is nuclear mismatched DNA, therefore uptake of the drug into the cell is crucial for metalloinsertor-induced cytotoxicity. Cell lines can exhibit different uptake and efflux properties towards small molecule therapeutic, therefore differences in uptake between cell lines may explain the wide cytotoxicity range of $[Rh(phen)(chrysi)(PPO)]^{2+}$.[35–38] We measured the whole cell uptake of $[Rh(phen)(chrysi)(PPO)]^{2+}$ after 24 hours in various cell lines by ICP-MS to determine if the whole cell uptake of $[Rh(phen)(chrysi)(PPO)]^{2+}$ correlated with cytotoxicity (**Figure 3.8**). A significant correlation was observed between increasing $[Rh(phen)(chrysi)(PPO)]^{2+}$ uptake and decreasing IC50. Furthermore, several of the results contrary to our hypothesis (i.e., high IC50 in MMR-deficient cells, low IC50 in MMR-proficient cells) are clarified by this assay; the three MMR-deficient cell lines least sensitive to $[Rh(phen)(chrysi)(PPO)]^{2+}$ (DLD-1, HT29, CW2) show the lowest cellular uptake and two of the most sensitive MMR-proficient cell lines (Ls123 and Colo205) exhibit the highest cellular uptakes. For these cell lines, high or low cellular uptake of $[Rh(phen)(chrysi)(PPO)]^{2+}$ likely obscures the selectivity that would normally be observed on the basis of MMR status alone. While this correlation between uptake and cytotoxicity is intuitive, it is of note that there are few reported studies correlating cellular

uptake and cytotoxicity of a small molecule therapeutic across *different* cell lines.[39] More commonly, reports examine the correlation of cellular uptake and cytotoxicity of different therapeutics in a single cell line or look only at a relatively small number of cell lines.[40] Therefore, our results comparing cytotoxicity and cellular uptake suggest that uptake may often play a non-negligible role in the cytotoxicity differences of a small molecule therapeutic between cell lines.

3.4.4 The Influence of Genomic DNA Binding Sites on Cytotoxicity

While a correlation between cytotoxicity and uptake is expected for any small molecule therapeutic, a correlation between cytotoxicity and DNA binding would only be expected if DNA were the relevant biological target of the therapeutic being studied. As discussed previously, inactivation of MMR proteins confers the cells with an increased level of uncorrected mismatches and indels that propagate into mutations upon replication.[4] The number of these lesions in the genome can fluctuate between cell lines, for instance mutations (an indirect measure of mismatches and indels) occur at different rates in cell lines deficient in different MMR proteins.[27] The number of these lesions present in the genomic DNA (gDNA) of a cell could influence differences in potency of $[Rh(phen)(chrysi)(PPO)]^{2+}$, which targets these mismatches and indels, in different cell lines.[8,10] Currently, there are limited direct protocols to determine the number of destabilized lesions in gDNA. Fluorescence-based probes have been widely used to visualize and quantify dynamic processes in live cells *via* interaction with various biological targets.[41] As such, our group recently reported a bifunctional fluorescent probe, RhCy3, which exhibits a fluorescent light-up effect upon interaction with thermodynamically destabilized mismatches in gDNA (**Figure 3.1**).[19] The fluorescence

of RhCy3 is an exceptional readout on the relative number of destabilized lesions in gDNA and an excellent predictor of the relative number of targetable DNA lesion for $[Rh(phen)(chrysi)(PPO)]^{2+}$, which is structurally similar.

Here we use this probe to better understand the cytotoxic effect of $[Rh(phen)(chrysi)(PPO)]^{2+}$ on a panel of cancer cell lines, but these studies also demonstrate the powerful detection and diagnostics properties of RhCy3 in MMR-deficient cancers. We performed fluorescence titrations with RhCy3 and increasing amounts of gDNA extracted from a test set of eight cell lines that span deficiencies in different MMR genes (**Table 3.2**).[27] As can be seen in **Figure 3.10**, a correlation was observed between increasing RhCy3 fluorescence and decreasing IC50 of $[Rh(phen)(chrysi)(PPO)]^{2+}$. By removing the potential outlier, DU145 (the only cell line tested mutated in two MMR proteins), the correlation improves dramatically and becomes significant, suggesting other factors may influence the cytotoxicity of $[Rh(phen)(chrysi)(PPO)]^{2+}$ or fluorescence of RhCy3 in DU145. This strong correlation between the IC50 of $[Rh(phen)(chrysi)(PPO)]^{2+}$ and the fluorescence of the reporter RhCy3 confirms that the effective biological target of rhodium metalloinsertors is, in fact, DNA lesions such as mismatches and indels, and that differences in the number of these lesions between different cell lines controls cytotoxicity of metalloinsertor therapeutics.

Remarkably, there is a clear relationship between the identity of the malfunctioning MMR protein and RhCy3 fluorescence. The genomic DNA extracted from cell lines with a deficiency in the MLH1 protein (HCT116O, AN3-CA, DU-145, and HCT116) reach the highest fluorescence intensities, indicating there are an abundance of targetable DNA lesions present in these cell lines (**Figure 3.9**). Conversely,

the MMR-deficient cell lines DLD-1 and HEC-1-A have low fluorescence intensity that is comparable to that of the MMR-proficient cell lines, HCT116N and SW480. It may be possible to explain the low intensity observed with DLD-1 and HEC-1-A by considering their specific MMR-deficiencies: MSH6 and PMS2, respectively. Functioning MMR generally involves two heterodimers, MutSα (MSH2 + MSH6) and MutLα (MLH1 + PMS2), to work together to identify and correct mismatches and indels. However, other homologues to these heterodimers also exist: MutSβ (MSH2 + MSH3), MutLβ (MLH1 + MLH2), and MutLγ (MLH1 + MLH3).[4] These different MutS and MutL homologues have different roles in the cell, with MutSα and MutLα correcting mismatches and some indels, and MutSβ, MutLβ, and MutLγ contributing to the correction of long and short indels, but not mismatches. A cell line deficient in MSH2 or MLH1 (which are part of *all* MutS and MutL homologues, respectively) cannot correct mismatches or indels, however a cell line deficient in MSH6 or PMS2 will only lack one homologue (MutSα or MutLα, respectively) and therefore may still be able to correct indels via functioning MutSβ, MutLβ, and MutLγ homologues. Considering this, it seems possible that the fluorescence of DLD-1 and HEC-1-A are relatively low because these cell lines have MMR machinery that can correct indels, meaning they will have fewer targetable lesions than MLH1-deficient cells, which can correct neither mismatches nor indels. It is also of note that the MMR-proficient cell lines have significant fluorescence despite their minimal mismatches and indels. We attribute this baseline fluorescence (as well as deviations between MMR-deficient cell lines) to RhCy3 binding abasic sites or other thermodynamically destabilized lesions that are not associated with MMR pathways. Once again, these results show how RhCy3 can serve as a direct detection method of

destabilized lesions in MSI tumors and a potential diagnostic for MMR deficiencies in cancer.

3.4.5 General Implications and Warning Signs for *in vitro* Studies

The results presented here highlight some interesting considerations for *in vitro* studies performed in any laboratory. We observed a large range of IC50 values spanning nearly three orders of magnitude for a single small molecule therapeutic across 27 cell lines. This result alone has significant implications for *in vitro* experiments. Many studies examine a therapeutic of interest in a single cell line or one cell line from several types of cancer (colorectal, ovarian, etc.), but clearly a single cell line cannot represent cancer or any subtype of cancer as a whole.

It is also common to compare cytotoxicity in unmatched cell lines that differ in the expression level of a protein of interest (regular expression, overexpression, and underexpression). Our results here suggest that using only a small number of unmatched cell lines may produce misleading results. For example, in this study we could consider MMR-proficient cells to have regular MMR expression and MMR-deficient to underexpress MMR proteins. If we randomly chose only two cell lines from our panel, one MMR-proficient and one MMR-deficient, we could observe every possible trend. Comparing RKO (MMR-deficient, IC50: 120 nM) and Colo320DM (MMR-proficient, IC50: 18.0 μM) would suggest $[Rh(phen)(chrysi)(PPO)]^{2+}$ is dramatically more toxic in MMR-deficient cells, however comparing CW2 (MMR-deficient, IC50: 9.2 μM) and Colo205 (MMR-proficient, IC50: 63 nM) would suggest the opposite trend, with $[Rh(phen)(chrysi)(PPO)]^{2+}$ being dramatically *less* toxic in MMR-deficient cells.

Overall, we believe the large range of IC50 values observed here serves as a point of caution for researchers performing *in vitro* studies in a limited number of cell lines; cell line selection can unintentionally but dramatically influence the trends a researcher observes in their studies, and therefore we encourage researchers to perform these studies with larger panels of cell lines and to supplement them using matched cell lines, which reduce the inter-cell line variation and allow one to observe the effect of a therapeutic on a specific target.

3.5 Conclusion

In summary, the experiments described here underscore the therapeutic and diagnostic potentials of mismatch-targeted small molecules. The potency of $[Rh(phen)(chrysi)(PPO)]^{2+}$ across diverse cell lines spans nearly three orders of magnitude and shows selectivity towards MMR-deficient cancer cells. $[Rh(phen)(chrysi)(PPO)]^{2+}$ is on average 5 times more potent than cisplatin, despite having a less abundant target to which it binds non-covalently. Overall, these results show $[Rh(phen)(chrysi)(PPO)]^{2+}$ is a potent and promising therapeutic agent for colorectal cancers, and *in vivo* experiments are in progress. Significantly, using the fluorescent probe RhCy3, we find that the DNA mismatch represents an effective biological target for the metalloinsertors, and that targeting these lesions leads to cell death. As such, RhCy3 can serve as a direct detection method for destabilized lesions in genomic DNA (the DNA mismatches and indels) and for diagnosing MMR deficiencies in MSI tumors.

3.6 References

(1) Cronin, K. A.; Lake, A. J.; Scott, S.; Sherman, R. L.; Noone, A. M.; Howlader, N.; Henley, S. J.; Anderson, R. N.; Firth, A. U.; Ma, J.; Kohler, B. A.; Jemal, A. *Cancer* **2018**, *124*, 2785–2800.

(2) Guinney, J.; Dienstmann, R.; Wang, X.; De Reyniès, A.; Schlicker, A.; Soneson, C.; Marisa, L.; Roepman, P.; Nyamundanda, G.; Angelino, P.; Bot, B. M.; Morris, J. S.; Simon, I. M.; Gerster, S.; Fessler, E.; De Sousa .E Melo, F.; Missiaglia, E.; Ramay, H.; Barras, D.; Homicsko, K.; Maru, D.; Manyam, G. C.; Broom, B.; Boige, V.; Perez-Villamil, B.; Laderas, T.; Salazar, R.; Gray, J. W.; Hanahan, D.; Tabernero, J.; Bernards, R.; Friend, S. H.; Laurent-Puig, P.; Medema, J. P.; Sadanandam, A.; Wessels, L.; Delorenzi, M.; Kopetz, S.; Vermeulen, L.; Tejpar, S. *Nat. Med.* **2015**, *21*, 1350–1356.

(3) Arzimanoglou, I. I.; Gilbert, F.; Barber, H. R. K. *Cancer* **1998**, *82*, 1808–1820.

(4) Kunkel, T. A.; Erie, D. A. *Annu. Rev. Genet.* **2015**, *49*, 291–313.

(5) Steven Lemery, Patricia Keegan, and R. P. *N. Engl. J. Med.* **2017**, *377*, 1409–1412.

(6) Hatch, S. B.; Lightfoot, H. M.; Garwacki, C. P.; Moore, D. T.; Calvo, B. F.; Woosley, J. T.; Sciarrotta, J.; Funkhouser, W. K.; Farber, R. A. *Clin. Cancer Res.* **2005**, *11*, 2180–2187.

(7) Jackson, B. A.; Barton, J. K. *Biochemistry* **2000**, *39*, 6176–6182.

(8) Jackson, B. A.; Alekseyev, V. Y.; Barton, J. K. *Biochemistry* **1999**, *38*, 4655–4662.

(9) Pierre, V. C.; Kaiser, J. T.; Barton, J. K. *Proc. Natl. Acad. Sci.* **2007**, *104*, 429–434.

(10) Zeglis, B. M.; Boland, J. A.; Barton, J. K. *Biochemisrty* **2009**, *48*, 839–849.

(11) Hart, J. R.; Glebov, O.; Ernst, R. J.; Kirsch, I. R.; Barton, J. K. *Proc. Natl. Acad. Sci.* **2006**, *103*, 15359–15363.

(12) Bailis, J. M.; Gordon, M. L.; Gurgel, J. L.; Komor, A. C.; Barton, J. K.; Kirsch, I. R. *PLoS One* **2013**, *8*, e78726.

(13) Tomasetti, C.; Marchionni, L.; Nowak, M. A.; Parmigiani, G.; Vogelstein, B. *Proc. Natl. Acad. Sci.* **2015**, *112*, 118–123.

(14) Martincorena, I.; Raine, K. M.; Gerstung, M.; Dawson, K. J.; Haase, K.; Van Loo, P.; Davies, H.; Stratton, M. R.; Campbell, P. J. *Cell* **2017**, *171*, 1029–1041.

(15) Komor, A. C.; Barton, J. K. *J. Am. Chem. Soc.* **2014**, *136*, 14160–14172.

(16) Berg, K. C. G.; Eide, P. W.; Eilertsen, I. A.; Johannessen, B.; Bruun, J.; Danielsen, S. A.; Bjørnslett, M.; Meza-Zepeda, L. A.; Eknæs, M.; Lind, G. E.; Myklebost, O.; Skotheim, R. I.; Sveen, A.; Lothe, R. A. *Mol. Cancer* **2017**, *16*, 1–16.

(17) Linnekamp, J. F.; Van Hooff, S. R.; Prasetyanti, P. R.; Kandimalla, R.; Buikhuisen, J. Y.; Fessler, E.; Ramesh, P.; Lee, K. A. S. T.; Bochove, G. G. W.; De Jong, J. H.; Cameron, K.; Van Leersum, R.; Rodermond, H. M.; Franitza, M.; Nürnberg, P.; Mangiapane, L. R.; Wang, X.; Clevers, H.; Vermeulen, L.; Stassi, G.; Medema, J. P. *Cell Death Differ.* **2018**, *25*, 616–633.

(18) Komor, A. C.; Barton, J. K. *J. Am. Chem. Soc.* **2014**, *136*, 14160–14172.

(19) Nano, A.; Boynton, A. N.; Barton, J. K. *J. Am. Chem. Soc.* **2017**, *139*, 17301–17304.

(20) Van Tonder, A.; Joubert, A. M.; Cromarty, A. D. *BMC Res. Notes* **2015**, *8*, 1–10.

(21) Vichai, V.; Kirtikara, K. *Nat. Protoc.* **2006**, *1*, 1112–1116.

(22) Repetto, G.; del Peso, A.; Zurita, J. L. *Nat. Protoc.* **2008**, *3*, 1125–1131.

(23) Komor, A. C.; Schneider, C. J.; Weidmann, A. G.; Barton, J. K. *J. Am. Chem. Soc.* **2012**, *134*, 19223–19233.

(24) Bailis, J. M.; Weidmann, A. G.; Mariano, N. F.; Barton, J. K. *Proc. Natl. Acad. Sci.* **2017**, *114*, 6948–6953.

(25) Unsurprisingly, cell lines derived from a common patient and therefore having identical genomes (DLD-1/HCT15, HT29/WiDr, and SW480/SW620) had similar IC50 values. To avoid double-counting cells derived from a common patient, IC50 values for these pairings.

(26) Boyle, K. M.; Barton, J. K. *J. Am. Chem. Soc.* **2018**, *140*, 5612–5624.

(27) Glaab, W. E.; Tindall, K. R. *Carcinogenesis* **1997**, *18*, 1–8.

(28) Chen, J. *Cold Spring Harb. Perspect. Med.* **2016**, *6*, 1–16.

(29) Mojarad, E. N.; Kuppen, P. J. K.; Aghdaei, H. A.; Zali, M. R. *Gastroenterol. Hepatol. from Bed to Bench* **2013**, *6*, 120–128.

(30) Ahmed, D.; Eide, P. W.; Eilertsen, I. A.; Danielsen, S. A.; Eknæs, M.; Hektoen, M.; Lind, G. E.; Lothe, R. A. *Oncogenesis* **2013**, *2*, 1–8.

(31) Gleeson, M. P.; Hersey, A.; Montanari, D.; Overington, J. *Nat. Rev. Drug Discov.* **2011**, *10*, 197–208.

(32) Hughes, J. P.; Rees, S. S.; Kalindjian, S. B.; Philpott, K. L. *Br. J. Pharmacol.* **2011**, *162*, 1239–1249.

(33) Lipinski, C. *Am. Pharm. Rev.* **2002**, *5*, 82–85.

(34) Oun, R.; Moussa, Y. E.; Wheate, N. J. *Dalt. Trans.* **2018**, *47*, 6645–6653.

(35) Mueller, J.; Kretzschmar, I.; Volkmer, R.; Boisguerin, P. *Bioconjug. Chem.* **2008**, *19*, 2363–2374.

(36) Solazzo, M.; Fantappie, O.; D'Amico, M.; Sassoli, C.; Tani, A.; Cipriani, G.; Bogani, C.; Formigli, L.; Mazzanti, R. *Cancer Res.* **2009**, *69*, 7235–7242.

(37) Krishna, R.; Mayer, L. D. *Pharm. Pharmacol. Commun.* **1999**, *5*, 511–517.

(38) Motskin, M.; Wright, D. M.; Muller, K.; Kyle, N.; Gard, T. G.; Porter, A. E.; Skepper, J. N. *Biomaterials* **2009**, *30*, 3307–3317.

(39) Dayton, A.; Selvendiran, K.; Kuppusamy, M. L.; Rivera, B. K.; Meduru, S.; Kálai, T.; Hideg, K.; Kuppusamy, P. *Cancer Biol. Ther.* **2010**, *10*, 1027–1032.

(40) Davis, K. J.; Carrall, J. A.; Lai, B.; Aldrich-Wright, J. R.; Ralph, S. F.; Dillon, C. T. *Dalt. Trans.* **2012**, *41*, 9417–9426.

(41) Liu, H. W.; Chen, L.; Xu, C.; Li, Z.; Zhang, H.; Zhang, X. B.; Tan, W. *Chem. Soc. Rev.* **2018**, *47*, 7140–7180.

Chapter 4

EFFORTS TOWARDS THE STRUCTURAL DETERMINATION OF A RHODIUM METALLOINSERTOR BOUND TO A DNA MISMATCH*

4.1 Introduction

Biochemical assays can provide excellent insight on the cellular target of a therapeutic agent, and cell culture experiments can predict potential clinical applicability. Despite the wealth of information that can be gained in these experiments, a structural understanding of a how a drug interacts with its cellular target is often key to fully understanding and developing new therapeutic agents.[1] One of the most common targets for the development of new chemotherapeutic agents is DNA.[2] Traditionally, FDA-approved chemotherapeutic agents target DNA through three main binding modes: intercalation, groove binding, and covalent binding.[3] While these binding modes certainly give rise to the cytotoxic properties that allow these drugs to kill cancer cells, they generally lack selectivity for cancer-specific targeting. As such, the development of new complexes that bind to disease-associated DNA structures is a current topic of interest for many chemical and biochemical research groups. In the development of these unique, first-in-class therapeutic agents, structural determination through NMR or X-ray crystallography is essential in confirming the novel interactions these complexes have with their cellular targets. Furthermore, this structural determination can inform the development of these complexes towards more potent, more selective anticancer agents.

---

* Crystal data was collected using the SLAC beamline with the guidance of Dr. Jens Kaiser, and Dr. Kaiser solved and preliminarily refined the crystal structure of TC mismatched DNA presented herein.

There are many examples in the literature of novel DNA binding modes being discovered through X-ray crystallography. For instance, the multi-nuclear platinum complex TriplatinNC shows micromolar activity against human ovarian cancer cell lines.[4] Unlike its parent complex, cisplatin, TriplatinNC has no labile chloride ligands and therefore can only interact with DNA in a non-covalent manner.[5] This non-covalent interaction was identified to be a novel binding mode, termed a "phosphate clamp," in which the amines of TriplatinNC non-covalently interact with the oxygen atoms along the phosphate backbone of DNA.

Similarly, biochemical assays have been used by the Barton group to establish that a class of rhodium complexes (termed rhodium metalloinsertors) could selectively bind to DNA mismatches, an abundance of which are associated with several types of cancer.[6,7] In 2007, this selectivity was confirmed to be through a novel DNA binding mode, metalloinsertion, which had been proposed by L.S. Lerman in 1961 but never confirmed.[8,9] In this crystal structure, the rhodium metalloinsertor, $[Rh(bpy)_2(chrysi)]^{3+}$, binds to DNA from the minor groove at a mismatched site and ejects the mismatched from the DNA π-stack (**Figure 4.1**). In addition to highlighting the structural mode of mismatch selectivity, this crystal structure allowed the Barton group to rationalize the biological activity of some of the metalloinsertors they had synthesized. For instance, the bulky metalloinsertor, $[Rh(DIP)_2(chrysi)]^{3+}$, has extremely low binding affinity to mismatched DNA (10^4 M^{-1}) compared to the less bulky $[Rh(bpy)_2(chrysi)]^{3+}$ (10^7 M^{-1}).[10] This dramatic drop in binding ability can be clearly rationalized when modeling $[Rh(DIP)_2(chrysi)]^{3+}$ into the DNA lesion that was crystallographically observed with $[Rh(bpy)_2(chrysi)]^{3+}$ (**Figure 4.1**). In this model, steric clashing is seen between the DIP

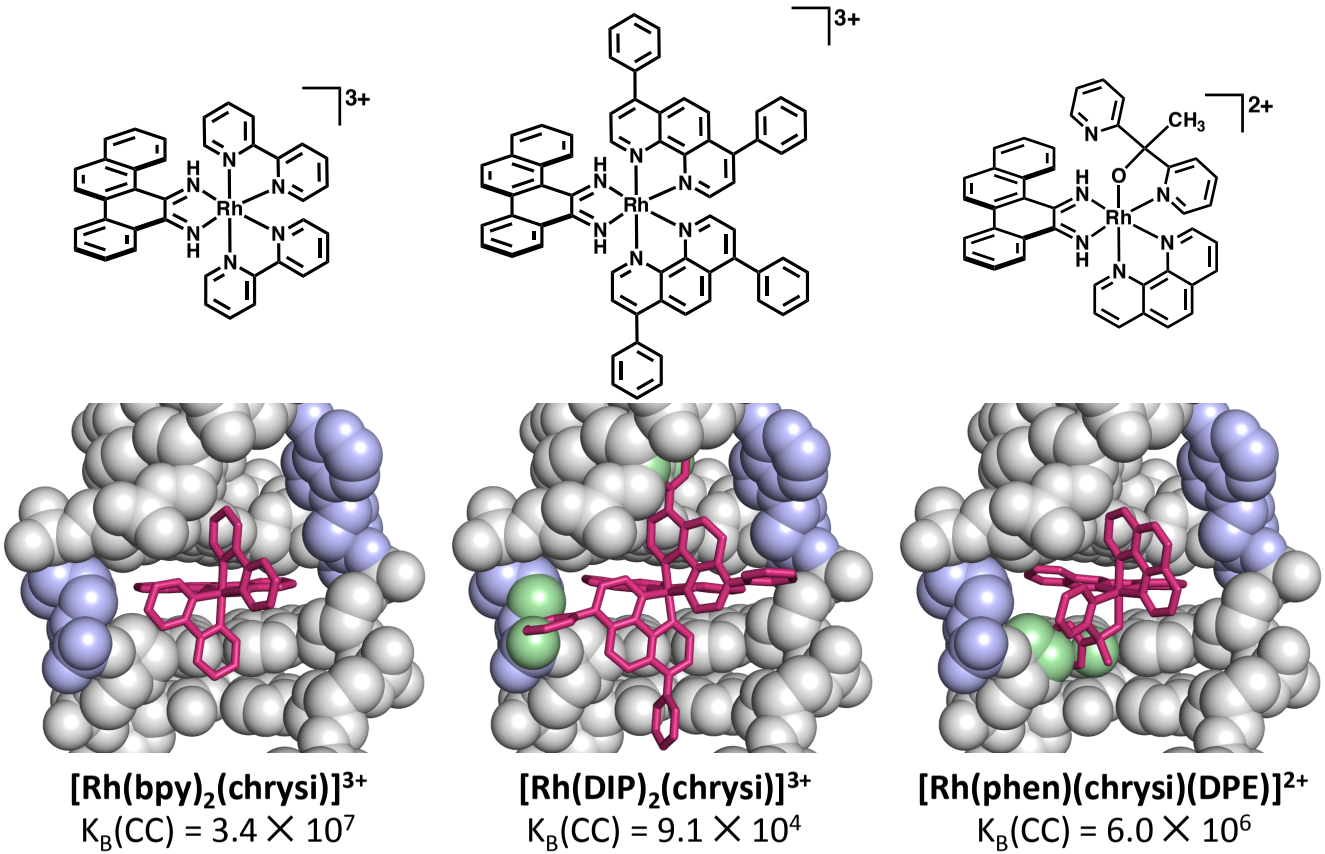

Figure 4.1 Crystal and model structures of three metalloinsertors. (Left) The crystal structure of $[Rh(bpy)_2(chrysi)]^{3+}$ bound to an AC mismatch in DNA, with the mismatch highlighted in blue. (Middle) The modeled structure of $[Rh(DIP)_2(chrysi)]^{3+}$ bound to an AC mismatch in DNA, with steric clashing highlighted in green. (Right) The modeled structure of $[Rh(phen)(chrysi)(PPO)]^{2+}$ bound to an AC mismatch in DNA. Again, steric clashing is observed and highlighted in green.

ligand and the DNA backbone, hindering DNA binding and leading to weak binding interactions.

Recently, a new generation of rhodium metalloinsertors bearing a rhodium-oxygen bond has been synthesized.[11,12] These complexes have comparable mismatch binding affinity to classic metalloinsertors, such as $[Rh(bpy)_2(chrysi)]^{3+}$, however they are up to 100-fold more toxic to cancer cells than these classic metalloinsertors. We hypothesize that this dramatic difference in potency is a result of a distinct DNA-binding interaction. While this binding interaction is likely still under the umbrella of metalloinsertion, we believe a significant distortion of the DNA helix at the metalloinsertor-bound mismatched site renders these new "Rh-O" metalloinsertors more detectable by intracellular proteins, resulting in cell death at lower concentrations of the therapeutic. This hypothesis is supported by several observations about the Rh-O metalloinsertors. First, unlike classic metalloinsertors (which only bind B-form DNA through their Δ enantiomer), both the Δ and Λ enantiomers of Rh-O metalloinsertors can bind to mismatched DNA. Additionally, altering the ancillary ligands to be sterically bulky does not dramatically influence mismatch binding affinity of Rh-O metalloinsertors. Indeed, when the Rh-O metalloinsertor $[Rh(phen)(chrysi)(DPE)]^{2+}$ is modeled into the DNA lesion that was crystallographically observed with $[Rh(bpy)_2(chrysi)]^{3+}$ we observe significant steric clashing with the DNA backbone, confirming there must be some difference in mismatch binding between these two complexes (**Figure 4.1**).[11]

Our group is currently attempting to crystallize an Rh-O metalloinsertor, $[Rh(phen)(chrysi)(PPO)]^{2+}$ (RhPPO) or $[Rh(phen)(chrysi)(DPE)]^{2+}$ (RhDPE), in the

presence of a mismatched DNA (**Figure 4.2)**. Such a structure would likely provide invaluable insight on the improved potency of the rhodium metalloinsertor. While such a structure has not yet been obtained, this chapter details the past and present efforts towards crystallizing an Rh-O metalloinsertor with mismatched DNA.

4.2 Experimental Methods

4.2.1 Materials

The metalloinsertors $[Rh(phen)(chrysi)(DPE)]^{2+}$ and $[Rh(phen)(chrysi)(PPO)]^{2+}$ were synthesized following the literature.[11,13] Oligonucleotides were purchased from IDT DNA with standard desalting. Crystallography kits and reagents were purchased from Hampton Research. Pellet Pestles (part #749520-0000) were purchased from DWK Life Sciences. SepPak C18 columns were purchased from Waters Co.

4.2.2 Purification of DNA Sequences

DNA oligonucleotides were purchased in 1-10 μmol quantities and dissolved in up to 800 μL of MilliQ water. Samples were then purified by HPLC on a C18 reverse-phase column using a gradient elution method starting at 2:98 acetonitrile:buffer and ramping up to 17:83 acetonitrile:buffer over 30 min, where the buffer is 50mM ammonium acetate in water. Analytical runs were performed before each purification using a small aliquot of the sample (< 0.1 μmol) to identify the elution time of the oligonucleotides. Following the analytical run, preparatory runs were performed such that ~1 μmol of oligonucleotides was injected into the HPLC and the center of the eluted peak was collected in a 15mL falcon tube. Samples were placed on the lyophilizer to remove the eluent, then desalted using either a C18 SepPak or ethanol precipitation, as described below.

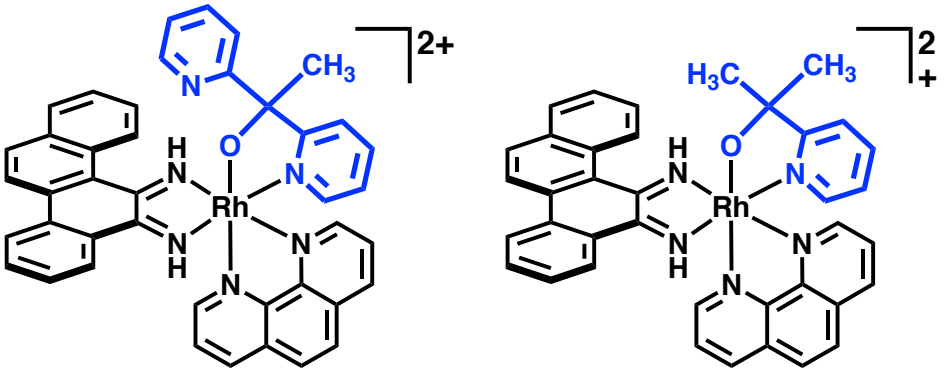

Figure 4.2 Structures of two Rh-O metalloinsertors. $[Rh(phen)(chrysi)(DPE)]^{2+}$ (**RhDPE**, left) and $[Rh(phen)(chrysi)(PPO)]^{2+}$ (**RhPPO**, right) are Rh-O metalloinsertors that appear to bind DNA mismatches through a binding mode that is distinct from classic metalloinsertors.

SepPak Desalting: A 5g SepPak was used to desalt up to 10 μmol of purified DNA. The column was pre-washed with three 20 mL aliquots of HPLC grade acetonitrile followed by three 20 mL aliquots of MilliQ water. The lyophilized DNA sample was dissolved in 5 mL of 2 M NaCl (or KCl) and loaded onto the column. The sample was then rinsed qith 5 mL of 2M NaCl, followed by 200-300 mL MilliQ water. Finally, the DNA sample was eluted with three 15 mL aliquots of 1:1 acetonitrile:water. DNA samples were again lyophilized. Once dry, samples were dissolved in a minimal amount of MilliQ water (adjusted to pH 8) and a UV-Visible spectrum taken to quantify the DNA following Beer's Law ($A = \varepsilon lc$), where ε is the extinction coefficient provided by IDT. Once quantified, samples were diluted (with MilliQ) or concentrated (by drying a known volume of sample and redissolving in the appropriate volume of MilliQ) to the appropriate concentration for crystallographic purposes.

Ethanol Precipitation: Pure ethanol and a 70:30 ethanol:water mixture were pre-cooled on dry ice in a 4 °C cold room. Lyophilized DNA samples (up to 2 μmol) were suspended in 100 μL MilliQ water, vortexed, and then centrifuge to ensure all DNA was dissolved and pooled at the bottom of the falcon tube. The DNA solution was then moved to a 1.5 mL eppendorf tube and 1 mL of cold ethanol was added to the sample and vortexed, the 50 μL of 3 M NaCl was added and samples were vortexed again. These additions resulted in some visible cloudiness of the sample. Samples were then cooled for at least 30 min at -20 °C. Samples were then centrifuged at 16,000 rcf for 30 min at 4 °C. The supernatant was removed from the DNA pellet, and the DNA pellet was rinsed/resuspended in 1mL of the 70% ethanol solution, then centrifuged again at 16,000

rcf for 5 min at 4 °C. The supernatant was again removed and the rinsing process repeated one more time. Once all liquid was decanted, the samples were completely dried on a speedvac for at least 20 min. Once dry, samples were dissolved in a minimal amount of MilliQ water (adjusted to pH 8) and a UV-Visible spectrum taken to quantify the DNA following Beer's Law ($A = \varepsilon lc$), where ε is the extinction coefficient provided by IDT. Once quantified, samples were diluted (with MilliQ) or concentrated (by drying a known volume of sample and redissolving in the appropriate volume of MilliQ) to the appropriate concentration for crystallographic purposes.

4.2.3 Diastereomeric and Enantiomeric Separation of Metalloinsertors

RhDPE and RhPPO were synthesized following the literature, however up to 50 equivalents of DIEA (N,N-diisopropylethylamine) was added to the final reaction step (addition of DPE or PPO to $[Rh(phen)(chrysi)(NH_3)_2]^{3+}$), allowing it to proceed more quickly and purely to the desired products.[11,13] Each complex was initially purified over a 10 g SepPak. The SepPak was first rinsed with 1L of methanol, followed by 500 mL of 0.1% TFA (trifluoroacetic acid, aq). The metalloinsertor was dissolved in 0.1% TFA (aq) and loaded onto the SepPak and eluted with various mixtures of acetonitrile and 0.1% TFA (aq), starting with a 5% solution of acetonitrile. The acetonitrile concentration was increased in 2.5% or 5% increments (in 100 mL intervals) until red metalloinsertor bands began to elute. Once the majority of red metalloinsertor product was eluted and collected, the remaining yellow/brown complex was eluted with 50% acetonitrile. Starting materials eluted around 15% acetonitrile, followed by product at 15% (for RhDPE) or 15-20% (for RhPPO) acetonitrile, and lastly side products began to elute at 20% (for RhDPE) or 30% (for RhPPO) acetonitrile.

4.2.3.1 Specific Methods for RhPPO

Following SepPak purification, RhPPO was purified on a C18 reverse-phase column using mixtures of acetonitrile and buffer (0.1% TFA, aqueous). RhPPO was purified using an isocratic method of 25:75 acetonitrile:buffer. This method allowed for the removal of undesired impurities, but did not allow for the separation of the two RhPPO diastereomers.

A summary of the diastereomeric and enantiomeric separation of RhPPO can be seen in **Figure 4.3**. An Astec Cyclobond column, which utilizes chiral cyclodextrin molecules to separate racemic mixtures into their enantiomers, was previously used to separate one set of enantiomers of RhPPO (see chapter 2 and reference 12). However, due to poor resolution of the enantiomers and natural degradation of the column, this method is not practical for the purification of a large amount of metalloinsertor. Instead, the Astec Cyclobond column was used only to separate the diastereomers of RhPPO. An isocratic method of 50:50 acetonitrile: 0.1 M KPF_6 (aq) was used to separate the two diastereomers (referred to as RhPPO-1 and RhPPO-2, based on elution order).

A ChiralPak IC column, which is a cellulose-based column, was used to purify each diastereomer of RhPPO into its two enantiomers. For the diastereomer that eluted first (RhPPO-1), an isocratic method utilizing 45% acetonitrile and 55% 0.1 M KPF_6 (aq) was used as it provided good separation of the two enantiomers (RhPPO-1-1 and RhPPO-1-2, based on elution order). For the diastereomer that eluted second (RhPPO-2), a method using 50% acetonitrile and 50% 0.1 M KPF_6 (aq) was used for purification into two enantiomers (RhPPO-2-1 and RhPPO-2-2, based on elution order). Purity of each enantiomer was confirmed using the ChiralPak IC column. A 50 μM sample of each

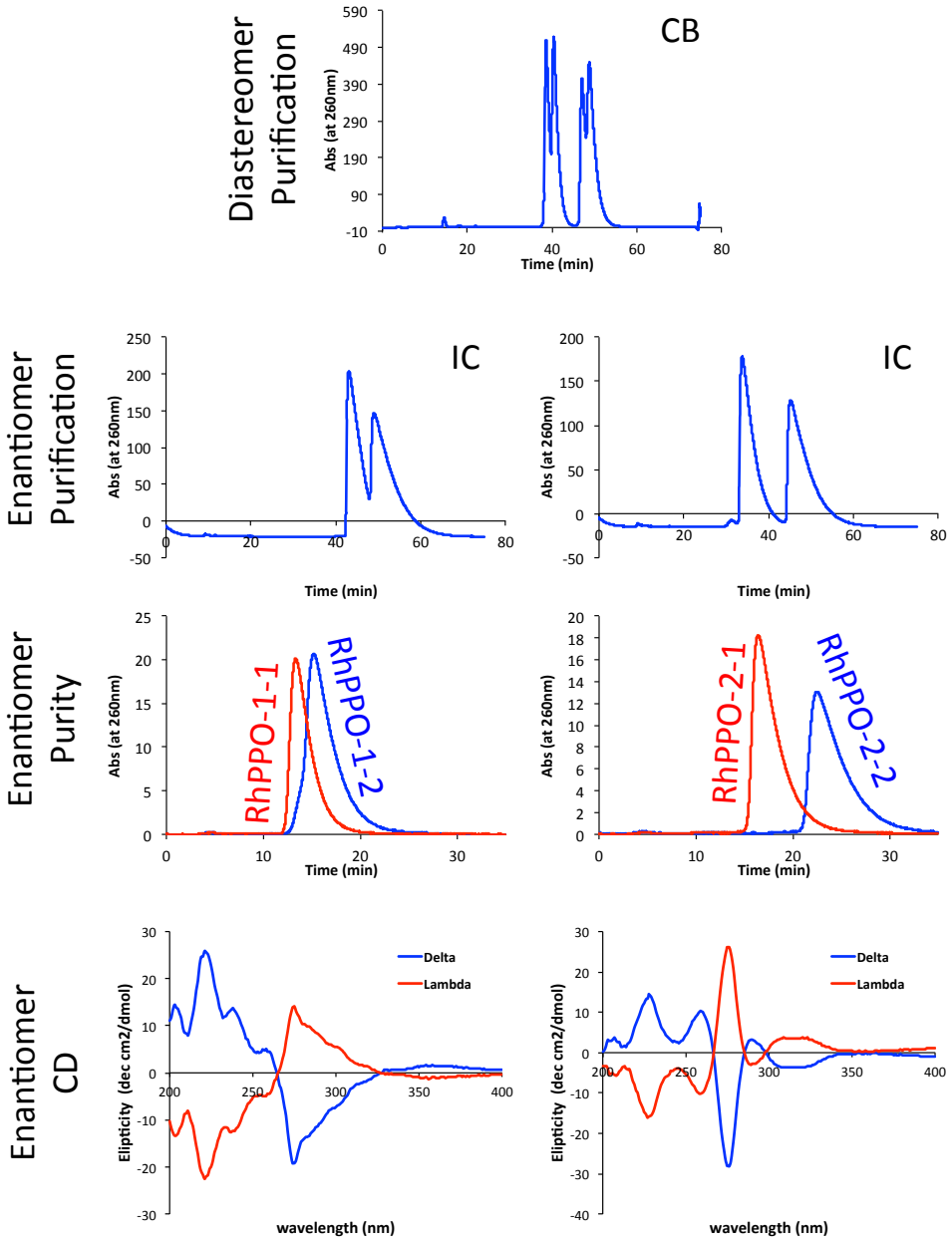

Figure 4.3 Purification scheme of RhPPO. (Top) Diastereomers are separated on a Astec Cyclobon (CB) column and (middle top) enatiomers can be separated on a ChiralPak IC (IC) column. (middle bottom) Separated enantiomers have minimal impurities and show enantiomeric behaviors by circular dichroism experiments. Enantiomers were assigned based on comparison to reference 11.

enantiomer was made in MilliQ water and examined on a Model 430 circular dichroism spectrometer (AVIV).

4.2.3.2 Specific Methods for RhDPE

A summary of the diastereomeric and enantiomeric separation of RhPPO can be seen in **Figure 4.4**. RhDPE was further purified by HPLC using a gradient method. Several different isocratic and gradient methods were attempted to find a suitable method that could separate the diastereomers of RhDPE. The method used was 15:85 acetonitrile:buffer to 25:75 over 5 min, holding at 25:75 for 5 min then ramp up to 50:50 over the next 40 min. This method allowed for the removal of undesired impurities as well as the separation of the two diastereomers (RhDPE-1 and RhDPE-2, based on elution order).

The Astec Cyclobond column was used to purify the RhDPE diastereomer that eluted second (RhDPE-2). A method utilizing 42.5% acetonitrile and 57.5% 0.1 M KPF_6 (aq) was used to separate the enantiomers (RhDPE-2-1 and RhDPE-2-2, based on elution order). The Astec Cyclobond column could not resolve the enantiomers of the first eluted diastereomer (RhDPE-1), therefore the ChiralPak IC column was used to separate these enantiomers using a method of 50% acetonitrile and 50% 0.1M KPF_6 into enantiomers (RhDPE-1-1 and RhDPE-1-2, based on elution order). Purity of each enantiomer was confirmed using the ChiralPak IC column. A 50 μM sample of each enantiomer was made in MilliQ water and examined on a Model 430 circular dichroism spectrometer (AVIV).

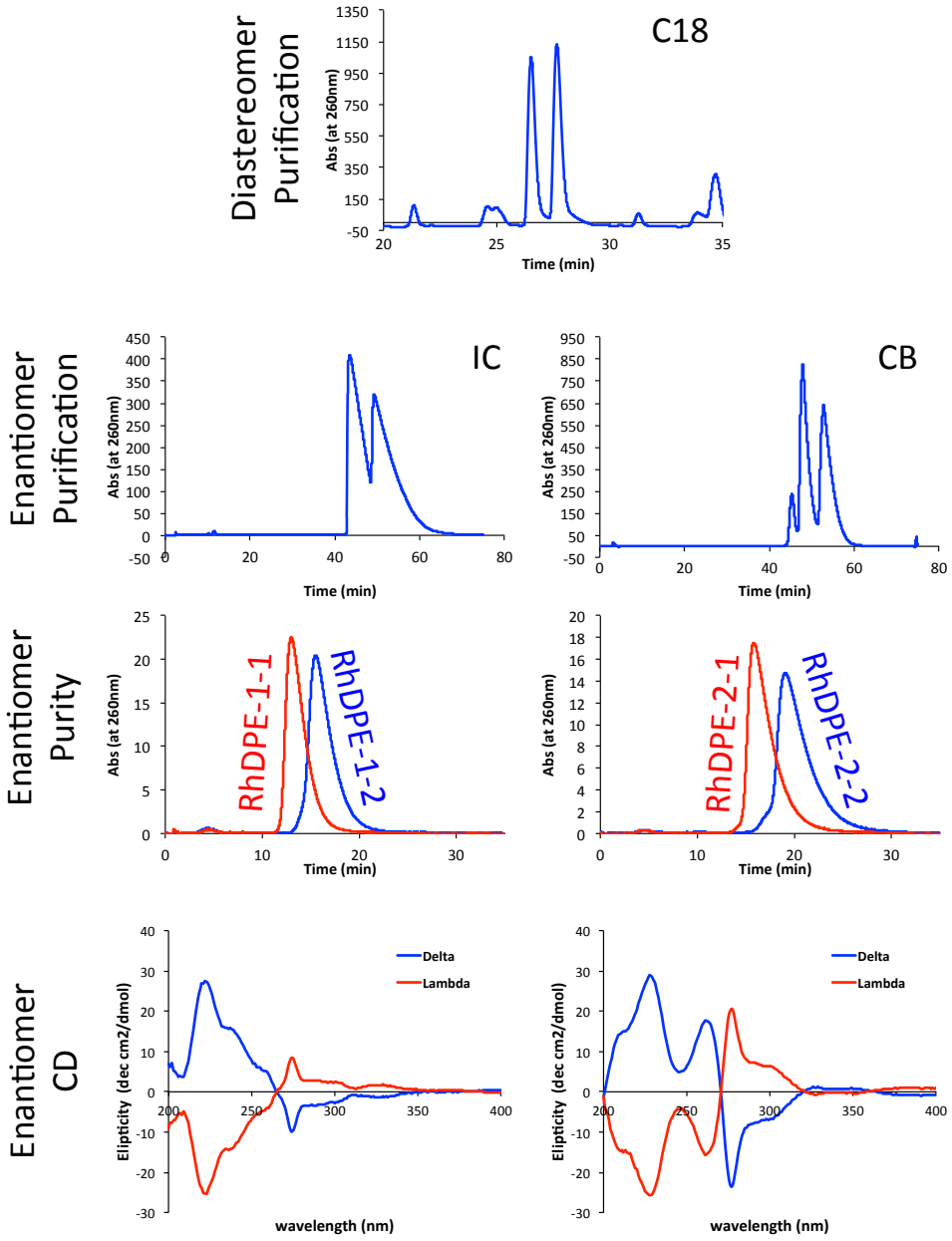

Figure 4.4 Purification scheme of RhDPE. (Top) Diastereomers are separated on a C18 column and (middle top) enatiomers can be separated on either an ChiralPak IC (IC) column or an Astec Cyclobond (CB) column. (middle bottom) Separated enantiomers have minimal impurities and show enantiomeric behaviors by circular dichroism experiments. Enantiomers were assigned based on comparison to reference 11.

4.2.4 Crystallographic Methods

4.2.4.1 General Crystal Tray Setup

Crystal trays were set up using either a 24-well or 96-well plate format. For the 24-well plate format, the Hampton Research Mini Nucleic Acid Screen, which includes 24 unique buffers, was used (**Table 4.1**). In these experiments, the well of the 24-well plate was filled with 1 mL of a 35% MPD solution, which serves as the precipitant. Next, 2 μL of a kit buffer and 2 μL of a metalloinsertor-DNA mixture were combined on the platforms of a 24-well sitting drop plate. The metalloinsertor-DNA mixture could be pre-mixed and filtered or mixed in the well by combining 1 μL of a metalloinsertor mixture with 1 μL of a DNA mixture (with or without pipette mixing). Specific details will be given in the results and discussion section for each experiment. Plates were sealed with packaging tape and stored at room temperature in the dark. Wells were checked for crystal growth every week for one month, then once a month.

For the 96-well plate format, the Hampton Research Natrix HT screen, which contains 96 buffer conditions, was used. The well of the 96-well plate was filled with 50 μL of a kit buffer using an Art Robbins Gryphon Nano. The plate was then equilibrated to 4 °C and a TTP Mosquito was used to combine 200 nL of kit buffer (from the well) with 200 nL of a pre-mixed metalloinsertor-DNA solution on the platform of the 96-well sitting drop plate. Plates were sealed with packaging tape and stored at 4 °C in the dark. Well were checked for crystal growth every week for one month, then once a month.

4.2.4.2 Crystal Tray Setup Using Seeding Crystals

Crystal seeding experiments were employed once in attempts to grow single crystals from poorly-ordered parent crystals. Fresh seeding buffers were made to match

Table 4.1 Buffer conditions for the Hampton Research Nucleic Acid Mini Screen used in crystallographic experiments

Kit Buffer	Precipitant [a]	Buffer [b]	Polyamine	Monovalent Ion	Divalent Ion [c]
1	10% MPD	40 mM NaCAC, pH 5.5	20 mM $[Co(NH_3)_6]Cl_3$		20 mM $MgCl_2$
2	10% MPD	40 mM NaCAC, pH 5.5	20 mM $[Co(NH_3)_6]Cl_3$	80 mM NaCl	20 mM $MgCl_2$
3	10% MPD	40 mM NaCAC, pH 5.5	20 mM $[Co(NH_3)_6]Cl_3$	12 mM NaCl, 80 mM KCl	
4	10% MPD	40 mM NaCAC, pH 5.5	20 mM $[Co(NH_3)_6]Cl_3$	40 mM LiCl	20 mM $MgCl_2$
5	10% MPD	40 mM NaCAC, pH 6.0	12 mM Spermine 4HCl	80 mM KCl	20 mM $MgCl_2$
6	10% MPD	40 mM NaCAC, pH 6.0	12 mM Spermine 4HCl	80 mM KCl	
7	10% MPD	40 mM NaCAC, pH 6.0	12 mM Spermine 4HCl	80 mM NaCl	20 mM $MgCl_2$
8	10% MPD	40 mM NaCAC, pH 6.0	12 mM Spermine 4HCl	80 mM NaCl	
9	10% MPD	40 mM NaCAC, pH 6.0	12 mM Spermine 4HCl	80 mM NaCl, 12 mM KCl	20 mM $MgCl_2$
10	10% MPD	40 mM NaCAC, pH 6.0	12 mM Spermine 4HCl	12 mM NaCl, 80 mM KCl	
11	10% MPD	40 mM NaCAC, pH 6.0	12 mM Spermine 4HCl	80 mM NaCl	20 mM $BaCl_2$
12	10% MPD	40 mM NaCAC, pH 6.0	12 mM Spermine 4HCl	80 mM KCl	20 mM $BaCl_2$
13	10% MPD	40 mM NaCAC, pH 6.0	12 mM Spermine 4HCl		80 mM $SrCl_2$
14	10% MPD	40 mM NaCAC, pH 7.0	12 mM Spermine 4HCl	80 mM KCl	20 mM $MgCl_2$
15	10% MPD	40 mM NaCAC, pH 7.0	12 mM Spermine 4HCl	80 mM KCl	
16	10% MPD	40 mM NaCAC, pH 7.0	12 mM Spermine 4HCl	80 mM NaCl	20 mM $MgCl_2$
17	10% MPD	40 mM NaCAC, pH 7.0	12 mM Spermine 4HCl	80 mM NaCl	
18	10% MPD	40 mM NaCAC, pH 7.0	12 mM Spermine 4HCl	80 mM NaCl, 12 mM KCl	20 mM $MgCl_2$
19	10% MPD	40 mM NaCAC, pH 7.0	12 mM Spermine 4HCl	12 mM NaCl, 80 mM KCl	
20	10% MPD	40 mM NaCAC, pH 7.0	12 mM Spermine 4HCl	80 mM NaCl	20 mM $BaCl_2$
21	10% MPD	40 mM NaCAC, pH 7.0	12 mM Spermine 4HCl	80 mM KCl	20 mM $BaCl_2$
22	10% MPD	40 mM NaCAC, pH 7.0	12 mM Spermine 4HCl	40 mM LiCl	80 mM $SrCl_2$, 20 mM $MgCl_2$
23	10% MPD	40 mM NaCAC, pH 7.0	12 mM Spermine 4HCl	40 mM LiCl	80 mM $SrCl_2$
24	10% MPD	40 mM NaCAC, pH 7.0	12 mM Spermine 4HCl		80 mM $SrCl_2$, 20 mM $MgCl_2$

[a] MPD = (+/-)-2-Methyl-2,4-pentanediol
[b] NaCAC = Sodium cacodylate trihydrate
[c] $MgCl_2$ from magnesium chloride hexahydrate

the well solution of the parent crystal; the same salts, buffers, and pH as the original kit buffers were used but the concentration of precipitant was increased to match the well concentration (35% MPD), as the drop should have equilibrated to 35% over time. Buffer matching should prevent the crystal from dissolving in the new buffer solution. The parent crystals were extracted from their wells using a cryoloop tool and placed into 10 μL of the fresh seeding buffer on a microscope slide. If undesired material was transferred with the parent crystal, the parent crystal was separated from the undesired material and moved again to fresh seeding buffer. The crystal was then manually crushed with a high-gauge needle and transferred to a pellet pestle (microcentrifuge tube + grinder) using a pipette. The microcentrifuge tube was filled to a volume of 40-50 μL of seeding buffer, then the crystal was further crushed using by inserting the pestle into the tube and moving the pestle up and down and periodically vortexing. In a new plate, 1.5 μL of a metalloinsertor-DNA stock was combined with 1 μL kit buffer. After a 3 day equilibration, 0.5 μL of the seed stock. Plates were sealed and stored as described above.

4.2.4.3 Crystal Harvesting

When viable crystals were identified, there were collected using the following general procedures. To collect a crystal from a well, a razor blade was used to remove the packaging tape covering the well of interest and a flap of fresh, easily replaceable packaging place was placed over the well. Crystals were scooped out of the well using a crystal loop affixed to a magnetic crystal wand. Loops of different sizes were selected to be slightly larger than the crystal being collected, but generally size 2 or 3 loops (0.05-0.2 mm) were used to collect the crystals. Sometimes an acupuncture needle was used to clear unwanted crystals or substances away from the crystal of interest. Once collected,

crystals were immediately plunged into liquid nitrogen and stored in cryo-vials. In addition to being a crystallographic precipitant, MPD is also a cryo-protectant, therefore no additional cryoprotection was necessary. Cryo-vials were affixed to a rack and stored in liquid nitrogen until beamtime was available. When beamtime was available the cryo-loops were transferred to a large cassette that can be screened using automated software at the SLAC beamline.

4.3 Results and Discussion

4.3.1 Efforts Towards Crystallization of a Rh-O Metalloinsertor with Mismatched DNA

As the crystallographic experiments described herein are ongoing, the attempts at crystallography and lessons learned from those attempts are detailed below in chronological order. Details on why certain methods were attempted, why certain procedure modifications were made, and the successes/failures that resulted will be described for each experimental setup.

4.3.1.1 Preliminary Crystallography Experiments

Initial crystallography experiments were performed solely with RhPPO-2-1 and RhPPO-2-2, as those enantiomers were the first RhPPO enantiomers to be purified (see chapter 2). Two self-complementary sequences containing two internal mismatches were used in these initial experiments, 5'-CGG**A**AATT**A**CCG-3' (**AA**, mismatch bolded and underlined) and 5'-CGG**A**AATT**C**CCG-3' (**AC**, mismatch bolded and underlined). These oligonucleotides were selected as the Barton group has previously had success crystallizing the metalloinsertor $[Rh(bpy)_2(chrysi)]^{3+}$ and $[Ru(bpy)_2(dppz)]^{2+}$ with these sequences.[8,14,15] It is of note that $[Rh(bpy)_2(chrysi)]^{3+}$ was crystallized with the **AA**

sequence in two buffer conditions that differ solely in the included monovalent cation salt, NaCl or KCl. The crystal obtained from the sodium-containing buffer contained two metalloinsertors bound through metalloinsertion at the mismatched sites. The crystal obtained from the potassium-containing buffer had these same two metalloinsertors bound; however an additional metalloinsertor bound through intercalation was observed at the centroid of the DNA duplex. Due to this stark difference in crystal form, both the sodium and potassium salts of DNA were used in these preliminary experiments.

Drops with final concentrations of 2 mM ssDNA (**AA**-K^+, **AA**-Na^+, **AC**-K^+, and **AC**-Na^+) and 2 mM of RhPPO-2-1 or RhPPO-2-2 were made. Higher concentrations of RhPPO stock solutions were attempted but were not possible due to solubility limitations. ssDNA and RhPPO stock solutions (8 mM) were pre-mixed in a 1:1 ratio. Variable amounts of precipitate formed upon mixing, and precipitate was removed through a 0.45 μm spin filter. These mixtures were combined with each of the 24 Hampton Research Nucleic Acid Mini Screen buffers either with or without pipette mixing of the resultant drop. Most plates were kept at room temperature, however some plates were held at 4° C. After several months, a variety of morphologies became visible, including precipitate, microcrystals, phase separations, quasi-crystals, and films (**Figure 4.5**). Sometimes crystals were also present; however most frequently these crystals were colorless, indicating no metalloinsertor was present in the crystal. Several disordered, low-resoltion crystalline samples were collected and used for additional seeding experiments. No colored (indicating metalloinsertor presence) single crystals were obtained from these experiments.

In order to screen a wider range of buffer conditions, additional preliminary

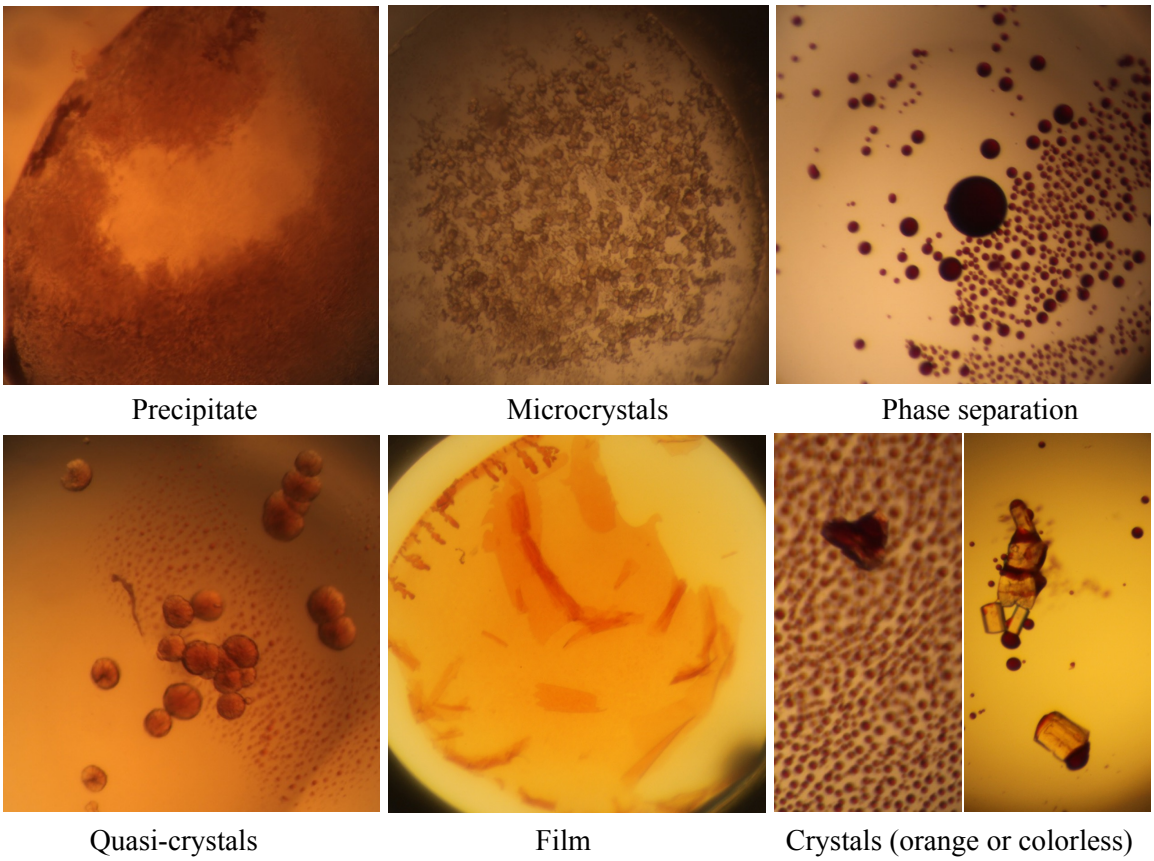

Figure 4.5 Morphologies commonly observed in crystallography experiments. A variety of different crystalline substances formed in preliminary experiments. None of the crystals that formed were both colored (indicating presence of metalloinsertor) and well-ordered.

experiments were performed using the Natrix HT screen, which contains 96 distinct buffers. This kit has the additional benefit of requiring a smaller sample volume, therefore testing these additional conditions does not require additional material. Drops with a final concentration of 2 mM ssDNA (**AA**-K^+, **AA-**Na^+, **AC**-K^+, or **AC**-Na^+) and 2 mM RhPPO-2-1 or RhPPO-2-2 were set up. These trays were set up and kept in a 4° C cold room. No crystals were observed in these experiments. Although the buffers were similar to those used in the Nucleic Acid Mini Screen, they differed in that the Nucleic Acid Mini Screen includes the polyamine spermine, which can help facilitate the crystallization of DNA sequences. Therefore additional experiments were carried out using the Natrix HT 96-well format, but with the addition of spermine (to a final concentration of 1 mM). Again, no single crystals were observed from these plates, though some crystalline material was produced. Buffer screens in which the pH and precipitant concentration were varied were performed around the buffer conditions that produced promising crystalline material under multiple different DNA-metalloinsertor conditions (see **Table 4.2** for an example of these screens). Theses screenings were performed using a 24-well plate format instead of a 96-well format as the larger amount of material can allow for larger crystal growth.

Overall, these preliminary experiments did not produce any promising results or difractable crystals. There are several reasons this likely occurred. These experiments were carried out using the same methods that had previously been successful in crystallizing metalloinsertors, however RhPPO and $[Rh(bpy)_2(chrysi)]^{3+}$ are different compounds with different properties. Specifically, at concentrations of 2 mM (the final concentration of each crystallography experiment), RhPPO and mismatch DNA

Table 4.2 Example of a pH and precipitant screen around a promising buffer condition.*

pH 5 41 % MPD	pH 5.5 41 % MPD	pH 6 41 % MPD	pH 6.5 41 % MPD	pH 7 41 % MPD
pH 5 43 % MPD	pH 5.5 43 % MPD	pH 6 43 % MPD	pH 6.5 43 % MPD	pH 7 43 % MPD
pH 5 45 % MPD	pH 5.5 45 % MPD	pH 6 45 % MPD	pH 6.5 45 % MPD	pH 7 45 % MPD
pH 5 47 % MPD	pH 5.5 47 % MPD	pH 6 47 % MPD	pH 6.5 47 % MPD	pH 7 47 % MPD
pH 5 50 % MPD	pH 5.5 50 % MPD	pH 6 50 % MPD	pH 6.5 50 % MPD	pH 7 50 % MPD

* Original buffer condition was F8 from the Natrix HT screen: 80 mM NaCl, 20 mM $BaCl_2$, 40 mM sodium cacodulate tryhydrate, pH 6.0, 45% MPD, 12 mM spermine tetrahydrochloride.

precipitate with each other to a sometimes significant extent. In the above-described experiments, precipitate was removed using a spin filter, as solid precipitate in each well would likely interfere with single crystal growth. This precipitate removal, however, significantly reduces RhPPO and DNA concentration and further makes those concentrations unknown and non-reproducible. As such, future methods were aimed at minimizing precipitation by using lower concentrations and altering the DNA sequences to see if precipitation has a length or sequence dependence.

4.3.1.2 Screening DNA Sequences

It was hypothesized that the preliminary crystallography attempts described in section **4.3.1.1** were futile due to significant precipitation of the DNA and metalloinsertor solutions upon mixing. As these new Rh-O metalloinsertors are significantly more potent, it seems possible that this precipitation may be reflective of the difference in how they bind to mismatched DNA—that is, perhaps a great enough distortion or significant helical unwinding occurs that results in aggregation and precipitation of the DNA helix. It was therefore hypothesized that this precipitation may be prevented by using (1) different DNA mismatches that interact with metalloinsertors to different extents based on their thermodynamic destabilization, (2) larger spaces between the two mismatched sites to allow more room for the metalloinsertor to unwind, bend, or otherwise interact with the DNA, and (3) to incorporate only a single DNA mismatch in the sequence to reduce the overall concentration of mismatches. Furthermore, exploring different DNA sequences is desirable, as DNA crystallography generally focuses on altering DNA sequences instead of altering buffer conditions when screening experimental setups.

The Nucleic Acid Data Bank (NDB) was used to identify DNA sequences and

buffer conditions that seemed most likely to be successful in crystallography. The NDB was searched for structures that contained drug interactions and that were solved by x-ray crystallography (as opposed to NMR solution structures). This pool was further narrowed down to include only drug molecules that interacted non-covalently and through intercalation, which is a well-studied binging mode that is similar to metalloinsertion. The buffer conditions and concentrations were extracted from the source literature of each structure and compiled to identify common successful motifs in drug-DNA crystallography (see **Table 4.3**). From this list, the DNA sequences or motifs that occurred most frequently were identified and modified to contain one or two mismatched sites (**Table 4.4**). Precipitation experiments (combining DNA with RhPPO and no buffer) were performed stock solutions of 2-8 mM RhPPO and 4 mM ssDNA. No consistent precipitation was observed at 4 mM or lower concentrations of RhPPO, suggesting precipitation observed in the preliminary experiments was likely due to the high stock concentrations (8 mM) of RhPPO and ssDNA.

With this knowledge, new 24-well crystal trays were set up using the RhDPE-2 enantiomers (RhDPE-2-1, RhDPE-2-2) and the sequences listed in **Table 4.4**. Instead of using the 24 buffers included in the Nucleic Acid Mini Screen, only two buffer conditions were used as attempting all 30 DNA sequences with 24 different buffers would require an excessive amount of metalloinsertor. The buffer conditions used are shown are #15 and #17 in **Table 4.1**, which were previously crystallized with $[Rh(bpy)_2(chrysi)]^{3+}$. Concentrations of DNA and metalloinsertor were dramatically reduced in these experiments. For RhDPE experiments, final concentrations of 1 mM ssDNA and a 1:1 (for buffer #15) or 2:3 (for buffer #17) mismatch:RhDPE molar ratio

Table 4.3 DNA sequences that have been crystallized with intercalating drug molecules and their PDB/NDB identification code

PDB/NDB ID	Drug Molecule	DNA Sequence
5JEU	Delta-[$Ru(phen)_2(dppz)]Cl_2$	TCGGCGCCGA
4YMC	$[Ru(phen)_2(dppz)]Cl_2$	CCGGTACCGG
NA2705	Variolin B	CGTACG
NA0614, NA0626	Sanguinarine	CGTACG
DD0103	proflavine	CGATCG
DD0108, DD0109	$Rh(bpy)_2(chrysi)Cl_3$	CGGAAATTACCG
DD0088	$Rh(bpy)_2(chrysi)Cl_3$	CGGAAATTCCCG
DD0073	enchinomycin	ACGTACGT
DD0064, DD0065	anthriquinone derivative	CGTACG
DD0070	ellipticine	CGATCG
DD0061	disaccharide anthracycline MAR20	CGATCG
DD0062	topoisomerase inhibitor	CGTACG
DD0051	5Br-9amino-DACA	CGTACG
DD0041	daunomycin	CGATCG
DDF074	DACA	CG(5-BrU)ACG
DD0054	disaccharide anthracycline MEN10755	CGATCG
DD0053	Actinomycin D	ATGCTGCAT
DD0037	acridine-peptide	CGCGAATTCGCG
DD0048	DACA	CGTACG
DD0047	cryptoiepine	CCTAGG
DD0039	Actinomycin D	CGATCGATCG
DD0032	acridine-4-carboxamide	CGTACG
DD0033	acridine-4-carboxamide	CG(BrU)ACG
DD0028, DD0029	misacridine	CGTA(BrC)G
DDF064	nogalamycin	TGTAACA

Table 4.4 Sequences used in crystallography experiments, designed from off literature examples.

Name	Sequence (5'-xxx-3')	Length (bp)	# MM	MM	Design Rationale
Oligo 1	CGT**C**ACG	7	1	CC	Based off 5'-CGTACG-3', which has been crystallized with many intercalators. Adapted to have a single mismatch at its center.
Oligo 2	CGT**A**ACG	7	1	AA	
Oligo 3	CGT**T**ACG	7	1	TT	
Oligo 4	CGGA**C**TCCG	9	1	CC	An intermediate sequence between oligos 1-3 and oligos 10-12
Oligo 5	CGGA**A**TCCG	9	1	AA	
Oligo 6	CGGA**T**TCCG	9	1	TT	
Oligo 7	ATGC**C**GCAT	9	1	CC	Based off 5'-ATGCTGCAT-3', which is a mismatch-containing sequence crystalized previously with actinomycin D. Adapted to contain different mismatches
Oligo 8	ATGC**A**GCAT	9	1	AA	
Oligo 9	ATGC**T**GCAT	9	1	TT	
Oligo 10	CCGGT**C**ACCGG	11	1	CC	Based off5'-CCGGTACCGG-3', which was crystallized previously with an octahedral ruthenium complex.
Oligo 11	CCGGT**A**ACCGG	11	1	AA	
Oligo 12	CCGGT**T**ACCGG	11	1	TT	
Oligo 13	CGCGAA**C**TTCGCG	13	1	CC	Based off the well-characterized Dickerson-Drew sequence (5'-CGCGAATTCGCG-3'), adapted to contain a central mismatch.
Oligo 14	CGCGAA**A**TTCGCG	13	1	AA	
Oligo 15	CGCGAA**T**TTCGCG	13	1	TT	
Oligo 16	CGG**C**AATT**C**CCG	12	2	CC	Based off the sequences 5'-CGGAAATTACCG-3' and 5'-CGGAAATTCCCG'3', which were crystallized with metalloinsertors previously. Adapted to include untested mismatches.
Oligo 17	CGG**T**AATT**T**CCG	12	2	TT	
Oligo 18	CGG**T**AATT**C**CCG	12	2	CT	
Oligo 19	CGCG**A**AATT**A**CGCG	14	2	AA	Based off the well-characterized Dickerson-Drew sequence (5'-CGCGAATTCGCG-3'), adapted to contain two mismatchs.
Oligo 20	CGCG**A**AATT**C**CGCG	14	2	AC	
Oligo 21	CGCG**C**AATT**C**CGCG	14	2	CC	
Oligo 22	CGCG**T**AATT**T**CGCG	14	2	TT	
Oligo 23	CGG**AT**CCGGA**A**CCG	14	2	AA	Based off the sequences 5'-CGGAAATTACCG-3' and 5'-CGGAAATTCCCG'3', which were crystallized with metalloinsertors previously. Adapted to include a larger break between mismatched sites.
Oligo 24	CGG**A**TCCGGA**C**CCG	14	2	AC	
Oligo 25	CGG**C**TCCGGA**C**CCG	14	2	CC	
Oligo 26	CGG**T**TCCGG**A**TCCG	14	2	TT	
Oligo 27	CGG**A**TCGA**A**CCG	12	2	AA	Based off the sequences 5'-CGGAAATTACCG-3' and 5'-CGGAAATTCCCG'3', which were crystallized with mismatches previously. Adapted to alter the sequence between the mismatched sites..
Oligo 28	CGG**C**TCGA**A**CCG	12	2	AC	
Oligo 29	CGG**C**TCGA**C**CCG	12	2	CC	
Oligo 30	CGG**T**TCGA**T**CCG	12	2	TT	

were used in each experiment. Similar setups were attempted with RhPPO, but significant precipitation was an issue even at reduced concentrations. Experiments with RhDPE produced a variety of promising crystal morphologies, including orange hexagons (**Figure 4.6**). These crystals were screened on the SLAC synchrotron beamline. Some diffraction was observed, although resolution was low. Diffraction patterns were observed out to 8Å, and fiber diffraction of the DNA helix was sometimes observed from 3.3-3.5Å, reflecting the spacing between base pairs in the DNA helix (**Figure 4.6**).

Under all conditions tested, the sequence 5'-CGG**T**AATT**C**CCG-3' produced some form of crystalline solid, including in one case an orange hexagonal crystal. As such, additional variations of this sequence (different mismatches, different lengths, a hairpin, and sequences with sticky ends) were designed and used in additional experiments (**Table 4.5**). New 24-well crystal trays were set up using all eight enantiomers (RhDPE-1-1, RhDPE-1-2, RhDPE-2-1, RhDPE-2-2, RhPPO-1-1, RhPPO-1-2, RhPPO-2-1, RhPPO-2-2) and the sequences listed in **Table 4.5**. Again, only two buffer conditions were used. Some crystalline products were produced from these screens but none resulted in single crystals.

From these experiments, it seems clear that the use of a 12-base pair palindromic sequence containing two mismatches is preferable for crystallographic experiments. Almost none of the sequences containing a single mismatch produced crystalline products, and shorter and longer sequences were also minimally successful. Future efforts were therefore focused on only these 12-mer sequences, but with variations primarily in the mismatch identity.

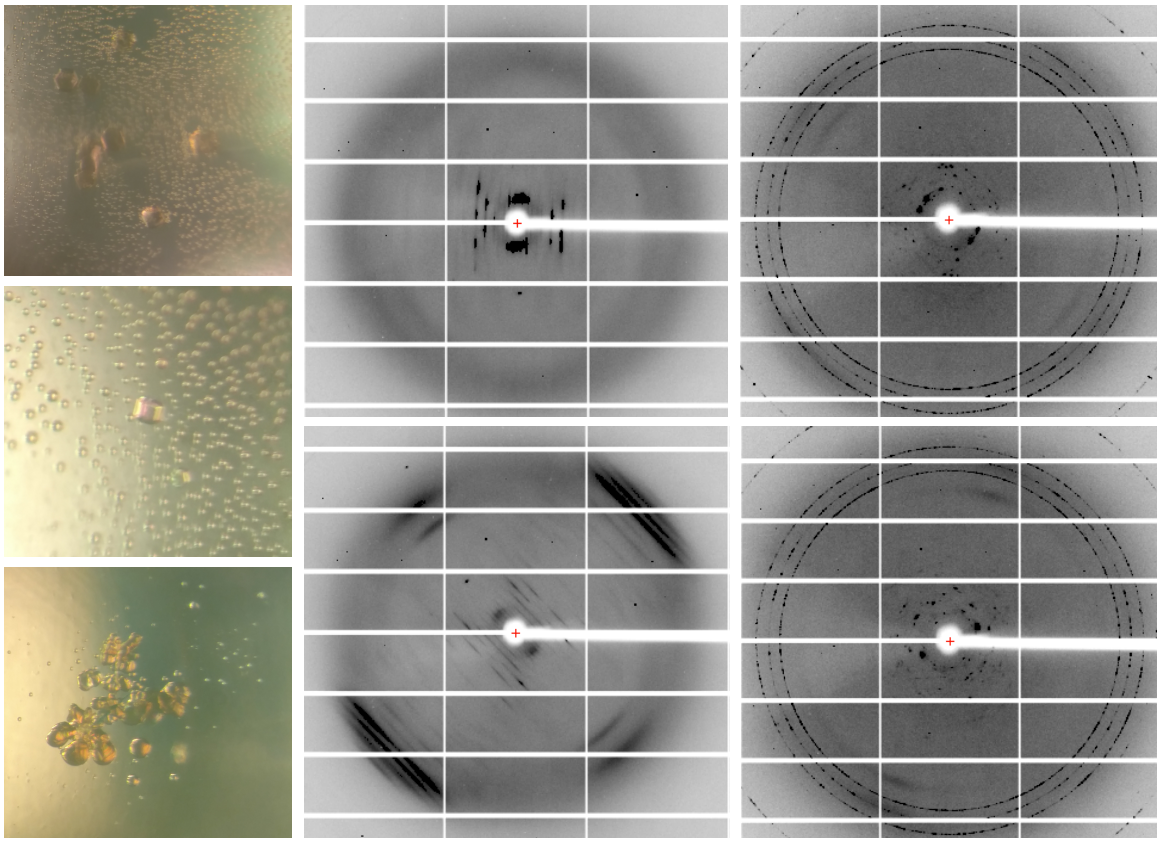

Figure 4.6 Example crystal morphologies and diffraction patterns from sequence variation experiments. (Left) Orange hexagonal crystals, cubic crystals, and amorphous crystalline solids were observed under various buffer conditions. (Middle) An example of a diffraction pattern from a hexagonal crystal at 0° and 90° rotations. Fiber diffraction from the DNA is observed as large black lines around 3.4 Å. (Right) Another example of a diffraction pattern from a hexagonal crystal at 0° and 90° rotations. Significant ice buildup is seen as concentric rings.

Table 4.5 Sequences used in crystallography experiments based off promising experiments with 5'-CGG**T**AATT**C**CCG-3' .

Name	Sequence (5'-xxx-3')	Length (bp)	# MM	MM	Sequence Rationale
Oligo 2.1	CGG**T**AATT**C**CCG	12	2	TC	Preliminarily Promising
Oligo 2.2	CGG**C**AATT**T**CCG	12	2	CT	Varied Mismatch
Oligo 2.3	CGGTAATTTCCG	12	2	TT	Varied Mismatch
Oligo 2.4	CGGCAATTCCCG	12	2	CC	Varied Mismatch
Oligo 2.5	CGGAAATTCCCG	12	2	AC	Varied Mismatch
Oligo 2.6	CGGAAATTACCG	12	2	AA	Varied Mismatch
Oligo 2.8	CGGTTCCGGACCCG	14	2	TC	Longer sequence, varied center
Oligo 2.9	CGGTTAATTACCCG	14	2	TC	Longer sequence
Oligo 2.10	GGCCGGCTTTTTGCCCGCC	19	1	CT	Hairpin sequence
Oligo 2.11a Oligo 2.11b	AACGGTAATTCGGC TTGCCTAATTCCCG	14	1	TC	AA/TT sticky end
Oligo 2.12a Oligo 2.12b	CCGGTAATTCGGC GGCCTAATTCCCG	13	1	TC	G/C sticky end
Oligo 2.13	CGGTAGCTCCCG	12	2	TC	Varied center
Oligo 2.14	GCATAATTCTGC	12	2	TC	Varied end caps
Oligo 2.15	ATGTAATTCCAT	12	2	TC	Varied end caps
Oligo 2.16a Oligo 2.16b	CGTCAGTATG CATCCTGACG	10	1	TC	Asymmetric sequence

4.3.1.3 Screening Buffer Conditions

Due to the original success of 5'-CGG**T**AATT**C**CCG-3' in kit buffers #15 and #17, a full buffer screen was performed using 5'-CGG**T**AATT**C**CCG-3' and all eight metalloinsertor enantiomers (RhDPE-1-1, RhDPE-1-2, RhDPE-2-1, RhDPE-2-2, RhPPO-1-1, RhPPO-1-2, RhPPO-2-1, RhPPO-2-2). Plates containing RhDPE were set up at a final concentration of 1 mM ssDNA and 1 mM RhDPE, and plates containing RhPPO were set up at final concentrations of 0.5 mM ssDNA and 0.5 mM RhPPO (due to RhPPO precipitating with DNA at lower concentrations than RhDPE). Orange rods, plates, and hexagonal crystals were grown from a variety of different metalloinsertor and buffer conditions, including many orange hexagons. These crystals were screened on the SLAC synchrotron beamline. In many cases diffraction was observed, however resolution was generally low, with diffraction out to 8Å and some fiber diffraction of the DNA helix (**Figure 4.7**). For the orange hexagonal crystals, however, excellent diffraction was observed and full data sets were collected on these crystals. Unfortunately, despite the orange hue of these crystals, the crystal structure contained only mismatched DNA and no metalloinsertor. The structure is described in more detail below in section **4.3.2**. The orange hue, therefore, was hypothesized to either be metalloinsertor in solvent channels of the crystal or the inclusion of very few metalloinsertor-bound DNA molecules within the crystal. These results suggest that use of buffer conditions containing a large divalent ion such as barium should be used with caution.

4.3.1.4 Screening Different DNA:Metalloinsertor Ratios

It was hypothesized that the lack of DNA in the crystal described in section **4.3.1.3** was due to low metalloinsertor loading into the DNA. As such, in future

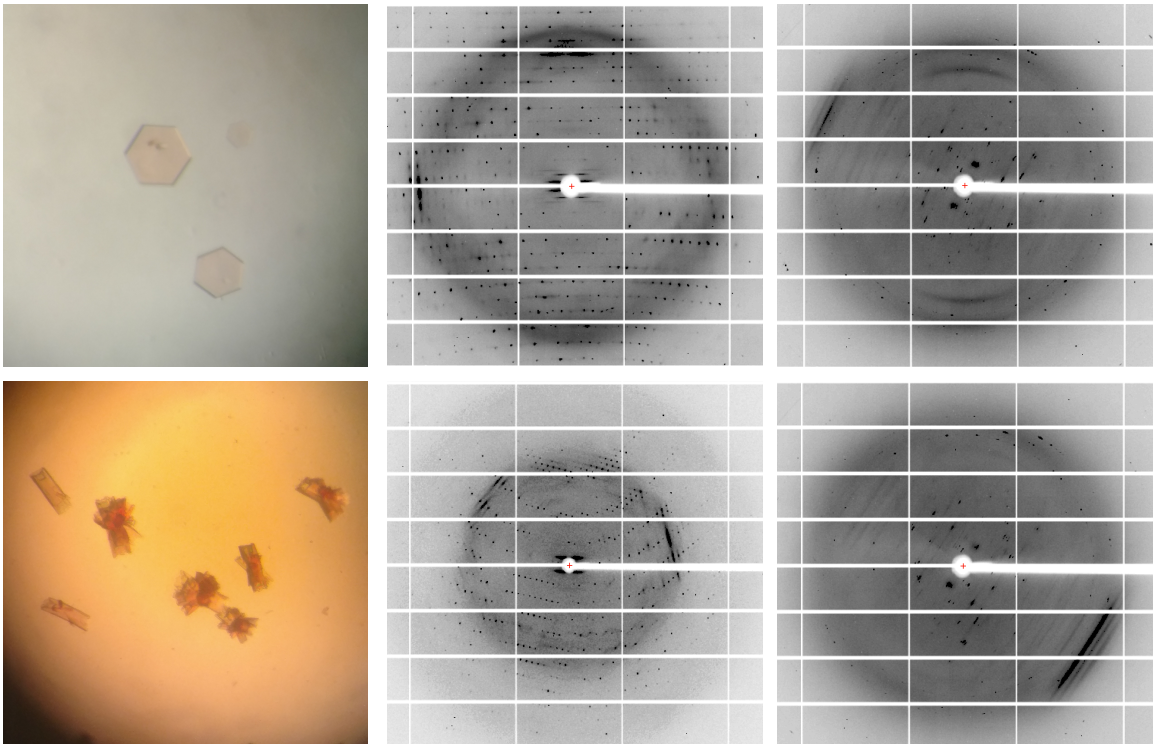

Figure 4.7 Example crystal morphologies and diffraction patterns from a buffer screening experiment. (Left) Orange hexagonal crystals and rod-shaped crystals. (Middle) An example of a diffraction pattern from a hexagonal crystal at 0° and 90° rotations. Diffraction was high enough resolution to determine a structure, but the structure contained only DNA. (Right) Another example of a diffraction pattern from a rod-shaped crystal at 0° and 90° rotations.

experiments, higher concentrations of metalloinsertor were used. Again, a full buffer screen of 5'-CGG**T**AATT**C**CCG-3' was performed using all eight metalloinsertor enantiomers (RhDPE-1-1, RhDPE-1-2, RhDPE-2-1, RhDPE-2-2, RhPPO-1-1, RhPPO-1-2, RhPPO-2-1, RhPPO-2-2). All plates were set up to a final concentration of 0.25 mM ssDNA and 1 mM RhDPE or RhPPO. After several weeks, many rich orange hexagons and red rod-shaped crystals were observed. These crystals were screened on the SLAC synchrotron beamline. In many cases diffraction was observed. Resolution remained low, but the diffraction spots that did exist were markedly more abundant and less smeared than previous crystallography attempts, suggesting using higher levels of rhodium is an extremely promising strategy (**Figure 4.8**).

4.3.1.5 Recommendations for Future Crystallographic Experiments

There are several directions that new crystallographic experiments may explore. First, the simplest next step will be to return to the well-studied sequences we have previously crystallized (5'-CGG**A**AATT**A**CCG-3' and 5'-CGG**A**AATT**C**CCG-3').[8,14] These sequences were used in early crystallography experiments, but experiments were hindered due to significant precipitation upon DNA-metalloinsertor mixing. For this reason, these sequences were abandoned and new sequences were explored, and during experiments with new sequences it was realized that precipitation could be avoided at low concentrations. Therefore, returning to the above sequences but setting up trays with lower DNA concentrations (and relatively high metalloinsertor concentrations, as described in section **4.3.1.4**) may produce single crystals. Indeed, these trays have already been set up with all eight metalloinsertor enantiomers and using all buffers in the Nucleic Acid Mini Screen. Additionally, crystal seeding experiments and streak seeding

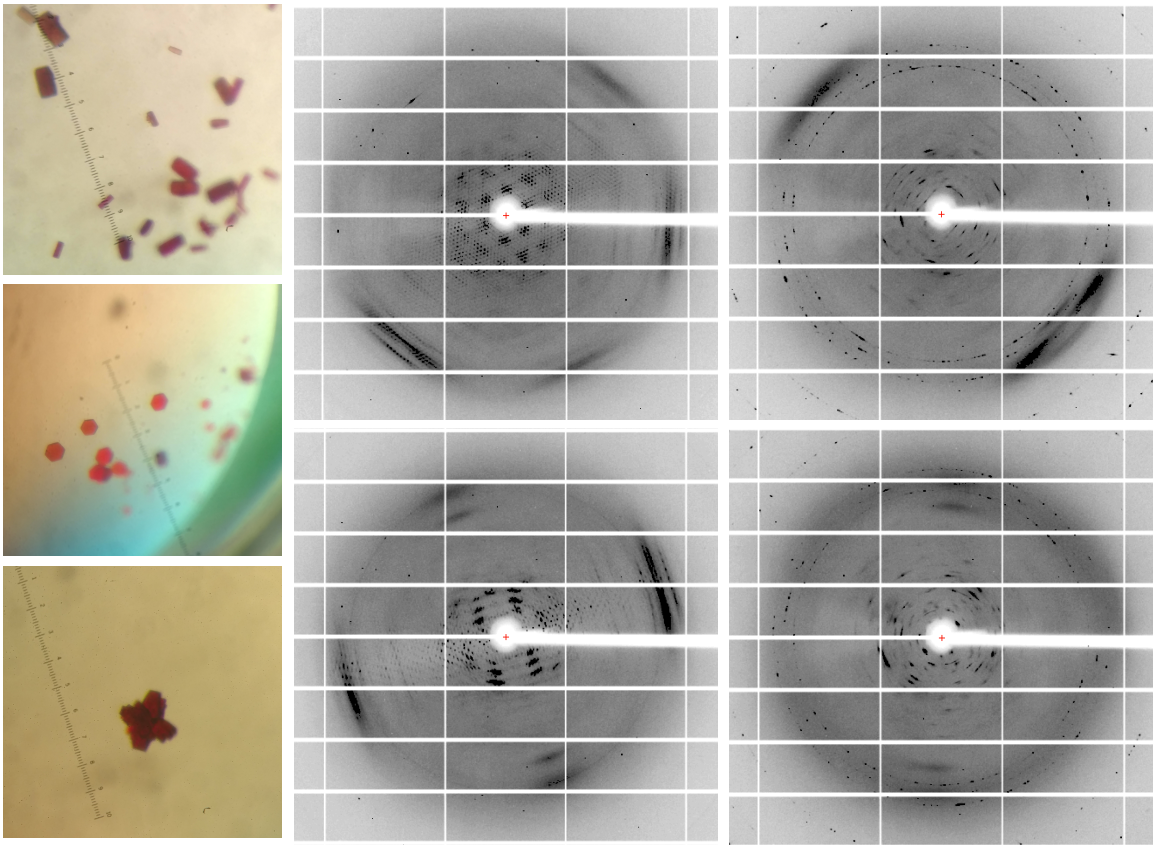

Figure 4.8 Example crystal morphologies and diffraction patterns from a rhodium enrichment experiment. (Left) Orange hexagonal crystals and rod-shaped crystals. (Middle) An example of a diffraction pattern from a hexagonal crystal at 0° and 90° rotations. (Right) Another example of a diffraction pattern from a rod-shaped crystal at 0° and 90° rotations.

experiments are currently underway.

Another potential approach could be to attempt crystallography with a racemic mixture of a metalloinsertor diastereomer. While this approach is not common in the literature, there is a recent example of a octahedral ruthenium complex being crystallized with DNA from a racemic mixture.[16] If the enantiomers bind DNA differently from each other, having two different enantiomers bound to the DNA sequence (which contains two mismatches that are relative close together) may be more complementary and stable than having two of the same enantiomer bound to the DNA sequence, especially if one of the enantiomers significantly distorts the DNA.

A third approach would be to explore additional structural methods. One option would be to instead determine the structure of the metalloinsertor in solution, as the Barton group has done previously with the metalloinsertor $[Rh(bpy)_2(chrysi)]^{3+}$.[17] This approach may be challenging, however, due to the tendency of Rh-O metalloinsertors to precipitate with DNA at high concentrations. Alternatively, a different structural method could be employed. Microcrystal electron diffraction (MicroED) is an emerging technique that could allow for the structural determination of a metalloinsertor bound to mismatched DNA. MicroED was developed by the Gonen lab at UCLA and has been used to determine high-resolution protein structures with only a small number of nano- or micro-crystals (i.e. nm to μm sized crystals).[18] Recently, the group used MicroED to solve the structure of α-synuclein, a Parkinson's disease related protein, at a staggering 1.4Å resolution using crystals that were a mere 200 nm thick.[19] Exploring these types of structural techniques may prove fruitful if traditional x-ray crystallography techniques do no begin to produce the desired results.

4.3.2 Crystal Structure of a DNA Mismatch Stabilized by Ba^{2+}

A crystal structure of the palindromic sequence 5'-CGG**T**AATT**C**CCG-3' was solved during the course of these experiments (**Figure 4.9** and **Table 4.6**). The diffracted crystal was a well-formed hexagon that was light orange in color, likely due to inclusion of red metalloinsertor molecules in solvent channels of the crystal. The crystal has been preliminarily solved to 1.6 Å and, to our knowledge, is the first crystal structure of a free DNA-duplex containing a TC mismatch. Overall, the structure of the DNA is minimally perturbed by the inclusion of these mismatches, as can be seen by comparisons to similar DNA sequences that contain well-matched AT and GC base pairs at the corresponding sites of the helix (**Figure 4.10**).[20,21] Overlaying the three DNA structures reveals good alignment on one end of the DNA duplex but deviations on the opposing end of the helix. At the base-pair level, there is a noticeable distortion of the DNA backbone at the TC mismatched site, wherein the backbones are pulled in towards the center of the helix to facilitate the TC base pairing interaction. This is primarily the result of a significant negative DNA stretch, determined using 3DNA software (**Figure 4.10**).[22] Of note is that the mismatch is further mediated by a barium cation, which forms stabilizing bonds with the electronegative carbonyl groups of both the cytosine and thymine bases (**Figure 4.9**). A similar stabilizing interaction was observed in 2.0 Å crystal structure of a polymerase bound to a DNA sequence containing a terminal TC mismatch, in which the TC mismatch is stabilized by a water molecule.[23] The crystal structure described herein suggests that this stabilizing effect observed in the polymerase structure is likely also present in naked DNA, either through the mismatch binding to water or to a biologically

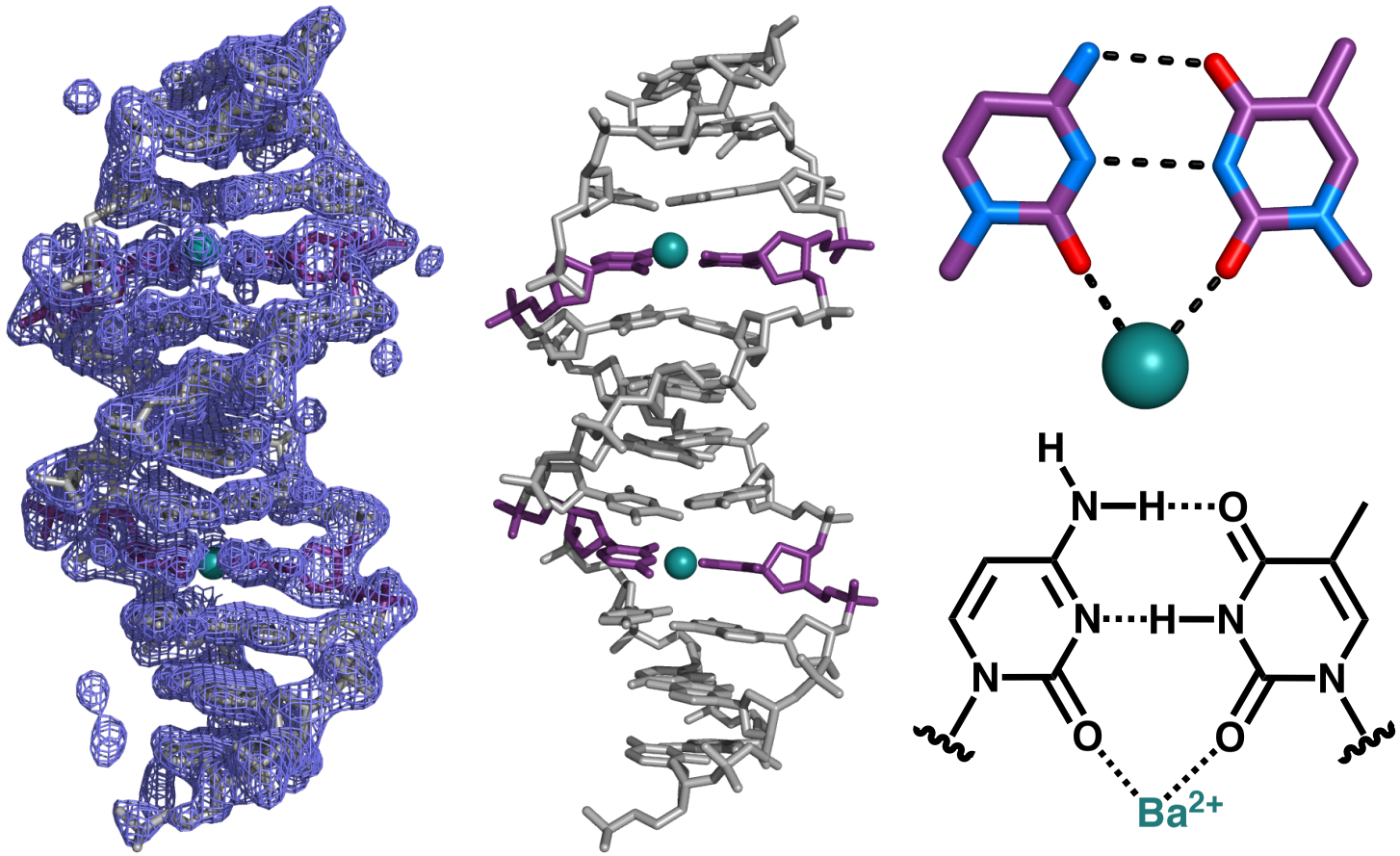

Figure 4.9 Crystal structure of DNA containing a barium-stabilized TC mismatched. (Left) The electron density map determine from the diffraction data with the DNA structure modeled in. (Middle) Structure of the sequence at 1.6 Å with mismatch highlighted in purple and barium highlighted in teal. (Right) the barium cation causes a stabilizing effect on the mismatched site by interacting with the electronegative carbonyl groups on the cytosine and thymine bases.

Table 4.6 Data collection and refinement statistics for TC mismatched DNA.

Structure 1	
Space group	$P3_121$
Cell dimensions	
a, b, c (Å)	66.5 66.5 38.2
α, β, γ (deg)	90 90 120
Resolution	33.27 - 1.61 (1.668 - 1.61)
$\mathbf{R_{merge}}$	0.06649 (1.219)
$\mathbf{R_{pim}}$	0.01598 (0.2869)
I/σI	19.62 (2.04)
Completeness (%)	89.51 (60.86)
Total reflections	240048 (24075)
Unique reflections	12862 (786)
Refinement	
Reflections used in refinement	11543 (779)
$\mathbf{R_{work}}$	0.2660 (0.3927)
$\mathbf{R_{free}}$	0.2909 (0.3492)
No. of DNA atoms	488
No. of Ba atoms	2
No. of water atoms	35
B-factor for DNA	43.26
B-factor for Ba	39.44
B-factor for water	44.49
Rmsd for bond lengths (Å)	0.013
Rmsd for bond angles (deg)	1.21

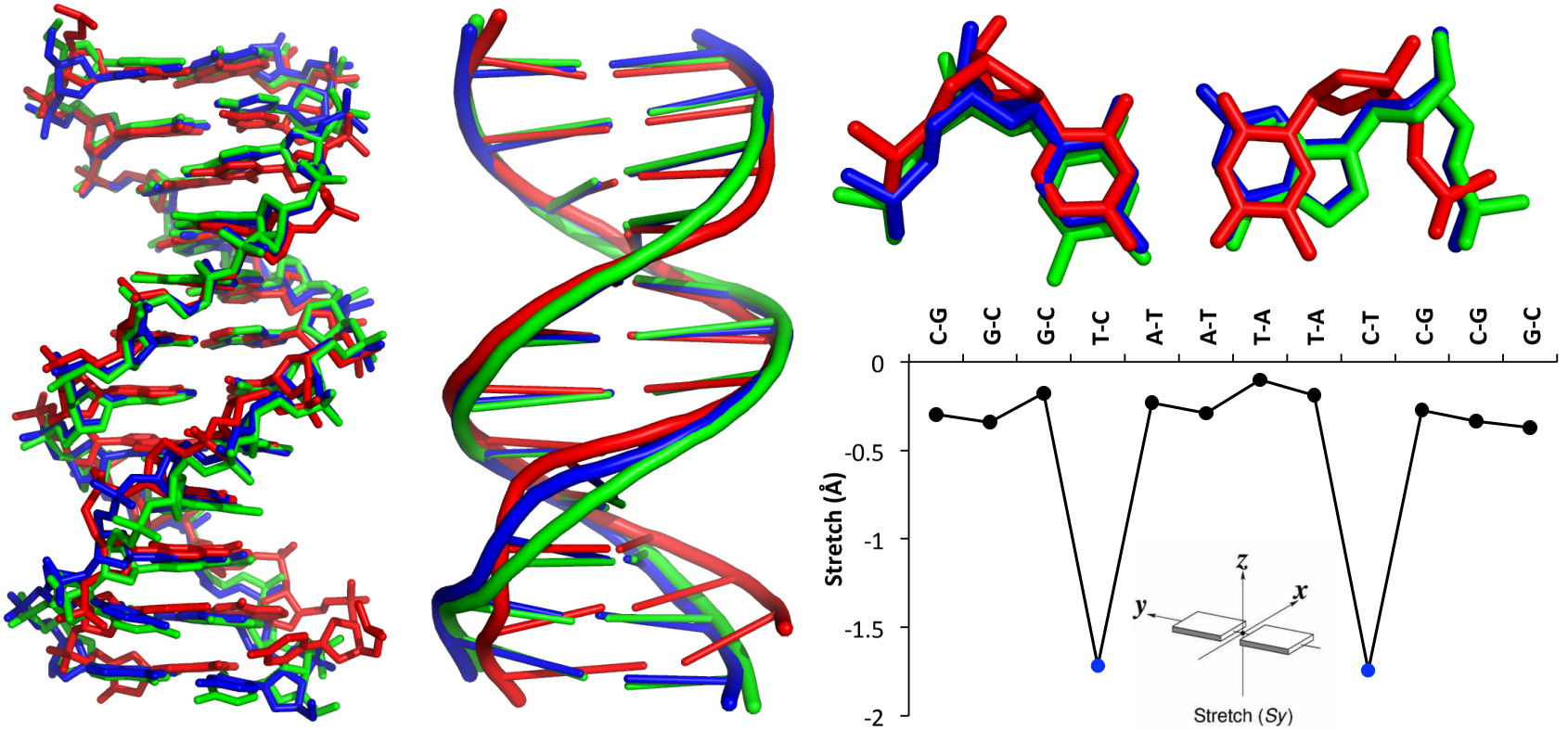

Figure 4.10 Comparison of TC mismatched DNA structure with well-matched sequences. (Left) Overlay of the mismatched duplex of 5'-CGGTAATTCCCG-3' (red,) with the well-matched duplexes 5'-CGCGAATTCGCG-3' (blue) and 5'-CGCAAATTTCGC-3' (green). (Middle) Cartoon representation of the overlay clarifying changes in overall structure, specifically at one end of the helix. (Right top) Overlay of the CT mismatch (red) over the well matched CG (blue) and AT (green) base pairs showing a significant distortion of the backbone. (Right bottom) The distortion is primarily due to a significant negative stretch as the two pyrimidine bases are pulled closer together to facilitate base pairing. Stretch schematic was taken from reference 22.

present cation. It is also of note that the C-dT mismatch is generated at one of the highest rates, alongside T-dG and G-dT mismatches.[24] Despite this, pyrimidine-pyrimidine mismatches are the most poorly identified and corrected by mismatches in bacterial systems.[25,26] If the same is true for eukaryotic systems, the stabilization of these mismatches by cellular cations or water molecules could contribute to this poor recognition or correction.

4.5 Conclusions

Over the course of this research, great strides have been made toward obtaining a single crystal of an Rh-O metalloinsertor with mismatched DNA. Originally, only poorly crystalline materials were observed due to high amounts of precipitation. Reducing concentration of these samples has allowed us to produce a variety of crystals with poor resolution. Altering the sequence of the crystallized DNA and increasing the ratio of metalloinsertor to mismatches in DNA have allowed us to move closer and closer to a crystal diffracting to high resolution. While there is still much to be done, it seems that a crystal structure of these new metalloinsertors with DNA is within reach! Such a crystal structure would undoubtedly aid our current understanding of the increased potency of these new Rh-O metalloinsertors and would allow us to rationally design new, better metalloinsertor complexes.

4.5 References

(1) Boer, D. R.; Canals, A.; Coll, M. *Dalt. Trans.* **2009**, 399–414.

(2) Hurley, L. H. *Nat. Rev. Cancer* **2002**, *2*, 188–200.

(3) Zeglis, B. M.; Pierre, V. C.; Barton, J. K. *Chem Commun* **2007**, *44*, 4565–4579.

(4) Harris, A. L.; Yang, X.; Hegmans, A.; Povirk, L.; Ryan, J. J.; Kelland, L.; Farrell, N. P. *Inorg. Chem.* **2005**, *44*, 9598–9600.

(5) Komeda, S.; Moulaei, T.; Woods, K. K.; Chikuma, M.; Farrell, N. P.; Williams, L. D. *J. Am. Chem. Soc.* **2006**, *128*, 16092–16103.

(6) Jackson, B. A.; Alekseyev, V. Y.; Barton, J. K. *Biochemistry* **1999**, *38*, 4655–4662.

(7) Jackson, B. A.; Barton, J. K. *J. Am. Chem. Soc.* **1997**, *119*, 12986–12987.

(8) Pierre, V. C.; Kaiser, J. T.; Barton, J. K. *Proc. Natl. Acad. Sci.* **2007**, *104*, 429–434.

(9) Lerman, L. S. *J. Mol. Biol.* **1961**, *3*, 18--IN14.

(10) Ernst, R. J.; Song, H.; Barton, J. K. *J. Am. Chem. Soc.* **2009**, *131*, 2359–2366.

(11) Komor, A. C.; Barton, J. K. *J. Am. Chem. Soc.* **2014**, *136*, 14160–14172.

(12) Boyle, K. M.; Barton, J. K. *J. Am. Chem. Soc.* **2018**, *140*, 5612–5624.

(13) Komor, A. C.; Schneider, C. J.; Weidmann, A. G.; Barton, J. K. *J. Am. Chem. Soc.* **2012**, *134*, 19223–19233.

(14) Zeglis, B. M.; Pierre, V. C.; Kaiser, J. T.; Barton, J. K. *Biochemistry* **2009**, *48*, 4247–4253.

(15) Song, H.; Kaiser, J. T.; Barton, J. K. *Nat. Chem.* **2012**, *4*, 615–620.

(16) Niyazi, H.; Hall, J. P.; O'Sullivan, K.; Winter, G.; Sorensen, T.; Kelly, J. M.; Cardin, C. J. *Nat. Chem.* **2012**, *4*, 621–628.

(17) Cordier, C.; Pierre, V. C.; Barton, J. K. *J. Am. Chem. Soc.* **2007**, *129*, 12287–12295.

(18) Shi, D.; Nannenga, B. L.; De La Cruz, M. J.; Liu, J.; Sawtelle, S.; Calero, G.; Reyes, F. E.; Hattne, J.; Gonen, T. *Nat. Protoc.* **2016**, *11*, 895–904.

(19) Rodriguez, J. A.; Ivanova, M. I.; Sawaya, M. R.; Cascio, D.; Reyes, F. E.; Shi, D.; Sangwan, S.; Guenther, E. L.; Johnson, L. M.; Zhang, M.; Jiang, L.; Arbing, M. A.; Nannenga, B. L.; Hattne, J.; Whitelegge, J.; Brewster, A. S.; Messerschmidt, M.; Boutet, S.; Sauter, N. K.; Gonen, T.; Eisenberg, D. S. *Nature* **2015**, *525*, 486–490.

(20) Fratini, A. V.; Kopka, M. L.; Drew, H. R.; Dickerson, R. E. *J. Biol. Chem.* **1982**, *257*, 14686–14707.

(21) Edwards, K. J.; Brown, D. G.; Spink, N.; Skelly, J. V.; Neidle, S. *J. Mol. Biol.* **1992**, *226*, 1161–1173.

(22) Lu, X. J.; Olson, W. K. *Nat. Protoc.* **2008**, *3*, 1213–1227.

(23) Johnson, S. J.; Beese, L. S. *Cell Press* **2004**, *116*, 803–816.

(24) Kunkel, T. A.; Erie, D. A. *Annu. Rev. Genet.* **2015**, *49*, 291–313.

(25) Modrich, P. *Annu. Rev. Biochem.* **1987**, *56*, 435–466.

(26) Marinus, M. G. *EcoSal Plus* **2012**, *5*, 1–41.

Chapter 5

CONCLUSIONS AND FUTURE OUTLOOKS

Mismatch repair is an essential DNA-processing pathway in healthy cells and tissues. Deficiencies in MMR proteins can lead to an abundance of DNA base pair mismatches and indels, which, if left uncorrected, will propagate into potentially disease-causing mutations upon cellular proliferation. These MMR-deficiencies can be seen with many types of cancer, including colorectal cancer and other solid tumors. Unfortunately, these MMR-deficient tumors have been historically challenging to treat, as they are often resistant to traditional chemotherapeutic agents. Clearly, the development of new therapeutic strategies that can effectively target MMR-deficient cancers is needed; therefore our group has spent the last 20 years developing a family of MMR-selected chemotherapeutic agents called rhodium metalloinsertors.

Rhodium metalloinsertors can selectively bind to DNA base pair mismatches *in vitro* and selectively kill MMR-deficient cancer cells over their MMR-proficient counterparts. Recently, our group discovered that the inclusion of an oxygen-containing ligand that forms an Rh-O bond leads to a significant increase in potency and MMR-selectivity of these "Rh-O" metalloinsertors. The work presented in this thesis has focused on further exploring the versatility of the Rh-O metalloinsertor framework, investigating the basis for increased potency and MMR-selectivity observed with these metalloinsertors, and assessing the biological activity of these complexes in diverse systems.

A family of Rh-O metalloinsertors differing in ligand bulk and lipophilicity was synthesized, characterized, and examined in human cancer cells. Nearly every Rh-O metalloinsertor proved to have robust potency and MMR-selectivity, regardless of its steric bulk or lipophilicity. We determined that MMR-selective behavior was retained in these complexes (and not in previous generations) due to low off-target accumulation in the mitochondria, which allows the mismatch-selective, on-target activity of these complexes to dominate the biological response. The answer to why these complexes are so potent remains unclear, though the results from studies on Rh-O metalloinsertors suggest a difference in DNA-binding could be the source. Crystallographic experiments have been employed and are still underway, and these studies will certainly give invaluable insight into the potency of these new complexes.

Our most promising Rh-O metalloinsertor was further studied in a diverse panel of 27 colorectal cancer cell lines to determine its general ability to kill cancer cells and target MMR-deficiencies. Overall, the metalloinsertor was significantly more potent that the FDA-approved chemotherapeutic agent cisplatin across this panel of cell lines. Additionally, correlation was observed between the potency of the metalloinsertor and the number of genomic DNA lesions that can be targeted by metalloinsertors, a result which helps to confirm that DNA mismatches are the cellular target of the rhodium metalloinsertor.

The lessons learned from the experiments described in this thesis will hopefully pave the way for the future development of rhodium metalloinsertors. The Rh-O metalloinsertor framework has proven to be an extremely tunable scaffold for the development of metalloinsertors that retain both potency and selectivity in the face of

great structural variation. This versatility opens many doors for the development of MMR-based therapeutics and diagnostics, and already our group has used this knowledge to develop potent and selective metalloinsertor conjugates, something that was not possible with previous generations of metalloinsertors. Understanding the effect of biological variation on metalloinsertor activity allows us to anticipate potential challenges and successes of our metalloinsertor as we move it towards pre-clinical and clinical. Indeed, our group has recently begun moving metalloinsertors into *in vivo* models, and we eagerly await the undoubtedly exciting results that are to come.